STRUCTURE ANALYSIS OF TITANATE NANOTUBE/ORGANIC MOLECULE HYBRID AND SELF-HEALING POLYMER

YUANYUAN JIA

A dissertation submitted to the faculty of the University of North Carolina at Chapel Hill in partial fulfillment of the requirements for the degree of Doctor of Philosophy in Department of the Department of Physics and Astronomy.

Chapel Hill
2007

Approved by

Advisor: Professor Yue Wu

Reader: Professor Alfred Kleinhammes

Reader: Professor Laurie E. McNeil

Reader: Professor Jianping Lu

Reader: Professor Yee Jack Ng

ABSTRACT

YUANYUAN JIA: Structure Analysis of Titanate Nanotube/Organic Molecule Hybrid and Self-Healing Polymer

(Under the direction of Professor Yue Wu)

In this dissertation I report the structure and property characterization of two kinds of materials on the micro- and nano-scale level, the self-healing polymer Surlyn® and a titanate nanotube/organic molecule hybrid. Multiple techniques have been utilized to study the structural, dynamic, thermal, and optical properties of the materials.

In the first study, the thermal, structural, and dynamic properties of the self-healing polymer Surlyn® (poly(ethylene-*co*-methacrylic acid) polymer neutralized with Na^+) were investigated. By introducing a suitable cation, Na^+ e.g., Surlyn® possesses unique properties, such as the intriguing property of self-healing. Understanding the role of the cations in the material, the chemical structure and the physical properties of the polymer is crucial for potential applications. The thermal property of Surlyn is characterized by differential scanning calorimetry (DSC) and microscopic structures are studied by NMR. It is found that although thermal properties change significantly, the structure and dynamics of ionic aggregates (consisting of Na^+-O^- pairs) remain unchanged under aging and mechanical deformation. The distance between Na^+ ions was also estimated.

In the second study titanate nanotubes were successfully synthesized. Titanate nanotubes have great potential for applications in photocatalysis due to their unique structural and photocatalytic properties. However, their wide band gap, 3.7 eV, and the Ti defect sites present problems for the photovoltaic applications Surface modification, e.g. attachment of charge-transfer ligands, is one of the most effective approaches to modify the optical absorption spectrum and restore the sixfold coordination of Ti sites. In order to study the mechanisms of bonding between titanate nanotubes and the charge transfer ligands, I chose three different molecules, hydroquinone, 4-methoxypenol(MEHQ) and catechol. Each of these three molecules is expected to form different bonding configuration. The optical and structural properties of titanate nanotubes and the three hybrid structures (titanate nanotube/hydroquinone, titanate nanotube/MEHQ and titanate nanotube/catechol) are characterized by multiple techniques, such as UV-vis, Raman spectroscopy, X-ray diffraction and NMR spectroscopy, etc. It is found that by forming a bidentate structure, organic molecules (hydroquinone and catechol) and titanate nanotubes can form hybrid structures which are relatively stable in the aqueous environment. Also, it was demonstrated that there are significant differences in local structures between water-washed and acid-washed titanate nanotubes. For acid-washed nanotube, the local structure can be changed reversibly into an anatase-like structure by the incorporation of HQ, MEHQ, or CAT. This provides important clues for understanding the structure of titanate nanotubes and the interaction between ligands and nanotube surfaces. The hybrid system of titanate nanotubes/organic molecules has optical absorption significantly beyond 700 nm. This system could have very important applications in photocatalysis and photovoltaic devices.

ACKNOWLEDEMENTS

I would like to express my sincere gratitude to my advisor, Prof. Yue Wu. It was his guidance, encouragement and support that led me through the most demanding and rewarding years of my life. His enthusiasm for and insight into science have greatly stimulated me. It has always been a refreshing experience discussing with him. I also want to extend my special gratitude to Dr. Alfred Kelinhammes. I am thankful for his kindness and patience. It would be much harder for me without his discussion and encouragement.

I am also deeply grateful for all the generous help and supports from other group members, past and present: Professor Horst Kessemmier, Dr. Qiang Chen, Harsha Kulkani, Dr. Lilong Li, Shenghua Mao, Dr. XueKui Xi, Gregory Mogilevsky, and particularly Professor Alfred Kleinhammes.

I would also like to thank all my former and current committee members, Yue Wu, Alfred Kleinhammes, Laurie E. McNeil, Jianping Lu, Yee Jack Ng, for their enlightening advice and warm-hearted help. Edward Samulski gave valuable advice and critique till the final oral defense, which he is unable to attend due to schedule conflicts.

Finally, I am so grateful to my parents. They are the forever support of my life for whichever path I choose. It would have been so much harder without them.

CONTENTS

6 HYBRID STRUCTURE OF TITANATE NANOTUBE AND ORGANIC MOLECULES……………………………….………………………......……85

LIST OF FIGURES

LIST OF TABLES

CHAPTER 1

INTRODUCTION

In the field of materials sciences, there is growing interest in controlled designs of materials whose functionalities arise from, or are supported by, their microscopic structures, usually on the nanometer scale. Being able to understand the microstructure of the materials and characterize their properties is crucial in order to control and direct the synthesis process, to produce materials with predictable structure and properties and, finally, to improve known materials and design new one.

In this dissertation I report the structure and property characterization of two kinds of materials on the micro- and nano-scale level, self-healing polymer Surlyn® and titanate nanotube/organic molecule hybrid. Multiple techniques have been utilized to study the structural, dynamic, thermal, and optical properties of the materials. NMR is one of the major characterization tools employed in our study. Before I start the discussion on the structure and property characterization of the materials, the background of NMR spectroscopy in **Chapter 2** to give the reader some familiarity and pave the way for later discussions.

In the first study, the thermal, structural, and dynamic properties of self-healing polymer Surlyn® (poly(ethylene-*co*-methacrylic acid) polymer neutralized with Na^+) were investigated. By introducing a suitable cation, Na^+ e.g., Surlyn® processes unique mechanical, rheological and thermal properties, as well as the intriguing property of self-healing following high-speed impact – after penetration of a bullet, the material can patch the hole and heal itself. It is hoped that these materials might have applications for protecting the space station or space vehicles from destructive micrometeorite impacts. However, currently, Surlyn® is not resistant to UV. Understanding the role of the cations in the material, the chemical structure and the physical properties of the polymer is crucial for potential applications. A modest fundamental understanding of the Surlyn® polymer has been established in the last few decades. An introduction about the previous studies on the chemical structure and physical properties of Surlyn® is presented in **Chapter 3**, including the microstructure models proposed mainly based on small angle X-ray scattering (SAXS) data. Yet much still remain to be learned about the properties of the polymer. In **Chapter 4**, I will discuss the experimental results of thermal properties obtained by differential scanning calorimetry (DSC) and microscopic structures obtained by nuclear magnetic resonance (NMR). It is found that although thermal properties change significantly, the structure and dynamics of ionic aggregates (consists of Na^+-O^- pairs) remain unchanged under aging and mechanical deformation. The distance between Na^+ ions was also estimated.

In the second study titanate nanotubes were successfully synthesized. Titanate nanotubes combine the properties and applications of conventional TiO_2 nanoparticles (e.g. photocatalysis, wide band gap) with the properties of layered titanates (e.g. ion exchange). Owing to the larger surface area of 293 m^2/g (5-10 times larger than TiO_2 nanoparticles) and higher photoactivity[1], titanate nanotubes have great potential for applications of photocatalysis. However, their wide band gap, 3.7 eV, limits the solar conversion efficiency in photovoltaic applications. It was reported [2] that 40 % of Ti atoms in such nanotubes are undercoordinated, which could present problems for electron transport. Surface modification, e.g. attachment of charge-transfer ligands, is one of the most effective approaches to modify the optical absorption spectrum and restore the sixfold coordination of Ti sites. Understanding the microstructure of titanate nanotubes and their properties is of great importance in order to predict, control and direct the surface modification process. However, up to now, the structure and the formation mechanism of titanate nanotubes have not been clarified. It was reported [2] that the coordination geometry of Ti atoms in titanate nanotubes differs from that in bulk TiO_2, and is surprisingly similar to that of 2 nm diameter nanoparticles. As a result, we studied the surface chemistry and structural properties of titanate nanotubes based on those of TiO_2 nanoparticles. The undercoordinated Ti sites presented on the surface of small TiO_2 nanoparticle are very reactive for certain molecules such as catechol. It was observed that there was a large optical red shift of about 1.6 eV when catechol molecules are adsorbed on TiO_2 nanoparticles. Based on a theoretical calculation [3], it was found that the different binding configurations of catechol on nanoparticle surfaces (e.g. monodentate and bidentate structures) lead to the different absorption energies, and may induce different structural changes of TiO_2 nanoparticles [4]. Similar to TiO_2 nanoparticles, our result shows that when titanate nanotubes were exposed to organic molecules, e.g. catechol, their color changes along with changes of local structures. In order to study the mechanisms of different binding configurations and the induced structure changes experimentally, we chose three different molecules, hydroquinone, 4-Methoxypenol(MEHQ) and catechol. Each of these three molecules is expected to form different binding configuration. For example, MEHQ can only form the monodentate structure. The optical and structure properties of titanate nanotubes and the three hybrid structures (titanate nanotube/hydroquinone, titanate nanotube/MEHQ and titanate nanotube/catechol) were characterized by multiple techniques, such as UV-Vis, Raman spectroscopy, X-ray diffraction and NMR spectroscopy, etc.

In **Chapter 5**, a review of previous studies about titanate nanotubes is presented, including the synthesis, proposed structures, formation mechanism and properties, especially surface properties. The properties of titanate nanotubes, especially surface chemistry, are discussed based on those of TiO_2 nanoparticles. Some important applications are briefly mentioned at the end of **Chapter 5**. In **Chapter 6** the experimental results are discussed in detail, starting with the synthesis processes of the titanate nanotubes and titanate nanotube/organic molecule hybrid, followed by the properties characterization of the hybrid structures using UV-Vis, Raman spectroscopy, X-ray diffraction and NMR spectroscopy, etc. Through comparing the results of the three hybrid structures, it is found that by forming bidentate structure, organic molecules (hydroquinone and catechol) and titanate nanotubes can form hybrid structures which are relatively stable in the aqueous environment. Also, it was demonstrated that the local structure of titanate nanotubes can be changed reversibly into anatase-like structure by the incorporation of organic molecules. This provides important clues for understanding the structure of titanate nanotubes and the interaction between ligands and nanotube surfaces. The hybrid system of titanate nanotubes/organic molecules has optical absorption significantly beyond 700 nm. This system could have very important applications in photocatalysis and photovoltaic devices.

Both studies have led to publications which are summarized in **Chapters 3** and **4** (self healing) and **5** and **6** (titanate nanotube/organic molecule hybrid structure).

A brief summary is presented in **Chapter 7**.

1.1 References.

1. M. Adachi, Y. Murata, and M. Harada, *Chem. Lett*, **8,** 942 (2000).

2. Z. V. Saponjic, N. M. Dimitrijevic, D. M. Tiede, A. J. Goshe, X. Zuo, L. X. Chen, A. S. Barnard, P. Zapol, L. Curtiss, and T. Rajh, *Adv. Mater.*, **17**, 965 (2005).

3. P. C. Redfern, P.Zapol, L. A. Curtiss, T. Rajh, and M. C. Thurnauer, *J. Phys. Chem. B*, **107,** 11419 (2003).

4. T. Rajh, J. M. Nedeljkovic, L. X. Chen, O. Poluektov, and M. C. Thurnauer, J. Phys. Chem. B, **103,** 3515 (1999).

CHAPTER 2

NMR AS A PROBE OF MOLECULAR STRUCTURE AND DYNAMICS

Nuclear magnetic resonance (NMR) is a phenomenon that occurs when the nuclei of certain atoms are immersed in a static magnetic field and exposed to a second oscillating magnetic field. It is a sensitive tool of local structures and dynamics. Here, I'll discuss briefly some basic aspects of NMR. Unless explicitly mentioned, the content discussed in this chapter is derived from three books authored by Abragam,[1] Slichter[2] and Fukushima and Roeder[3].

2.1 Basics of NMR Spectroscopy

Most nuclei have a non-zero spin angular momentum $\hbar\vec{I}$ with corresponding magnetic moment $\vec{\mu}$ given by

$$\vec{\mu} = \gamma \cdot \hbar \cdot \vec{I} \tag{2.1}$$

$\vec{I}$ is the spin angular momentum, the proportionality constant γ is called the gyromagnetic ratio and $h = 2\pi\hbar$ is the Planck constant.

Assume that we have a static magnetic field $\vec{B}_0$. The Zeeman interaction between the magnetic moment $\vec{\mu}$ and the external magnetic field $\vec{B}_0$ is given by

$$\mathcal{H} = -\vec{\mu} \cdot \vec{B}_0 = -\gamma\hbar\vec{I} \cdot \vec{B}_0 \tag{2.2}$$

For simplicity, consider spins that have two eigenstates (spin ½), spin-up and spin-down. According to Eq. (1.2), the energy difference between the two spin states can be represented by

$$E = \hbar\omega_0 = E_{-1/2} - E_{1/2} = \gamma\hbar B_0 \tag{2.3}$$

When the energy of an incident photon matches the energy difference between the two spin states, absorption of energy occurs. In other words, if an electromagnetic excitation with a frequency $\nu = \omega_0 / 2\pi$ is applied, a resonance occurs, and it is called nuclear magnetic resonance. ν is called the Larmor frequency and it is usually in the radio frequency range for typical external magnetic field.

According to Boltzmann statistics, in a bulk sample containing *N* spins, at temperature *T*, the spin population difference between these states provides a macroscopic magnetization of the spin system given by:

$$M = N\gamma\hbar \frac{\sum_{m=-I}^{I} m \exp(\gamma\hbar m B_0 / kT)}{\sum_{m=-I}^{I} \exp(\gamma\hbar m B_0 / kT)} \tag{2.4}$$

In nuclear magnetism, where the ratio $\gamma\hbar B_0 / kT$ is almost always a very small number, Eq. (2.4) now simplifies to

$$M = \frac{N\gamma^2\hbar^2 I(I+1)}{3kT} B_0 = \chi_0 B_0 \tag{2.5}$$

χ_0 is called the static nuclear susceptibility. At room temperature, $\chi_0 \sim 10^{-10}$ due to the very small eigenstate population difference, which in turn is due to the small energy difference between the two states compared with *kT*.

So if we insert a sample into a magnetic field, a macroscopic magnetization will be induced. The process of growth towards the equilibrium magnetization described in Eq (2.5) is defined as spin-lattice relaxation. The symbol T_1 is used as the spin-lattice relaxation time. After the external field is turned on, in order for a spin with its moment $\bar{\mu}$ antiparallel to the field (with a potential energy $+\mu B_0$) to turn parallel to the field (in which case its potential energy will be $-\mu B_0$), it has to give up $2\mu B_0$ of energy. The spin can only make the jump to the lower energy when there is an agent to accept this energy. Thus, the rate at which magnetization builds up in a static field depends on the mechanism available for the spins to transfer energy to something else – namely the other repositories for thermal energy such as the translations, rotations, and vibrations, collectively called the lattice. The buildup curve for the net magnetization is usually approximately exponential given by

$$M_z = M_0(1 - \exp(-t/T_1)) \tag{2.6}$$

In a magnetic resonance experiment, we place a sample and a coil in the field of a laboratory magnet in such a way that the rf magnetic field generated in the coil is perpendicular to the static field, shown in Fig. 2.1. In Fig. 2.1 (a), when the transmitter is turned on, the sinusoidal rf current in the transmitter coil generates a linearly polarized magnetic field $2B_1\cos(\omega_0 t)$ .This linear polarization can be decomposed into two counter-rotating vectors of magnitude B_1 as shown in Fig. 2.1 (b). In a frame rotating at ω_0(Fig. 2.1 (c)), one of the rotating fields will have the right frequency and appears to be stationary. The other one will be neglected because it is $2\omega_0$ away from the right frequency and has little interaction with the spin system. The magnetization $\vec{M}$ will rotate in the rotating frame about this $\vec{B}_1$ field at angular speed $\vec{\omega}_1 = \gamma\vec{B}_1$ and since $\vec{B}_1$ is perpendicular to the laboratory field $\vec{B}_0$, $\vec{M}$ will change its orientation with respect to the static field, therefore, an appropriate combination of the intensity and the duration of the rotating field can rotate the magnetization $\vec{M}$ by any desired amount (Fig. 2.1 (d)). Such a magnetization turned 90° (Fig. 2.1 (e)) from $\vec{B}_0$ is stationary in the rotating frame after $\vec{B}_1$ has been turned off but is precessing at the Larmor frequency in a plane perpendicular to the static magnetic field in the laboratory frame. This precession generates NMR signal picked up by the rf coil. In an actual experiment, owing to various mechanisms which usually are interesting in NMR studies, the precessing magnetization decays. The decay will induce a decrease of the rf signal. The signal induced in the coil is a free precession signal and owing to its decay, is called the free induction decay (FID). The signals contain enough information to determine both the magnitude of the Larmor frequency ω_0 and the decay time constant T_2. After a Fourier transform, a NMR peak with a width of $1/(\pi T_2)$ (in units of Hz) will be obtained. Later in this dissertation it will become clear that in a real system, due to internal interactions the resonance frequencies will have a distribution, from which the local environment of the nucleus is determined.

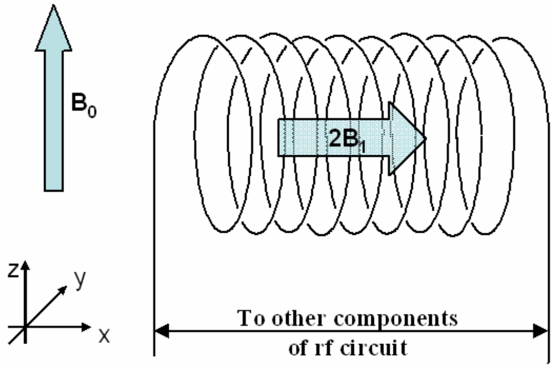

(a) Osillating B_1 field generated by coil rf current. B_1 is perpendicular to the external magnetic field B_0.

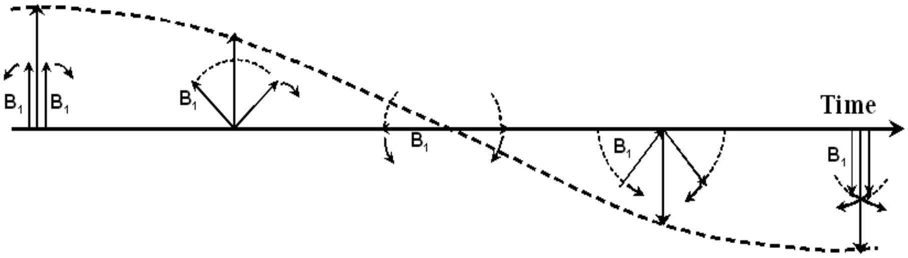

(b) Decomposition of B_1 into two fields rotating in opposite directions.

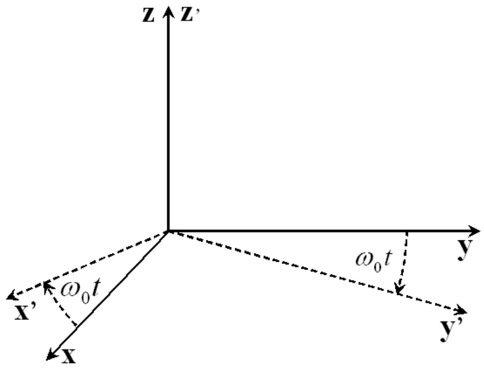

(c) Rotating frame.

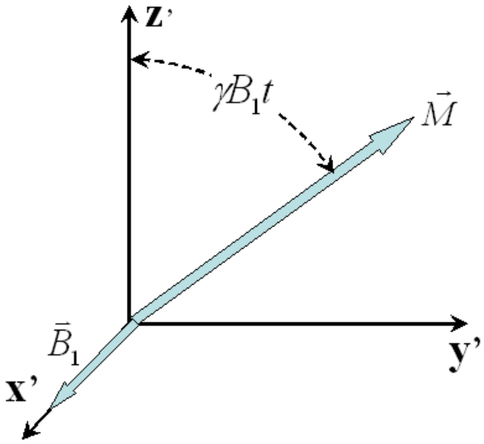

(d) Magnetization in rotating frame.

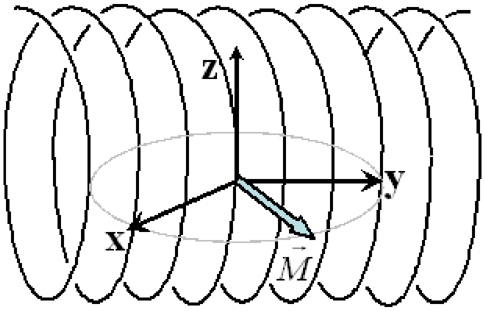

(e) Pulse off; precessing magnetization in the laboratory frame, which induces a signal detectable by coil.

Fig. 2.1 Illustration of the effect of a radio frequency pulse.[3]

The discussion above didn't include the internal interactions between the nuclear spins and the environment such as other nuclear spins, electron spins, and the electric field gradient (EFG) produced by electrons. Normally such internal interactions are sufficiently small compared to the main Zeeman interaction, so in quantum mechanics, we can treat them as a perturbation to the main Zeeman interaction, and the net effect is that the nucleus of interest would experience a small additional magnetic field due to interactions with the environment.

2.2 Internal Interactions

In the above discussion we neglected the internal interactions. We will discuss three such internal interactions which are directly relevant to our study: chemical shift, dipolar interaction, and quadruple interaction.

2.2.1 Chemical Shift -- Magnetic Interaction of Nuclei with Electrons

When an atom is placed in a magnetic field, its electrons circulate about the direction of the applied magnetic field. This circulation causes a small local magnetic field $\vec{B}_{induced}$ at the nucleus which opposes the externally applied field $\vec{B}_0$. The magnetic field at the nucleus (the effective field) $\vec{B}_{eff}$ is therefore generally less than the applied field by a fraction σ.

$$B_{eff} = B_0 - B_{induced} = B_0(1-\sigma) \tag{2.7}$$

σ is called the chemical shift. The electron density around each nucleus in a molecule varies according to the types of nuclei and bonds in the molecule. The opposing field and therefore the effective field at each nucleus will vary. Therefore, a magnetic resonance line of a spin system in an inhomogeneous magnetic field has a certain width owing to the spread of their Larmor frequencies, and the corresponding broadening of the line is called inhomogeneous broadening.

The chemical shift is the difference between the resonance frequencies of the nucleus and a reference,normalized by the reference frequency. This quantity is reported in ppm and is given the symbol delta, δ.

$$\delta = \frac{(\nu - \nu_{\mathrm{Re}\,f}) \times 10^6}{\nu_{\mathrm{Re}\,f}} \tag{2.8}$$

In NMR spectroscopy of ^{13}C and ^{1}H, this reference is often tetramethylsilane, $Si(CH_3)_4$, abbreviated TMS. The chemical shift is a very precise metric of the chemical environment around a nucleus.

2.2.2 Quadrupolar Interaction

Nuclei with spin quantum number $I \geq 1$ have an electric quadrupole moment Q that couples with the electric field gradient (EFG) existing in molecules and solids. The EFGs are exclusively generated by the electrons and nuclei of molecules and crystals, and the sum of these is a three-dimensional entity with the properties of a tensor. To describe it fully, we need to specify its size, shape, and orientation. The quantity eq is a parameter of the size. The shape is characterized by the asymmetry parameter η, which is a measure of the deviation of the EFG from axial symmetry. η can have any value between 0 and 1, with $\eta = 0$ corresponding to axial symmetry. The orientation of the EFG with respect to the molecular or crystalline structure is defined by Euler angles. The value of the size of the quadrupolar interaction, in frequency units, e^2qQ/h, is called the nuclear quadrupolar coupling constant (NQCC). In the literature, quadrupolar interactions are commonly reported by specification of their NQCC and η. The angular parameters are not usually provided unless orientation information is of special interest.

The quadrupolar interaction vanishes in three general cases.

1. No quadrupolar interaction is ever associated with an I = 1/2 nucleus, because Q vanishes for all subatomic particles with spin quantum number I = 0 or 1/2.
2. The NQCC is zero when a quadrupolar nucleus is positioned at a cubic (octahedral or tetrahedral) site, because then $eq = 0$ by symmetry.
3. The quadrupolar interaction of a nucleus belonging to a molecule in an isotropic liquid or a gas is averaged to zero by the rapid tumbling motion of the molecule.

The contribution of the quadrupolar interaction to the magnetic resonance line width of the central transition $\frac{1}{2}\leftrightarrow-\frac{1}{2}$ in Hz is given by[4]

$$\Delta\nu(\frac{1}{2}\leftrightarrow\frac{1}{2})\propto-\frac{3\chi^2}{2[2I(2I-1)]^2\nu_L} \tag{2.9}$$

Here, $\nu_L=\gamma_I B_0/2\pi$ is the Larmor frequency determined by the external magnetic field B_0 and the gyromagnetic ratio γ_I . $\chi=e^2qQ/h$ is the nuclear quadrupolar coupling constant.

The size of the quadrupolar interaction experienced by a particular nucleus is a constant that is characteristic of the molecular or crystalline environment, and quadrupolar nuclei are very sensitive to structure and symmetry. This provides the connections between quadrupolar nucleus NMR spectra and structure.

2.2.3 Dipolar Interaction – the Direct Magnetic Interactions of Nuclear Spins with Each Other

It has already been stated in previous sections that chemical shift and quadrupolar interaction cause a magnetic resonance line a certain width. In both case the line width is due to the differences among the resonance frequencies of the individual spins rather than to interactions among them. The situation is very different if the line width is due to the existence of couplings between neighboring spins.

2.2.3.1 General Theory of Dipolar Interaction

The interaction between two nuclear spins depends on the magnitude and orientation of their magnetic moments and also on the length and orientation of the vector describing their relative positions. The effects of this interaction depend strongly on whether this vector is fixed in space or changes rapidly because of relative motion of the nuclei. The latter case is true in liquid and gases, and we will just limit ourselves for the present to a rigid lattice where the nuclei can be considered fixed, a reasonable approximation in many solids at room temperature.

The dipolar interaction between two magnetic moments $\vec{\mu}_i = \gamma_i \hbar \vec{I}_i$ and $\vec{\mu}_j = \gamma_j \hbar \vec{I}_j$ can be written as follows:

$$\mathcal{H}_{ij} = \frac{\gamma_i \gamma_j \hbar^2}{r_{ij}^3} \{\vec{I}_i \vec{I}_j - 3\frac{(\vec{I}_i \cdot r_{ij})(\vec{I}_j \cdot r_{ij})}{r_{ij}^2}\} \tag{2.10}$$

In this dissertation, we only discuss the interaction in a system of identical interacting spins, thus, the Hamiltonian $\mathcal{H}$ can be written as:

$$\mathcal{H} = \sum_{i<j} \mathcal{H}_{ij} = \sum_{i<j} \frac{\gamma^2 \hbar^2}{r_{ij}^3} \{\vec{I}_i \vec{I}_j - 3\frac{(\vec{I}_i \cdot r_{ij})(\vec{I}_j \cdot r_{ij})}{r_{ij}^2}\} \tag{2.11}$$

The task of finding the eigenstates of $\mathcal{H}$ in Eq. (2.9) is a formidable one and no exact solution exists. In order to go beyond qualitative statements, the method of moment is introduced. If the spins in a system are subjected to the same central transition $(\frac{1}{2} \leftrightarrow -\frac{1}{2})$ frequencies, but different quadrupolar coupling (different magnitude and/or orientation of the electric field gradient), called semi-like spins, the second moment M_2 determined by dipole-dipole interactions can be given in a powder average by[1]

$$M_2 = \frac{9}{5} (\gamma_I^2 \hbar)^2 \frac{1}{N} F_{SL}(I) \sum_{i,k} \frac{1}{r_{ik}^6} \tag{2.12}$$

where $F_{SL} = \frac{4I(I+1)}{27} + \frac{(2I+1)}{18} + \frac{(2I+1)^3}{288}$ is a spin-dependent factor. For ^{23}Na nuclei I=3/2 and $F_{SL}(I)$=1, N is the number of interacting ^{23}Na nuclear spins, and the summation is over all pairs of ^{23}Na nuclei i and k with distance r_{ik}.

As mentioned above, the method of moment enables one to compute properties of the resonance line without solving explicitly for the eigenstates and eigenvalues of energy. Thus, it provides a way to make theoretical predictions using the experimental results. In the next section, we will discuss how to predict the structure of the solids through the comparison of the theoretical values of M_2 and the NMR signals obtained by using a widely-used NMR technique – spin echo decay, also called Hahn-echo decay.

2.2.3.2 Spin Echo Decay

In this section we will discuss what spin echoes are and what information they provide for the insight of the static and dynamic structure of solid.

Consider a group of spins initially in thermal equilibrium in a static magnetic field $\vec{B}_0$ in the z-direction. The thermal equilibrium magnetization M_0 then lies along $\vec{B}_0$ as shown in Fig. 2.2 (a). We assume there is a spread in magnetic field over the sample, and take the average value of field to be B_0. We apply rotating magnetic field B_1 at $t = 0$ with frequency ω to generate a $\pi/2$ pulse. Let the $\pi/2$ pulse rotate M_0 to lie along the negative y-axis (Fig. 2.2 (b)). The existence of inhomogeneity leads to a spread in precession rates and dephasing. Consider what happens during a time interval τ. In any small region of the sample, the magnetization $\delta\vec{M}$ will remain in the x-y plane since we are neglecting the precession along z-direction. But at the end of τ, the direction of $\delta\vec{M}$ within that plane will advance from the $-y$ –direction by some angle which we call θ, given by

$$\theta = \gamma \delta B \tau = \gamma (B - B_0)\tau \tag{2.13}$$

which represents the inhomogeneity in B (Fig. 2.2 (c)). Suppose now we apply a π pulse at $t = \tau$, the situation is shown in Fig. 2.2 (d). Noting the orientation of $\delta \vec{M}$, we immediately see that during a second time interval τ, $\delta \vec{M}$ will again advance through the same angle θ, which will bring it exactly along the positive y-axis at $t = 2\tau$ (Fig. 2.2 (e)). Though all the spins are in phase at $t = 2\tau$, they get out of phase again owing to the field inhomogeneity, so the free induction signal decays.

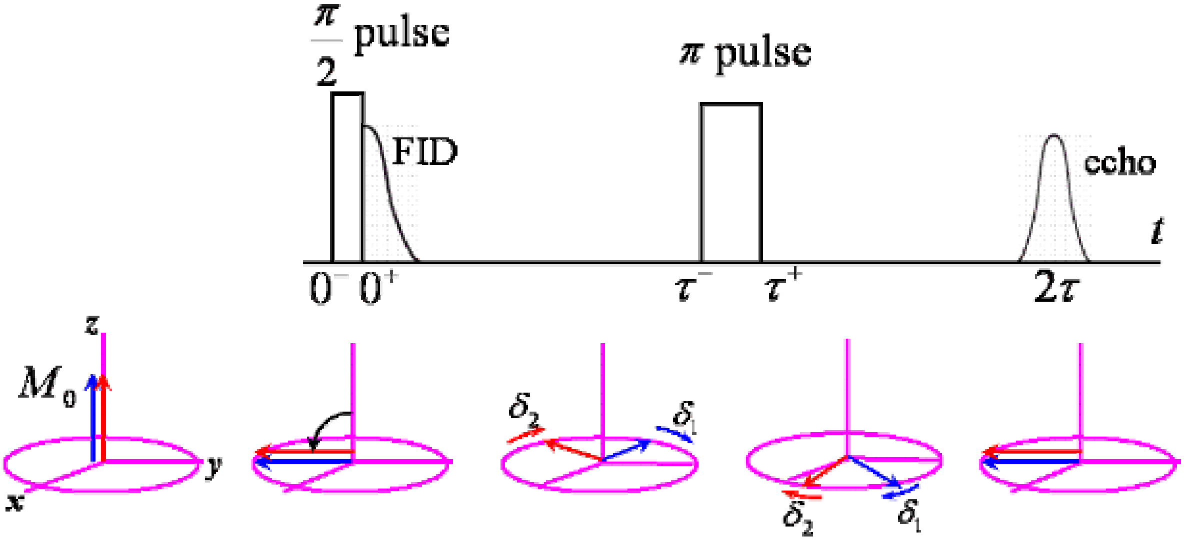

(a)$t = 0^-$ (b)$t = 0^+$ (c)$t = \tau^-$ (d)$t = \tau^+$ (e)$t = 2\tau$

Figure 2.2 Spin-echo pulse sequence and rotation of the magnetization.[3]

The spin echo will refocus any time-independent variations in the resonance frequency, including chemical shifts, susceptibility shifts, and heteronuclear spin couplings. However, the dephasing induced by homonuclear dipolar interaction can not be refocused by methods such as the spin echo. As one varied τ , the echo amplitude diminishes. If the decay is exponential, the decay time constant T_2 is called transverse relaxation time. Under the influence of homonuclear dephasing, as shown in reference [4], the spin echo intensity S versus τ is described by

$$S(2t) \propto \exp[-M_{2E}(2\tau)^2/2] \tag{2.14}$$

If effect of motion is negligible $M_{2\mathrm{E}}$ is determined solely by dipole-dipole interactions. For 'semi-like spins' and selective excitation of the central transition ($\frac{1}{2} \leftrightarrow -\frac{1}{2}$), $M_{2\mathrm{E}}$ is given by $M_{2\mathrm{E}} = 0.5M_2$. M_2 is the second moment determined by dipole-dipole interactions given by Eq. (2.10).

In powdered solids, the presence of anisotropic interactions leads to broad lines, as the different molecular orientations give rise to different resonance frequencies. If the anisotropy of the coupling exceeds the chemical shift the lines will overlap and the chemical shift resolution is lost. In addition to this, dipolar couplings between abundant nuclei (e.g. protons) broaden the lines dramatically and lead to spectra that basically consist of one large 'hump'. In liquids, the fast isotropic tumbling of the molecules averages the anisotropic interactions to zero and no such substantial line broadening is observed. Thus, it would be desirable to mimic this motion to get spectral resolution in solid samples.

One method for achieving high-resolution NMR is to artificially narrow NMR lines in solids, by physically spinning the sample in a specific way to eliminate the broadening. This is known as magic angle spinning (MAS). In the presence of abundant spins, it may be possible to obtain a high resolution (i.e. without dipolar broadening) spectrum of low-abundance spins, such as naturally abundant ^{13}C, by simply decoupling the abundant spins in analogy to solution NMR. Under certain conditions, cross polarization (CP) to transfer polarization from ^{1}H nuclei can help the sensitivity greatly.

In my sdudy, MAS, heteronuclear decoupling and cross polarization were used to achieve NMR signals with high resolution and signal sensitivity. The details of these methods are discussed in the Appendix.

2.4 References

1. A. Abragam, *The Principles of Nuclear Magnetism*, (1961). Oxford University Press.

2. C. P. Slichter, *Principles of Magnetic Resonance*, (1990). Springer-Verlag New York.

3. E. F. Roeder, and S. B. W. Roeder, *Experimental Pulse NMR*, (1981). Addison-Wesley Publishing Company, Inc.

4 J. Haase and D.Freude, *NMR Basic Principles and Progress*. Springner-Verlag, Berlin. **29** (1969).

5. M. Bak, J. T. Rasmussen, and N. C. Neilsen, *J. Magnetic Resonance*, **147,** 296 (2000).

CHAPTER 3

INTRODUCTION OF POLY(ETHYLENE-*CO*-METHACRYLIC ACID IONOMER

3.1 Self-healing Ionomer--Surlyn®

Surlyn® is the random copolymer poly(ethylene-co-methacrylic acid) (EMAA) introduced by DuPont in the early 1960's. The incorporation of methacrylic acid is typically low (< 15mol. %). Some or all of the methacrylic acid units can be neutralized with a suitable cation, commonly Na^+ or Zn^{+2}. Thus, Surlyn is also an ionomer – an ion-containing polymer. The addition of the ionic character to a polymer strongly influences the glass transition temperature, physical and mechanical behaviors, etc. Thus, Surlyn possesses unique mechanical, rheological, and thermal properties, as well as the intriguing property of self-healing following high-speed impact.

When a bullet is shot through a target made of Surlyn, during the impact the energy is passed to the ionomer, heating it locally to the molten state. After the bullet's penetration, it is proposed that the ionic regions maintain their attractions and flow together, patching the hole. It is hoped that these materials might have space applications, primarily for protecting space vehicles from destructive micrometeorite impacts.

Currently, the poly(ethylene-co-methacrylic acid) ionomers with self-healing properties are not space-compatible; the ionomers are not resistant to UV. Understanding the relationship between chemical structure, morphology, and physical properties is of primary importance to both academia and industry. Basic understanding of ionomers has been established over the last 30 years of investigation; yet much still remains to be learned about the properties of ionomers.

3.1.1 Definition of Ionomers

An ionomer is an ion containing polymer with some similar behaviors to polyelectrolytes, especially in solvents with high dielectric constants. In order to differentiate an ionomer from a polyelectrolyte, a new definition was given by Eisenberg and Rinaudo in 1990[1]. The new definition stated that ionomers are “polymers in which the bulk properties are governed by ionic interactions in discrete regions of the material (ionic aggregates)”, and the ionic group content is less than 15% of the polymer.

3.1.2 Composition of Ionomer Surlyn

Ionomers are composed of nonionic repeat units and ionic repeat units. The nonpolar chains are grouped together and the polar ionic groups are attracted to each other, tending to cluster together away from the nonpolar polymer backbone chains.

Surlyn is a sodium salt (which provides the ions) of the copolymers derived from ethylene and methacrylic acid, where the ionic groups are attached to the backbone chain at random intervals.

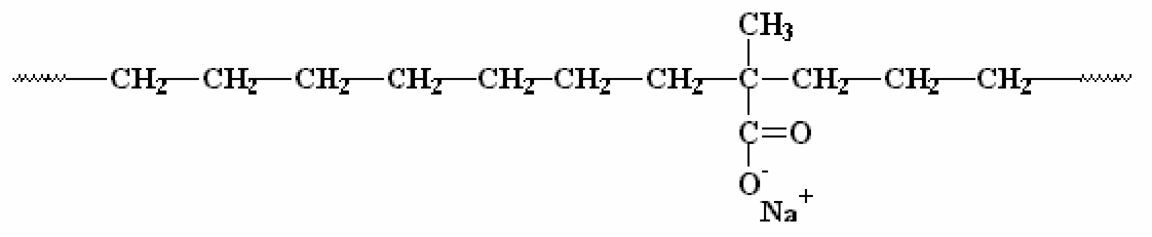

$$\sim\mathrm{CH_2-CH_2-CH_2-CH_2-CH_2-CH_2-CH_2}-\overset{\displaystyle \mathrm{CH_3}}{\underset{\underset{\displaystyle \mathrm{O^{-}\ Na^{+}}}{\mathrm{C{=}O}}}{\mathrm{C}}}-\mathrm{CH_2-CH_2-CH_2}\sim$$

Fig. 3.1 Chemical structure of Surlyn.

The ionic groups (Na^+-O^-) facilitate the formation of ionic aggregates. The ionic aggregates are effectively physical crosslinks, which are reversible and give rise to ionomers with unique characteristics.

3.2 Ionomer Morphology

Over the past two decades, a number of models for the morphology of random ionomers have been proposed, none of which are completely consistent with all of the experimental observations on these materials. The multiplet-cluster model proposed by Eisenberg[2] is now generally accepted. The model is in good agreement with a very wide range of experimentally observed phenomena, especially those based on dynamic mechanical and X-ray scattering techniques.

3.2.1 Multiplets

Defined by Eisenberg[3], a “multiplet” is an aggregate consisting of several ion pairs and containing only ionic material.

With the assumption that multiplets are nearly spherical in shape with less than approximately 10 ion pairs[4], the properties, such as firmness and size, of the multiplets are affected by the strength of the electrostatic interactions between the ion pairs, the ion content of the ionomer, and the characteristics of the host polymer, etc.

Each multiplet is surrounded by a region of restricted chain mobility. This region is formed by the polymer chains anchored by the ion pairs in the multiplet. Hence, the mobility of the polymer chain in the immediate vicinity of a multiplet is expected to be greatly reduced relative to that of those in the bulk polymer. The thickness of the region of restricted mobility surrounding each multiplet is determined largely by the flexibility of the polymer backbone. The more flexible the chain, the thinner the region of restricted mobility. The region is too small to have its own glass transition temperature (T_g), but the multiplet itself would increase the T_g of the polymer.

3.2.2 Clusters

As the ion content is increased, the average distance between multiplets decreases. Eventually some overlap will be encountered among the regions of restricted mobility surrounding each multiplet. When such a region is large enough to have its own T_g, greater than 50-100 Å in dimension, it constitutes a cluster and exhibits behavior characteristic of a phase-separated region.

The clusters could be of any geometry, and there is also no well-defined size or number of ion pairs or multiplets in a cluster. It is not necessary to invoke electrostatic interactions between multiplets within a cluster.

3.2.3 Multiplet—Cluster Model

Based on the SAXS data, a multiplet-cluster model was put forward by Eisenberg[2](Fig. 3.2). Ionic pairs exist as isolated multiplets in the ionomer and raise T_g of the material. As the ion content is increased, the ionic clusters are formed and exhibit a phase-separated behavior, and the second T_g is observed. The intercluster region consists of nonionic chain material, probably ion pairs, individual multiplets, or small aggregates of multiplets which are not large enough to have their own T_g. In case of Surlyn, it consists of three regions: a polyethylene crystalline region, an amorphous region including metal carboxylates and isolated groups such as COOH, and an ionic cluster region.

The formation of the ionic aggregates has a profound influence on the polymer's mechanical, thermal, and other physical properties. Thus, it is crucial to clarify the microscopic structure of the ionic aggregates and understand their effects on physical and improve their applications.

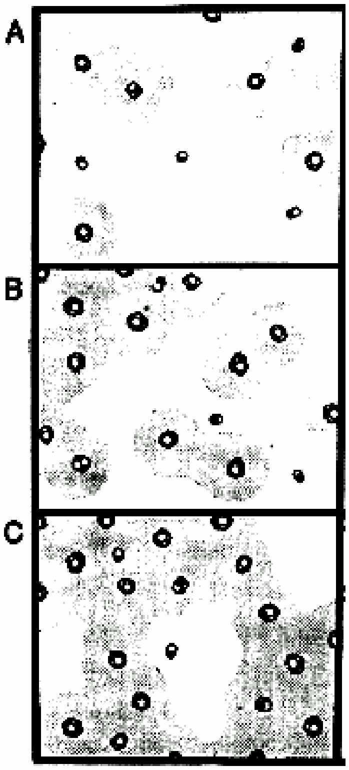

Fig. 3.2 Schematic representation of the morphologies of random ionomers at different ion contents: (A) low ion content; (B) intermediate ion content; (C) high ion content. The shaded areas indicate regions of restricted mobility.[2]

3.3 Influence of Aggregate Formation on Thermal Property

Differential Scanning Calorimetry (DSC) is widely used to characterize the thermal properties of a polymer. DSC is a technique used to study the changes that take place in a polymer when it is heated, which are called the thermal transitions of a polymer. Heat flow, that is heat absorption (endothermic) or heat emission (exothermic), is measured, per unit time with the sample compared to a thermally inert reference. If the sample exhibits a phase change, energy is either absorbed, or emitted. In either case a change in the temperature is detected and the resulting signal is heat flow. The plot produced from the DSC shows heat flow versus the temperature.

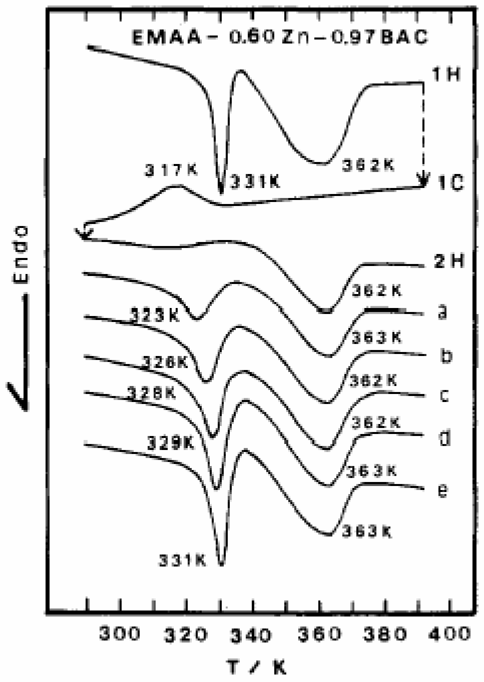

Fig. 3.3 DSC curves for EMAA-0.60Zn-0.97BAC: lH, first heating; lC, first cooling; 2H, second heating; second heating processes after storing for (a) 5 h, (b) 1 day, (c) 3 days, (d) 9 days, and (e) 38 days at room temperature.[5]

Previous DSC study[5], Fig. 3.3 showed that two endothermic peaks are present upon heating of structurally the relaxed (aged) poly(ethylene-co-methacrylic acid (EMAA))- zinc neutralized ionomer system. The higher temperature peak, around 90°C, is attributed to the melting of polyethylene crystalline lamellae. The identity of the low-temperature peak around 50°C remains unclear. This peak is absent in samples immediately after cooling from the melt and recovers after a certain period of structural relaxation at room temperature. It was found that this low-temperature peak is also affected by hydration[6] and stretching.[7]

3.4 Origin of the Low-temperature DSC Peak—Proposed Models

3.4.1 Order-disorder Transition of Ionic Clusters

Based on their thermal expansion and DSC results, Yano *et al.*[5] proposed that the ionic clusters are ordered assemblies of ionic group (ionic crystallites) and show an order-disorder transition near 50°C. Fig. 3.4 shows a model illustrating this order-disorder transition (T_i) of the ionic clusters.

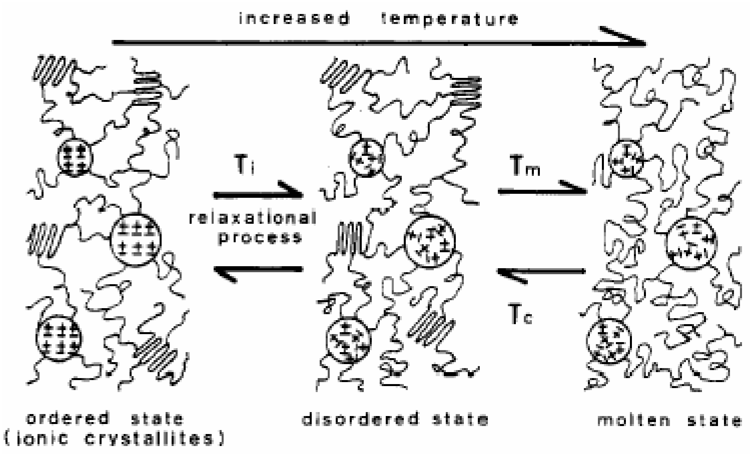

Fig. 3.4 Model for the order-disorder transition of ionic clusters.[5]

The original sample consists of three phases: ionic clusters, a polyethylene crystalline region, and an amorphous region. When the temperature is increased from room temperature, the crystal-like order inside the ionic clusters is destroyed at T_i, giving a disordered state, and on further increasing the temperature, the polyethylene crystallites melt at T_{m}, but the disordered ionic clusters still exist. In the cooling process from the temperature above T_{m}, the crystallization of polyethylene regions take place at T_{c}, but the ordering in the ionic clusters does not appear down to room temperature. However, upon storing the sample below T_{i}, the disordered ionic clusters very slowly change to the ordered ones; this slow change results from the relaxation process with long relaxation time. The annealing studies showed that the new order-disorder peak did not shift with annealing temperature, and was therefore not due to melting of quasi-crystallites in the polyethylene matrix regions. Similar results were reported by Kutsumizu *et al*[6] for an EMAA-sodium neutralized ionomer system.

3.4.2 Destruction of Ordered Structure Surrounding the Ionic Clusters

Murakami *et al*.[7] studied the changes in ordered structure of Na neutralized Surlyn polymer under deformation by observing DSC and Small Angle X-ray Scattering (SAXS). It was reported that T_i peak of Na ionomer disappeared after deformation (stretching) and there was no change in the T_m peak. The disappearance of secondary melting point (Ti) in Na ionomers was due to the destruction of ordered structure surrounding the ionic aggregate.

Clearly, much still remain to be learned about the structure of the ionic aggregates, the influence of ionic aggregates on physical properties of the ionomer, and the effects of temperature, relaxation and impact deformation on the aggregate local structure and dynamics. **In Chapter 4**, I will discuss the experimental results of the thermal properties obtained by differential scanning calorimetry (DSC) and the microscopic structures obtained by nuclear magnetic resonance (NMR). It is found that although the thermal properties change significantly, the structure and dynamics of ionic aggregates (consists of Na^+-O^- pairs) remain unchanged under aging and mechanical deformation. The distance between Na^+ ions was also estimated.

3.5 References

1. A. Eisenberg, and M. Rinaudo, *Polymer Bull*, **24**, 671 (1990).

2. A. Eisenberg, B. Hird, and R. B. Moore, *Macromolecules*, **23**, 4098 (1990).

3. A. Eisenberg, *Macromolecules*, **3**, 147 (1970).

4. A. Eisenberg, and J-S. Kim, *Introduction to Ionomers.* Wiley&Sons, Inc., 327 (1998).

5. K. Tadano, E. Hirasawa, H. Yamamoto, S. Yano, *Macromolecules*, **22**, 226 (1999).

6. S. Kutsumizu, N. Nagao, K. Tadano, H. Tachino, E. Hirasawa, and S. Yano, *Macromolecules*, **25**, 6829 (1992).

7. H. Akimoto, T. Kanazawa, M. Yamada, S. Matsuda, G. O. Shonaike, A. Murakami, *J. Appl. Polymer Science*, **81**, 1712 (2001).

CHAPTER 4

STRUCTURE AND DYNAMICS OF IONIC MULTIPLETS IN SURLYN®

The previous studies of the chemical structure and physical properties of Surlyn® are reviewed in **Chapter 3**, including the microstructure models proposed mainly based on small angle X-ray scattering (SAXS) data. Yet much still remains to be learned about the properties of the polymer. In this chapter, I will discuss the experimental results of thermal properties obtained by differential scanning calorimetry (DSC) and microscopic structures obtained by nuclear magnetic resonance (NMR).   .

4.1 Experimental Details

4.1.1 Sample Preparation

Surlyn® 8920 (E-0.054MAA-0.6Na), which contains 5.4 mol% MAA and is 60% neutralized by sodium, was used in this investigation. Samples were first heated in quartz tubes under dynamic vacuum at 423 K for 1.5 hours. After that, the samples were quenched under vacuum by ice water. The quenched samples were divided into four groups. The first group of samples, referred to here as quenched samples, were sealed in quartz tubes under vacuum followed by (typical delay of 1 hour) DSC and NMR measurements. The second group, referred to here as relaxed samples, were sealed in a quartz tube under vacuum and kept at room temperature for one month before DSC and NMR measurements. The third group, referred to here as relaxed-compressed samples, were prepared by compressing the relaxed samples under a pressure of 275 MPa for 1 minute. During the compression treatment, these samples were exposed to air for about 1 hour followed immediately by DSC or NMR measurements. The effect of moisture here should be negligible since we did not observe any noticeable changes by DSC and NMR in quenched-relaxed samples upon 1 hour exposure to air. The fourth groups, referred to here as hydrated samples, were relaxed samples placed in a closed container under saturated water vapor at room temperature for four days. Water uptake in these samples was determined by the weight increase as a function of time. The water uptake in the hydrated samples after four days of hydration is 2.6 wt%, corresponding to 1.4 H_2O molecules per Na^+ ion. The saturated level of water uptake is 7.9 wt%, which corresponds to 4.2 H_2O molecules per Na^+ ion.

4.1.2 Measurements

NMR is a sensitive probe of local structures and dynamics. ^{23}Na NMR provides a natural probe of the structure and dynamics of ionic multiplets in E/MAA neutralized by sodium. In this study, NMR and DSC were employed to investigate the structure and dynamics of ionic multiplets.

DSC measurements were carried out using a PerkinElmer Pyris 1 with a scanning rate of 10 K/min. Indium and tin were used as calibration standards.

NMR measurements were carried out using pulsed spectrometers. Unless explicitly mentioned, results were obtained at a magnetic field of 9.4 T. To study the field dependence some spectra were recorded at a magnetic field of 4.7 T. Dilute aqueous NaCl solution was used as the ^{23}Na chemical shift reference. The typical nonselective 90^o pulse is 4.3 μs as determined in aqueous NaCl. With selective excitation (considering only the central transition ($\frac{1}{2} \leftrightarrow -\frac{1}{2}$)), ^{23}Na spectra were recorded using either 1 pulse or the spin echo sequence (90^{o}–*t*–180^{o}–*t*–detection). An Oxford continuous flow cryostat was used for NMR measurements at and below room temperature and a homemade high-temperature probe was used for measurements at and above room temperature.

4.2 Results and Discussion

4.2.1 Thermal and Dynamic Properties of Ionic Multiplets and Assignment of the Low Temperature DSC Peak

By comparing changes of thermal properties and ^{23}Na NMR spectra under various sample conditions, such as structural relaxation, mechanical deformation, and hydration, information on the relationship between thermal properties and the microstructure and dynamics of ionic multiplets was obtained; we also got a better understanding of the assignment of the low temperature DSC peak.

Fig. 4.1 shows the DSC curves of the various samples examined in this study. The first heating curve of the relaxed sample shows the two characteristic endothermic peaks, one at 329 K and the other at 364 K. The second heating curve, following immediately after the first, only shows the peak at 364 K. As is well known, the peak at 329 K reappears after a certain time of structural relaxation at room temperature. As expected, the quenched sample shows only a very weak endothermic peak at 323 K along with the higher temperature endothermic peak. Since a delay of 1 hour occurred after quenching before the DSC measurement was carried out for the quenched sample, partial recovery of the low-temperature endothermic peak took place. This peak grows in intensity and moves to higher temperature as a function of relaxation time. As reported earlier, no further change occurs after 30 days of relaxation. Figure 4.1 shows that hydration has a significant effect on the low-temperature endothermic peak as reported earlier.[1] The peak intensity decreases and the peak position moves to lower temperature, 317 K, upon hydration. Similarly, compression also has a dramatic effect on this low-temperature peak, which nearly disappeared after compression as shown in Fig. 4.1.

Fig. 4.2 shows the ^{23}Na NMR spectra at 190 K. The spectra of quenched, relaxed, and relaxed-compressed samples are all identical within errors with linewidth at half-height (LWHH) of 9.5±0.3 kHz. The peak for the hydrated sample is narrower with LWHH of 8.4±0.3 kHz. Fig. 3.3 shows the temperature dependence of the linewidth of the non-hydrated samples up to 580 K along with the hydrated sample data. For the hydrated sample the linewidth decreases rapidly above 210 K and reaches a minimum value of 3.0±0.3 kHz at 255 K. Upon further increase of temperature, the motional narrowing is followed by a slight increase of the linewidth to 3.7±0.3 kHz at 275 K (possibly due to motions with rate becoming comparable to ^{23}Na Larmor frequency[2] of 105.76 MHz), and then drops again to 3.2±0.3 kHz upon further heating. For the three non-hydrated samples the linewidth decreases dramatically above 300 K instead of 210 K as in the hydrated sample. It drops to a minimum of 2.5 kHz at 375 K, followed by an increase to 4.0 kHz at 500 K, where the rate of motion reaches the ^{23}Na Larmor frequency,[2] and then drops again. Fig.4 3 shows clearly that the linewidth at 190 K is determined exclusively by the structural environment around the Na atoms, since the rapid thermal fluctuation of the surrounding molecules is eliminated.

The linewidth at 190 K and below is determined by spin interactions including chemical shift, dipolar interactions, and quadrupolar interactions. Fig. 4.2 shows that there are no noticeable differences in structure that are detectable by static ^{23}Na spectra in the three non-hydrated samples, in contrast to the significant change in the low-temperature DSC peak upon relaxation and compression. Fig. 4.3 shows that the three non-hydrated samples exhibit very similar line narrowing behavior in the temperature range of 320~330 K where the low-temperature DSC peak appears. This indicates that molecular motions of ionic multiplets are not affected significantly by relaxation or compression. Moreover, the ^{23}Na linewidth of non-hydrated samples is reversible versus measurement temperature whereas the low-temperature DSC peak has a very long relaxation time and recovers fully only after a few weeks of relaxation at room temperature. Thus, the change of the low-temperature DSC peak is not directly related to either structural changes, such as an order-disorder transition, or changes of dynamical properties of ionic multiplets. On the other hand, when ionic multiplets are affected by hydration, as evidenced by ^{23}Na NMR, the low-temperature DSC peak also shows significant change. This is consistent with the picture that the low-temperature DSC peak is related to structure in proximity to ionic multiplets. A similar conclusion was drawn based on other experiments.[3]

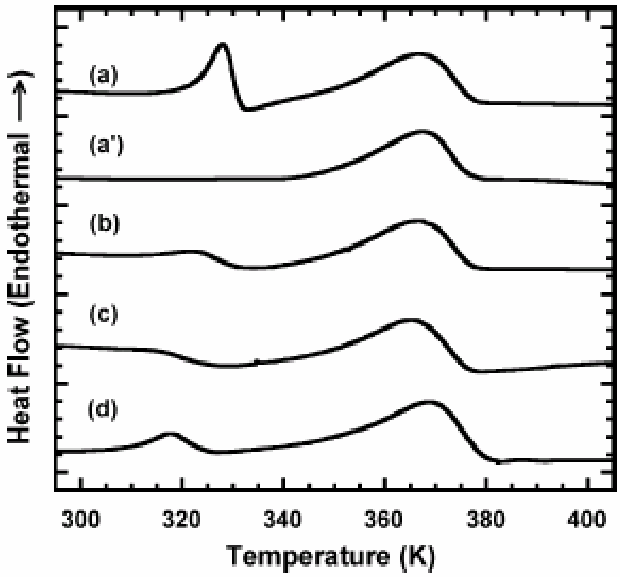

Fig. 4.1 DSC results for various samples: (a) relaxed sample; (a′) second heating of relaxed sample; (b) quenched sample; (c) relaxed-compressed sample; (d) hydrated sample.

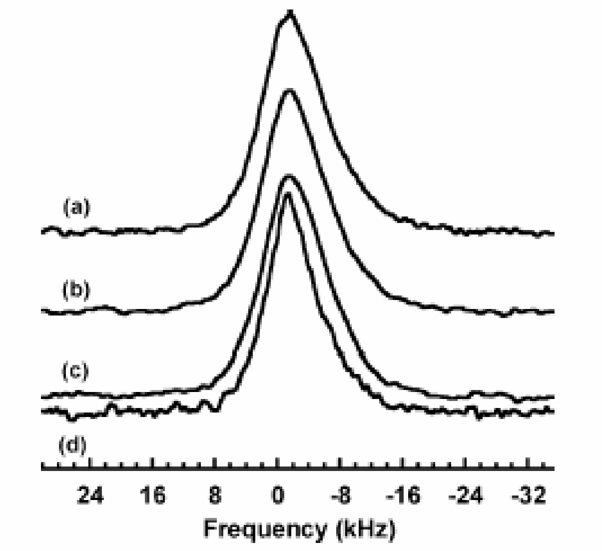

Fig. 4.2 ^{23}Na NMR spectra for various samples at 9.4 T and 190 K: (a) relaxed sample; (b) quenched sample; (c) relaxed-compressed sample; (d) hydrated sample.

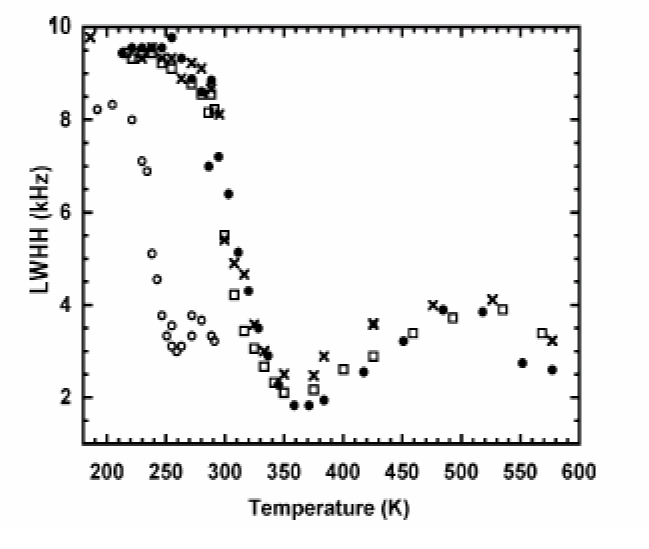

Fig. 4.3 ^{23}Na LWHH (linewidth at half height) for various samples versus temperature. (●) relaxed sample; (×) quenched sample; (□) relaxed-compressed; (○) hydrated sample.

4.2.2 Structure Study of Ionic Multiplets in Surlyn® through Quadrupole Interaction Calculation

One of the connections between ^{23}Na NMR spectra and structure is through quadrupole interactions. Fig. 4.4. shows the ^{23}Na NMR spectra of the hydrated sample at 190 K obtained at magnetic fields of 4.7 and 9.4 T. The linewidth at 4.7 T is 10.7 kHz which is broader than that at 9.4 T, a clear indication that the second-order quadrupole broadening contributes significantly to the linewidth according to Eq. (2.8).

The ^{23}Na spectra observed at 4.7 T and 9.4 T can be fit (lineshape simulations by SIMPSON[4] of both spectra shown in Fig. 4.4.) with χ = 1.71 MHz and η = 0.5 as shown in Fig. 4.4. The narrower linewidth of the hydrated sample at 190 K compared to that of non-hydrated samples indicates that hydration causes a reduction of the EFG at Na sites.

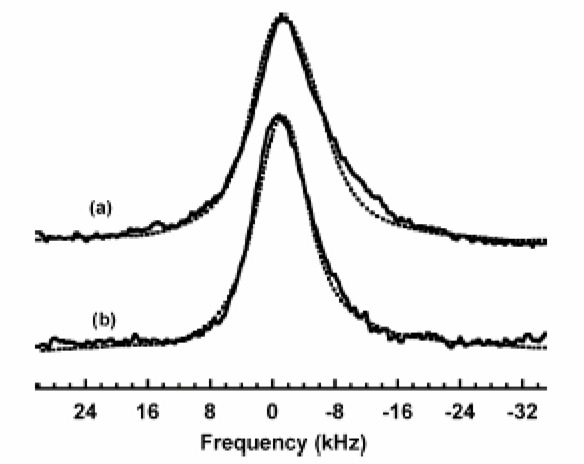

Fig. 4.4 ^{23}Na NMR spectra for the hydrated sample at 190 K in field of 9.4 T and 4.7 T and simulation curves (dotted lines). (a) 4.7 T, LWHH=10.7 kHz; (b) 9.4 T, LWHH-8.4 kHz.

4.2.3 Composition Analysis of Ionic Multiplets in Surlyn® via Second Moment (M_2) Calculation

As mentioned earlier, the dipolar interaction between two nuclear spins depends on the magnitude and orientation of their magnetic moments and also on the length and orientation of the vector describing their relative positions. To investigate the microscopic composition of the ionic multiplets, the transverse magnetic relaxation was measured by spin-echo decay and the interatomic distances between Na^+ and O^- in the multiplets were calculated via second moment analysis.

Fig. 4.5. shows the spin-echo decay curves of quenched, relaxed, relaxed-compressed, and hydrated samples at 260 K. M_{2E} for each sample was calculated according to Eq. (2.13). Within errors, all the non-hydrated samples have the same value of M_{2E} and the hydrated sample has slightly larger M_{2E}. A possible reason for the slightly larger M_{2E} for the hydrated sample is that the excitation might be slightly nonselective due to the smaller quadrupolar interaction. Using the measured second moment and assuming a multiplet consisting of 13 Na and 13 O atoms with a NaCl-type structure shown in Fig. 4.6., the nearest neighbor Na-Na distance $d_{\text{Na-Na}}$ can be estimated according to Eq. (2.11). The estimated Na-Na distance, the corresponding Na-O distance $d_{\text{Na-O}}$, and the measured M_{2E} value are listed in Table 4.1 for the four samples. For non-hydrated samples, based on a NaCl-type structure, a $d_{\text{Na-Na}}$ of 3.17 Å is derived yielding a distance $d_{\text{Na-O}}$ between Na and O of $3.17/\sqrt{2} = 2.24$ Å.

The identical M_{2E} values of the non-hydrated samples indicate that ionic multiplets remain unchanged after a long time of relaxation or compression. The calculated Na-O distance increases slightly if a larger multiplet is considered. In the limit of an infinite NaCl-type lattice (this is of course not a real multiplet), the calculated $d_{\text{Na-Na}}$ and $d_{\text{Na-O}}$ are 3.57 Å and 2.52 Å, respectively. Compared to the well-known ionic radius of Na and O, 1.02 Å and 1.4

Å, respectively, the measured Na-Na distance $d_{\text{Na-Na}}$ agrees very well with multiplet structures with close-packed Na^+-O^- ionic pairs.

Table 4.1. M_{2E} values, the calculated Na-Na distances $d_{\text{Na-Na}}$ and the corresponding Na-O distances $d_{\text{Na-O}}$.

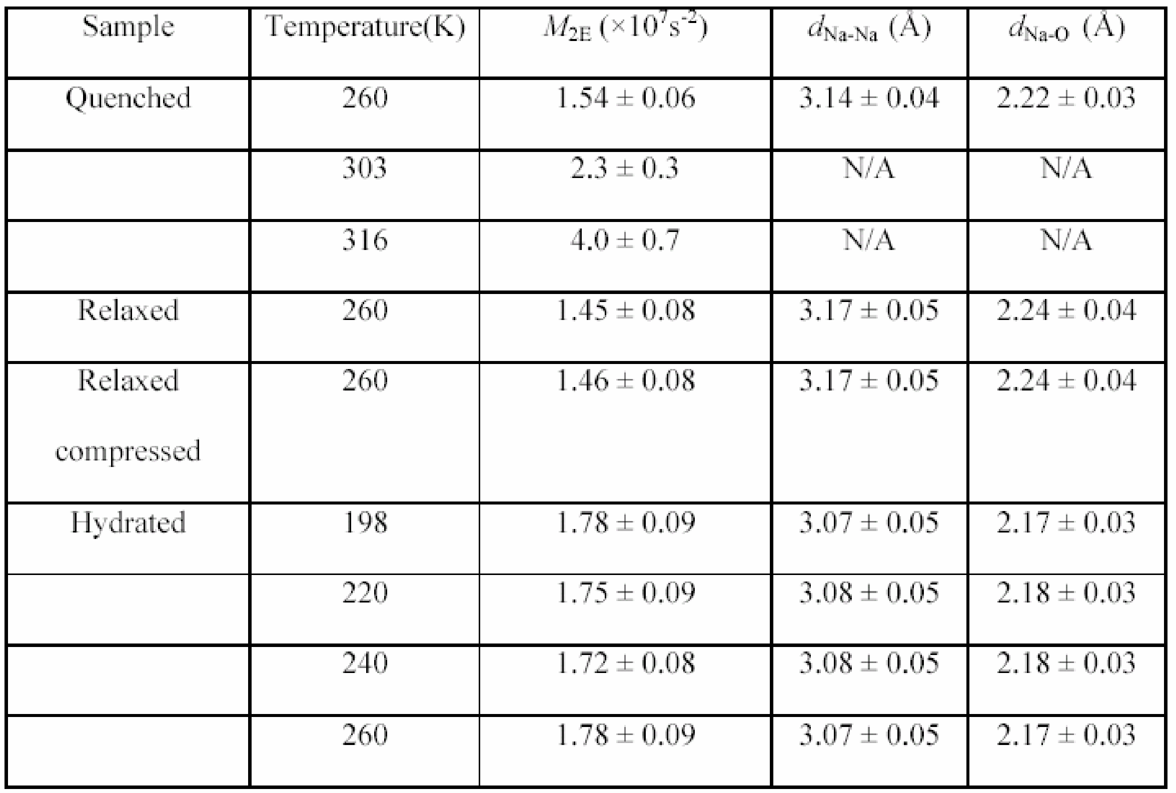

Sample	Temperature(K)	M_{2E} ($\times 10^7 \text{s}^{-2}$)	$d_{\text{Na-Na}}$ (Å)	$d_{\text{Na-O}}$ (Å)
Quenched	260	1.54 ± 0.06	3.14 ± 0.04	2.22 ± 0.03
	303	2.3 ± 0.3	N/A	N/A
	316	4.0 ± 0.7	N/A	N/A
Relaxed	260	1.45 ± 0.08	3.17 ± 0.05	2.24 ± 0.04
Relaxed compressed	260	1.46 ± 0.08	3.17 ± 0.05	2.24 ± 0.04
Hydrated	198	1.78 ± 0.09	3.07 ± 0.05	2.17 ± 0.03
	220	1.75 ± 0.09	3.08 ± 0.05	2.18 ± 0.03
	240	1.72 ± 0.08	3.08 ± 0.05	2.18 ± 0.03
	260	1.78 ± 0.09	3.07 ± 0.05	2.17 ± 0.03

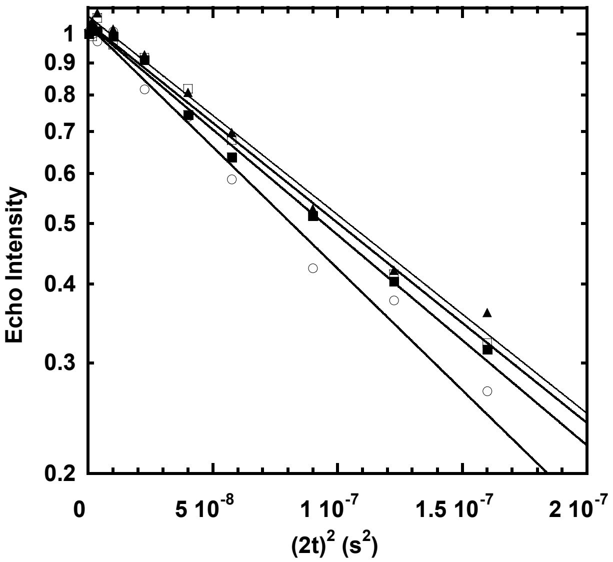

Fig. 4.5 Time dependence of the Hahn-echo intensities of various samples at 260K. (▲) relaxed sample, $M_{2E} = 1.45 \times 10^7 s^{-2}$; (■) quenched sample, $M_{2E} = 1.54 \times 10^7 s^{-2}$; (□) relaxed-compressed sample, $M_{2E} = 1.46 \times 10^7 s^{-2}$; (○) hydrated sample, $M_{2E} = 1.78 \times 10^7 s^{-2}$.

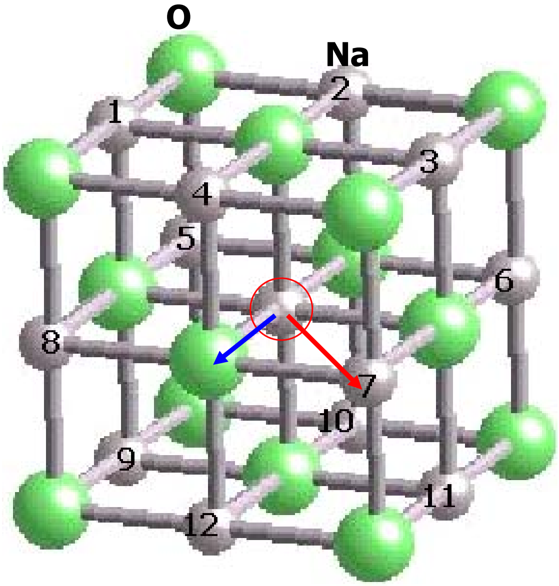

Fig. 4.6 Model of ionic multiplets using NaCl (simple cubic) structure.

4.2.4 Dynamic Mechanism of Motional Narrowing of ^{23}Na NMR Line Width

As mentioned earlier, rapid relative motion of the molecules or their surroundings can diminish the quadrupole interaction of the nucleus and the dipolar interaction between two nuclear spins, which are the dominant mechanisms for line broadening, and lead to NMR line narrowing.

As shown in Fig. 4.3., hydration has a significant effect on the motional narrowing of the ^{23}Na line width above 210 K, while the three non-hydrated samples exhibit similar line narrowing behavior in the temperature range of 320-330 K. To investigate the mechanism of this effect, M_{2E} values were measured at the temperatures where the dramatic line narrowing occurs.

Fig. 4.7. shows the spin-echo decay curves of the hydrated sample at 198, 220, 240 and 260 K. Surprisingly, the slope of the echo decay remains unchanged over this temperature range despite the significant line narrowing that occurs. This shows clearly that the atomic motion that leads to the initial reduction of the linewidth is of much higher frequency compared to the timescale of the transverse relaxation. For instance, vibrations of water molecules around Na atoms could cause such changes. Another evidence of such fast motions is given by the spin-lattice relaxation time denoted by T_1, which is defined as the time constant which describes how M_Z returns to its equilibrium value. T_1 depends on the nuclei and their molecular surroundings, including parameters such as temperature and viscosity. It is a probe to investigate the effects induced by rapid thermal fluctuation of the surrounding molecules. At 170 K, T_1 is 39.5 ms which decreases quickly to 7.7 ms at 220 K. Since motion-induced spin-lattice relaxation is most effective for motions with frequency approaching the Larmor frequency, it is too fast to be detected by the transverse relaxation

which has a timescale of a few hundred microseconds. The onset of this NMR-detected fast motion of water molecules could eventually lead to other modes of motion of water molecules, such as those detected by dielectric loss measurement,[5] which contribute further to motional narrowing.

Figure 8 shows the Hahn-echo decay curves of the quenched sample at 260 K, 303 K and 316 K, which are the characteristic temperatures over the range of the dramatic line narrowing. The decay rate of the Hahn echo starts to increase gradually above 260 K. Here, the motion contributing to motional narrowing also contributes to the decay rate of the Hahn echo, unlike in the hydrated sample below 260 K. Therefore, this is attributed to the typical onset of slow motion with increasing rate as temperature increases. The timescale of such slow motion, which causes changes of the Na local environment (and thus the resonance frequency of ^{23}Na), becomes comparable to the transverse relaxation timescale of a few hundred μs associated with dipolar interactions and causes additional decay of the Hahn echo. Therefore, the decay rate of the Hahn echo reflects not only dipole-dipole interactions but also slow motion. This shows clearly that the line narrowing of the quenched sample above 300 K is due to slow motions of Na^+ ions, such as hopping and possibly motions of the polymer backbone. The timescale of such motions is a few hundred μs around 300 K.

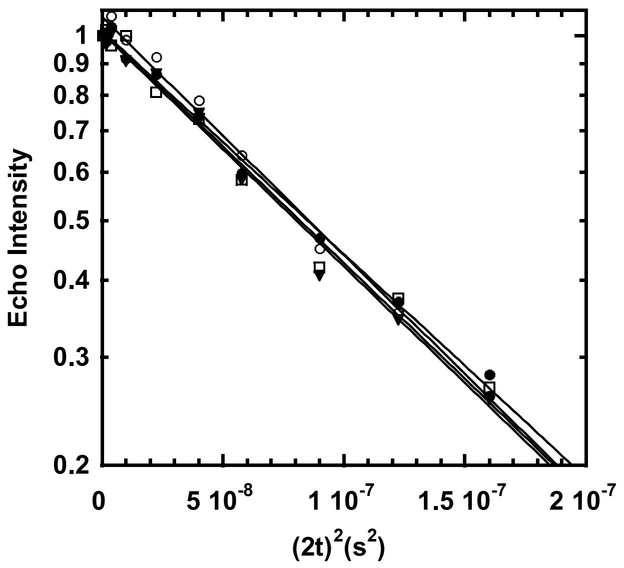

Fig. 4.7 Hahn-echo decay curves of the hydrated sample at 198, 220, 240 and 260 K. (○) 198 K, $M_{2E} = 1.78 \times 10^7 s^{-2}$; (▼) 220 K, $M_{2E} = 1.75 \times 10^7 s^{-2}$; (●) 240 K, $M_{2E} = 1.72 \times 10^7 s^{-2}$; (□) 260 K, $M_{2E} = 1.78 \times 10^7 s^{-2}$.

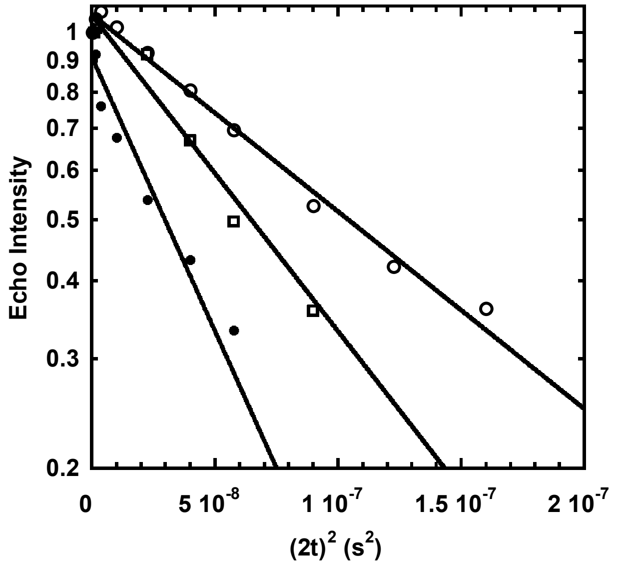

Fig. 4.8 The Hahn-echo decay curves of the quenched sample at 260 K, 303 K and 316 K. (○) 260K, $M_{2E} = 1.54 \times 10^7 s^{-2}$; (□) 303K, $M_{2E} = 2.3 \times 10^7 s^{-2}$; (●) 316K, $M_{2E} = 4.0 \times 10^7 s^{-2}$.

4.3 Conclusions

The structure and dynamics of ionic multiplets were investigated by ^{23}Na NMR and DSC. The low-temperature DSC peak is related to structure in proximity to ionic multiplets, instead of multiplets themselves. Under relaxation and compression, no detectable changes of structure and dynamics of ionic multiplets were observed by ^{23}Na NMR, but hydration did change the local environment and dynamics of ionic multiplets. The nearest-neighbor distance between Na^+ ions was determined to be 3.17 to 3.57 Å by NMR which gives an estimated Na^+-O^- distance of 2.24 to 2.52 Å. This agrees very well with an ionic multiplet structure consisting of close-packed Na^+-O^- ionic pairs. The timescale of Na motion, possibly hopping, was determined to be on the order of a few hundred μs near 300 K.

We report the first direct measurement of the multiplet structure in ethylene-methacrylic acid ionomers using ^{23}Na NMR. Combined with DSC results, it shows that the model of the ionic multiplets' order-disorder transition during heating is incorrect. The results on the dynamic properties of Na^+ ions and their temperature dependence contribute significantly to the understanding of the intriguing self-healing property, which is believed closely related to the interactions between Na^+-O^- ion pairs. The results were published in *Macromolecules,* **38** 2781 (2005).

4.4 References

1. S. Kutsumizu, N. Nagao, K. Tadano, H. Tachino, E. Hirasawa, and S. Yano, *Macromolecules*, **25**, 6829 (1992).

2. A. J. Vega, *Encyclopedia of Nuclear Magnetic Resonance*, 3874 (1996). John Wiley New York.

3. H. Akimoto, T. Kanazawa, M. Yamada, S. Matsuda, G.O. Shonaike, and A. Murakami, *J. Appl. Polymer Science*, **81***,* 1712 (2001).

4. M. Bak, J. T. Rasmussen, N. C. Nielsen, *J. Magnetic Resonance*, **147**, 296 (2000).

5. S. Yano, K. Tadano, N. Nagao, S. Kutsumizu, H. Tachino, and E. Hirasawa, *Macromolecules*, **25**, 7168 (1992).

CHAPTER 5

INTRODUCTION TO TITANATE NANOTUBES

Due to its high physical and chemical stability, titanium dioxide (TiO_2) is extensively studied as a photocatalyst for photolysis of water[1-4] and decontamination of wastewater[5], and as a constituent solar cells.[3, 6-12] Titanate nanocrystals have been used in many of these studies, mainly to take advantage of their large specific surface area (45m^2/g for anatase nanoparticles with average size of 32 nm)[3, 6-12]. Since intrinsic TiO_2 possesses a large band gap of 3.2 eV, the solar energy conversion efficiency of TiO_2 is limited. Surface modifications are essential to improve the efficiencies for TiO_2-based solar photoconversion. Dye sensitization is one of the most effective approaches of such surface modification.[6, 9, 11, 13, 14] Attachment of bidentate charge-transfer ligands on small nanocrystal surfaces is another.[15-19]

A new form of titanate nanostructure was discovered in 1998, the tubular nanotube, referred here as to titanate nanotubes. Titanate nanotubes combine the properties and applications of conventional TiO_2 nanoparticles (e.g., wide band gap, photocatalysis) with the properties of layered titanates (e.g. ion exchange). Owing to their larger surface area (293 m^2/g)[20, 21] and higher photoactivity[22] than titania nanocrystals, titanate nanotubes have great potential for applications including photocatalysis and solar cells. However, its wide band gap, 3.7 eV, limits the solar conversion efficiency in photovoltaic applications. It was reported[19] that 40% of Ti atoms in such nanotubes are undercoordinated, which could present problems for electron transport. Surface modification, e.g. attachment of charge-transfer ligands, is one of the most effective approaches to modify the optical absorption spectrum and restore the sixfold coordination of Ti sites. Understanding the microstructure of titanate nanotubes and their properties is of great importance in order to predict, control and direct the surface modification process. However, up to now, the structure and the formation mechanism of titanate nanotubes have not been clarified. It was reported [19] that the coordination geometry of Ti atoms in titanate nanotubes differs from that in bulk TiO_2, and is surprisingly similar to that of 2 nm diameter nanoparticles.

In this chapter, a review of previous studies about titanate nanotubes is presented, including the synthesis, proposed structures, formation mechanism and properties, especially surface properties. The surface properties of titanate nanotubes, especially surface chemistry, are discussed based on those of TiO_2 nanoparticles. Some important applications of titanate nanotubes are briefly mentioned at the end of this chapter.

5.1 Synthesis of Titanate Nanotubes by Hydrothermal Method

The innovative work was inspired by the fact that TiO_2-based powders doped with a small amount of SiO_2 prepared by the sol-gel method[23, 24] with subsequent heat treatment have large specific surface area, 150 m^2/g.[25] In 1998-1999, Kasuga *et al.* reported that high-quality titanate nanotubes with uniform diameters (~10 nm) could be produced via a simple hydrothermal treatment of crystalline TiO_2 particles with NaOH aqueous solutions.[25, 26] When TiO_2-SiO_2 powder produced by the sol-gel method was treated with an aqueous solution of 10 M NaOH for 20 h at 110 °C and then treated with HCl aqueous solution and distilled water, nanotubes with an inner diameter of 5 nm, an outer diameter of 8 nm, and a length of 100 nm were obtained (Fig. 5.1).[25] It was proved that SiO_2 plays no role in the formation of TiO_2 nanotubes.[25]

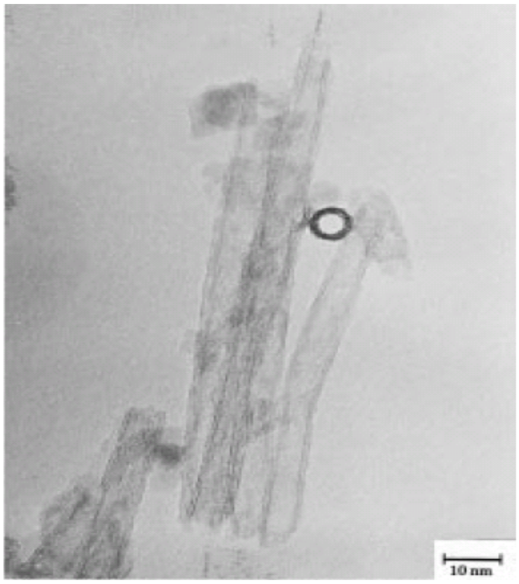

Fig. 5.1 TEM photograph of $80TiO_2 \cdot 20SiO_2$ (in mol %) powders treated with 10 M NaOH aqueous solution for 20 h at 110 °C.[25]

Currently, the nanotube preparation method is basically the same as described above, and a few modifications have been made to improve the yield and the structure of the titanate nanotubes.[21, 27-29] In a typical experiment TiO_2 powder with particle sizes from 80 to 200 nm was added in a 10 M NaOH aqueous solution. The specimen was transferred into a sealed Teflon container and statically heated in a furnace at 130°C for 72 h for producing high quality nanotubes. The white powder was filtered and washed with deionized water at room temperature until the pH reached about 7. A narrow distribution of the average diameter (~7 nm) and of the number of shells (~4) of the nanotubes were obtained, as shown in Fig. 5.2.[30]

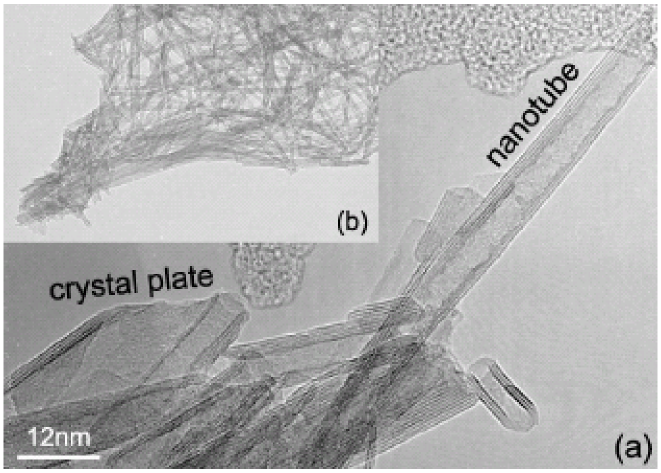

Fig. 5.2 (a) HRTEM image showing $H_2Ti_3O_7$ plates coexist with nanotubes after reaction of TiO_2 with NaOH for 24 h. The inset (b) shows a low-magnification TEM image of the nanotubes after the reaction for three days.[30]

5.2 Morphology of Titanate Nanotubes

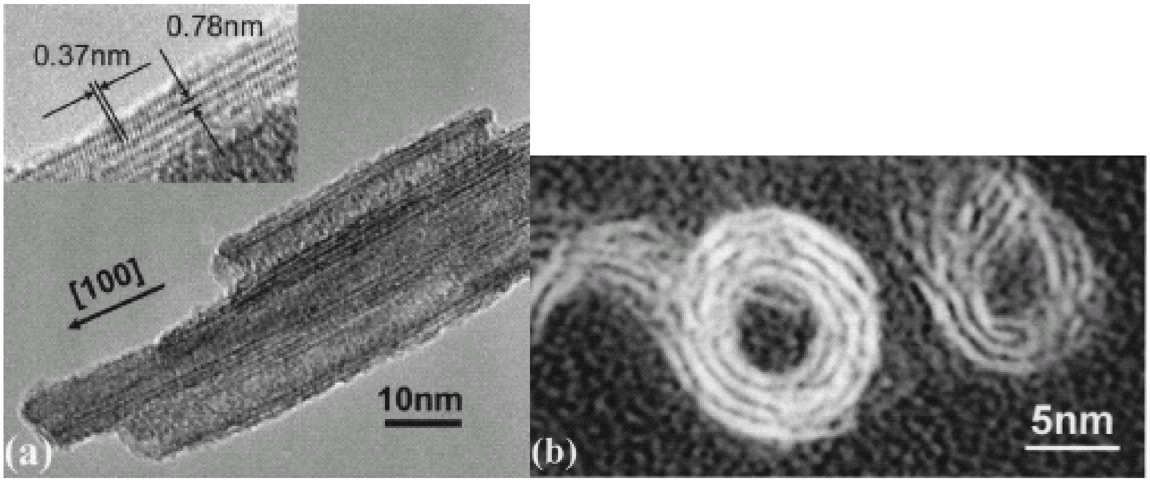

Fig. 5.3 (a) HRTEM images of TiO_2 nanotubes. Left inset is the enlarged picture of the tube wall. (b) Cross-sectional view of TiO_2 nanotubes.[28]

The typical microstructure of titanate nanotubes is illustrated by HRTEM images shown in Fig. 5.3(a).[28] Most tubes are open ended. The numbers of walls counted from the two sides of the tube are usually not identical, as can be seen in this image. Moreover, the wall thickness generally varied along the tube. The left inset in Fig. 5.3(a) is an enlarged picture of the tube wall. The interspacing of the tube walls was 0.78 nm. Figure 5.3(b) is a cross-sectional image (negative picture) of two nanotubes and clearly reveals the arrangement of the tube walls (the white fringes). It was inferred from this image that titanate nanotubes were formed by rolling up the single-layer sheets.

5.3 Structure of Titanate Nanotubes

Titanate nanotubes synthesized by the hydrothermal method have well-defined X-ray diffraction (XRD) patterns. Up to now, the understanding of the crystal structure and formation mechanism of titanate nanotubes is incomplete. It was reported that the structure of the nanotubes was concluded to be either anatase phase[25] or anatase-rutile phase[31]. Another group claimed[21] that the tubular material is not consistent with that of TiO_2, and the atomic ratio of Ti/O various from tube to tube. Here, the proposed crystal structures of titanate nanotubes, e.g. tritiananate $H_2Ti_3O_7$[27, 30, 32] orthorhombic nanotubes[33], and lepidocrocite titanate[34, 35], are reviewed. In this dissertation, the term "titanate nanotubes" is used throughout for simplicity. Our results shown in Chapter 6 indicate that the structure of the titanate nanotubes is closely related to anatase. It is possible that the tubular structure is an anatase phase. Much effort has been put into the investigation of titanate nanotube structures in order to gain insight into their formation mechanism.[21, 27-30, 34] An understanding of their structural characteristics may also be helpful for exploring the nanotube synthesis and formation mechanism.

5.3.1 Trititanate Nanotubes

The model of trititanate nanotubes is proposed by Peng and co-workers based on information from powder X-ray diffraction (XRD), selective-area electron diffraction (SAED), and high-resolution electron microscopy (HRTEM) data.[21, 27, 30, 32]

They proposed that the crystal structure of titanate nanotubes corresponded to layered trititanic acid ($H_2Ti_3O_7$) with a monoclinic crystal structure. A schematic showing the crystal structure of monoclinic trititanic acid in a TiO_6 edge-sharing octahedron representation is shown in Figure 5.4; the three different projections correspond to the crystallographic axes. A nanotubular morphology of layered trititanic acid can by obtained by rolling several (100) planes around axis [010] or [001]. It has been proposed[21] that rolling of the plane occurs around the [010] axis such that the axis of the nanotube is parallel to the *b*-axis of monoclinic $H_2Ti_3O_7$. Using the layered structure of $H_2Ti_3O_7$ as the basis of the model, the structural model is shown in Fig. 5.4(d). A typical X-ray diffraction (XRD) pattern of titanate nanotubes together with a simulated XRD profile using the trititanate nanotube model is shown in Figure 5.5.

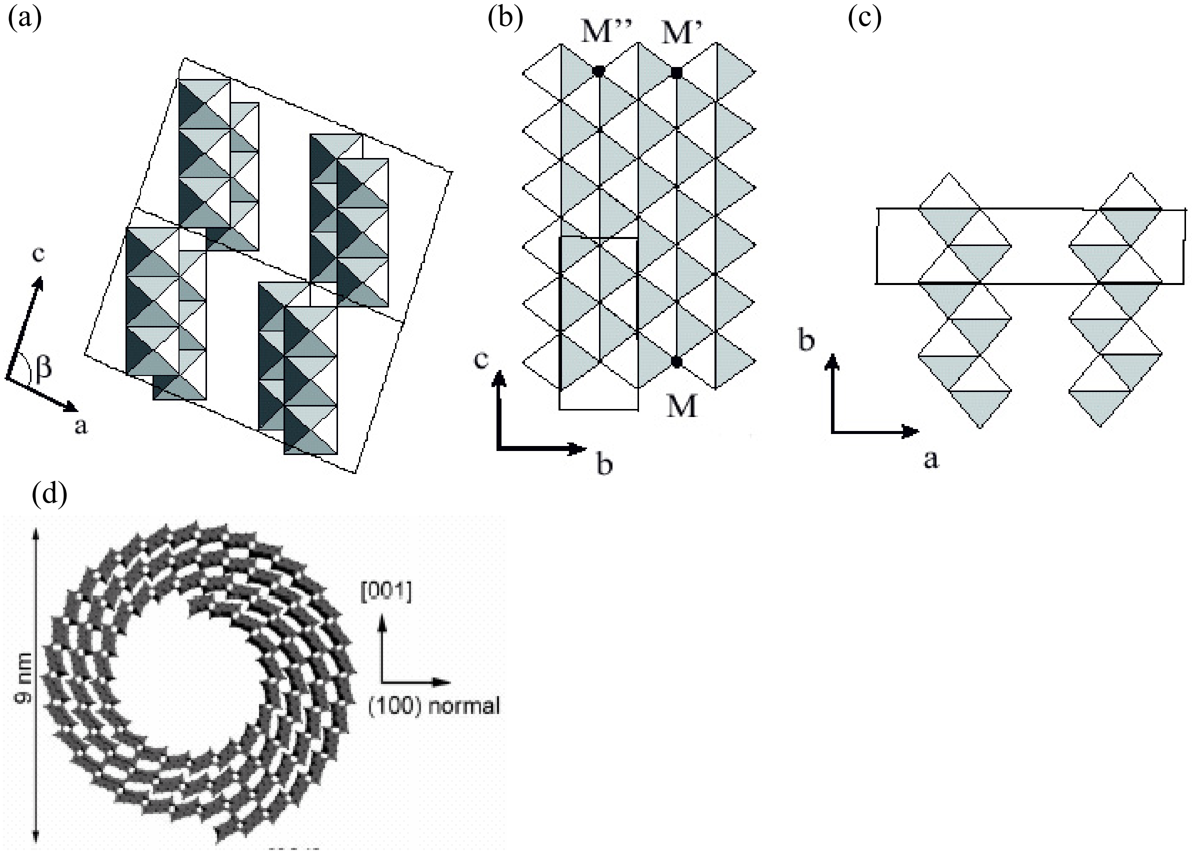

Fig. 5.4 Crystal structure of monoclinic trititanic acid ($H_2Ti_3O_7$) in three different projections in octahedral presentations (a), (b), (c), with lattice parameter a=1.602 nm, b=0.375 nm, c=0.919 nm. The solid line shows the dimension of a unit cell. Connection of point M to point M′ results in the formation of nanotubes with chirality equal to zero. (d) the structure of the trititanate nanotube.[27]

Table 5.1. Comparison of the proposed crystal structures of titanate nanotubes.[36]

Crystallographic phase	Symmetry	Lattice parameters (nm)				XRD reflections									Ref
		a	*b*	*c*	*β*										
Nanotubes						10.5	24.4	28	34	38.5	44.5	48.2		61.5	
$H_2Ti_3O_7$	Monoclinic	1.602	0.375	0.919	101.5°	11	24.4	29	33	38		48.4	60	62	[27]
$H_2Ti_2O_4(OH)_2$	Orthorhombic	1.926	0.378	0.300	90°	9	24.3	28	34	38	48			62	[33]
$HxTi_{2-x/4}\square_{x/4}O_4 \cdot H_2O$	Orthorhombic	0.378	1.834	0.298	90°	9.5	24.5	28			48			62	[31]

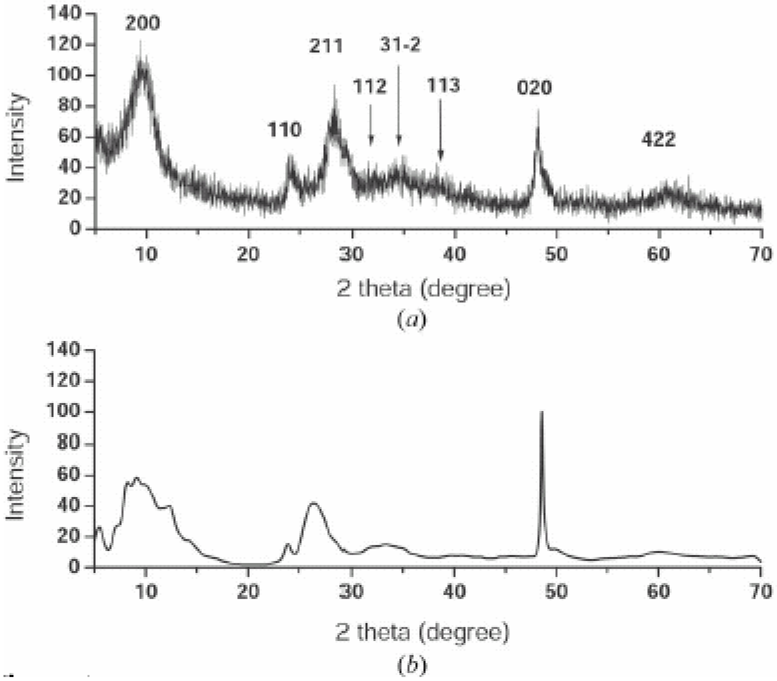

Fig. 5.5 (a) Experimental XRD profile taken from nanotubes and (b) simulated XRD profile using the trititanate nanotube model. (Note: the index number “200”in the figure should be replaced by “001”).[27]

5.3.2 Nanotube $H_2Ti_2O_4(OH)_2$

Jin and co-workers[33] proposed the following crystal structure of titanate nanotubes: $H_2Ti_2O_4(OH)_2$ with an orthorhombic unit cell (a=1.926 nm, b=0.378 nm, c=0.300 nm), based on studies of the sodium content of titanate nanotubes at various pH values during acid washing (in combination with XRD and TEM data). Both protons of the bititanic acid could be ion-exchanged with sodium ions. The XRD pattern had similar reflections to the monoclinic trititanic acid (Table 5.1). The orthorhombic bititanic acid also has a layered structure of walls, where each layer represents a (100) plane rolled around the b-axis. The (100) plane is built up from edge-sharing TiO_6 octahedra, forming a zigzag structure.

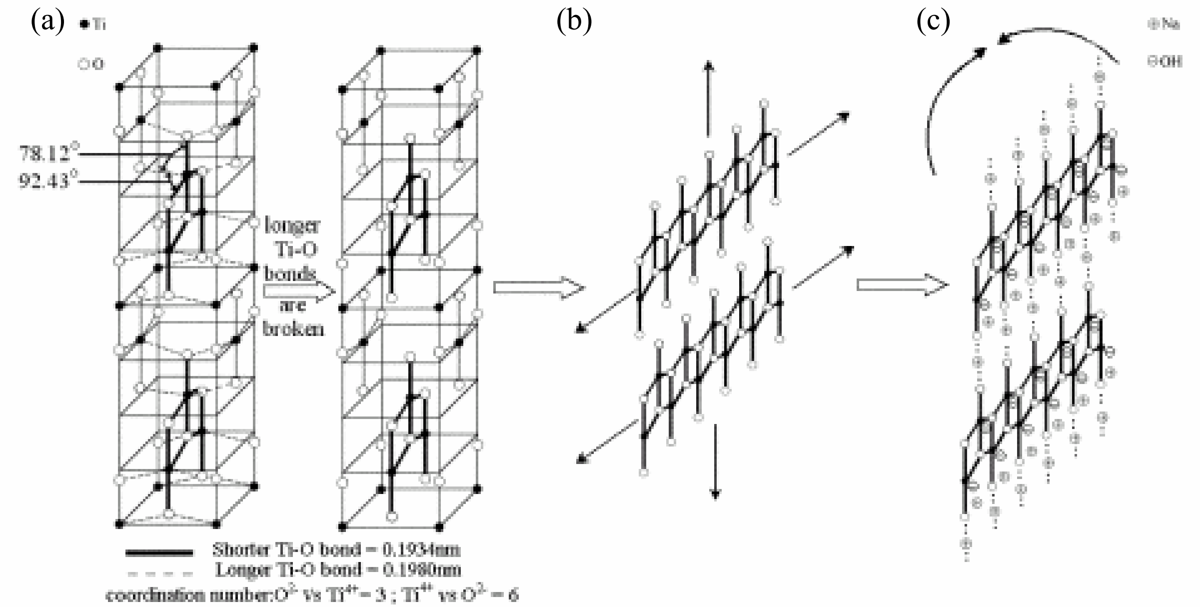

Fig. 5.6 Schematic diagram of formation process for nanotube $Na_2Ti_2O_4(OH)_2$.[33]

It is well known that the structure of anatase TiO_2 can be described in terms of chains of distorted TiO_6 octahedra[37, 38] (Fig. 5.6 (a)). Each Ti^{4+} is surrounded by an octahedron of six O^{2-} ions. Two of the Ti–O bonds are longer (0.1980 nm), while the other four are shorter (0.1934 nm). The coordination number of O^{2-} with Ti^{4+} is three. Upon treatment with concentrated NaOH, the longer Ti–O bonds might be attacked by OH^- ions and break, but the shorter ones would not. Then, linear fragments are formed and peeled from the TiO_2 crystalline particles (Fig. 5.6(b)). The linear fragments link with each other to form planar fragments through O^-–Na^+–O^- ionic bonds (Fig. 5.6(c)). The planar fragments may be denoted the kinetic product in the formation process of the nanotube material. The (–Ti–O–Ti–O–Ti–O–)*x* chains included in a planar fragment are flexible and the thermodynamic product (*i.e.* the solid nanotube $Na_2Ti_2O_4(OH)_2$) could be obtained through the covalent bonding of their end groups (Fig. 5.6(c)). After treating with a HCl solution of pH 1, the nanotube $Na_2Ti_2O_4(OH)_2$ can be converted to the nanotube $H_2Ti_2O_4(OH)_2$.

5.3.3 Nanotubes of Lepidocrocite Titanates

The model of lepidocrocite titanate nanotubes was proposed by Sasaki and coworkers.[34, 35] The model was based on XRD, electron diffraction spectroscopy (EDS) and electron energy loss spectroscopy (EELS) data.

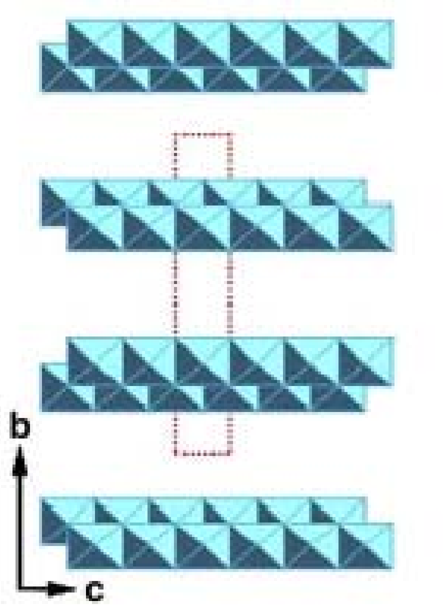

Fig. 5.7 Structure models of lepidocrocite $H_xTi_{2-x/4}\square_{x/4}O_4$. The unit cells were indicated in red lines.[34]

Based on EDS and EELS measurements, it is suggested that the nanotubes and sheets (which become nanotubes after scrolling) are composed of Ti and O. There is almost no Na (detection limit 2 wt %) recorded in the nanotubes. Taking the H into consideration, they should therefore be attributed to protonic titanate, $H_xTi_{2-x/4}\square_{x/4}O_4$ (x ~ 0.7 □: vacancy) (Fig. 5.7). Unlike trititanic acid, which has three steps of corrugated layers, the lepidocrocite titanate consists of a continuous and planar 2D array built up from TiO_6 edge-sharing octahedra.

Many other researchers proposed their own models, such as $H_2Ti_3O_7{\cdot}nH_2O$[29] and

$Na_xH_{2-x}Ti_3O_7$.[39] All the proposed crystal structures described above have the following properties in common. Firstly, this is a well-defined, layered structure with a relatively large interlayer distance 0.7–0.8 nm corresponding to the observation of a characteristic reflection (200) in the XRD patterns at small 2θ values of ca. 10°. Secondly, an atom of hydrogen situated in these interlayer cavities could be exchanged with alkali metal ions. Thirdly, the layers of the (100) plane consist of edge- and corner-sharing TiO_6 octahedra building up to zigzag structures.

Our understanding of the crystal structure of nanotubular titanate is incomplete. Clarification of the structure may lead to a better understanding of the formation mechanism, the integration of metallic, inorganic and organic materials into the nanotubes and the development of materials with novel properties.

5.4 Formation Mechanism of Titanate Nanotubes

Although the detailed sequence of transformation from TiO_2 nanoparticles to titanate nanotubes is still unclear, it is clear that during the transformation of TiO_2 under alkaline conditions, the observed intermediate single layer and multilayered titanate nanosheets play a key role in the formation of tubular morphology.[35, 40] These nanosheets can scroll or fold into the nanotubular morphology. The driving force for curving these nanotubes has been considered by several groups.

Zhang *et al.*[30] considered that single surface layers experience an asymmetrical chemical environment, due to the imbalance of H^+ or Na^+ ion concentration on two different sides of a nanosheet, giving rise to excess surface energy, resulting in bending. The system could be presented as a plane with two springs on each side parallel to this plane (crystallographic *c* and *b*-axis, see Fig. 5.8 (a)). When both sides have a symmetrical chemical environment, both spring constants have similar values. As a result, all tensions are compensated and the plane is straight. When the trititanate nanosheets have a proton-distribution asymmetry, then both sides have different values of free surface energy (spring constants) and, in order to compensate the imbalance in surface tensions, the plane bends towards the surface with a higher spring constant value.

Another reason for bending multilayered nanosheets[40] is that mechanical tensions arise during the process of dissolution/crystallization in nanosheets. During spontaneous crystallization and rapid growth of layers, it is possible that the widths of different layers vary. It is likely that the imbalance in the layer width creates a tendency for the layers to move within the multiwalled nanosheet in order to decrease the excess surface energy (see Fig. 5.8 (b)). This can result in the bending of multilayered nanosheets. It was demonstrated that, during simultaneous shift of the layer and bending of the nanosheet, the gain in surface energy is sufficient to compensate for mechanical tensions arising in the material during curving and wrapping into nanotubes. The kinetic rate of curving the nanotubes might control the diameter of the nanotubes produced, which can be adjusted by varying the condition of synthesis.

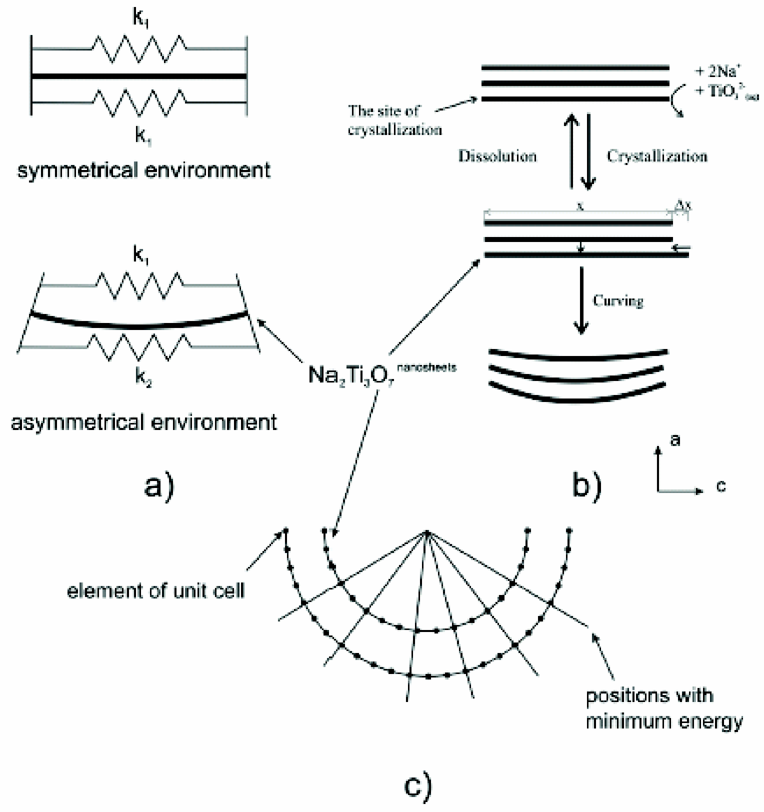

Fig. 5.8 The driving forces for bending titanates nanosheets under alkaline hydrothermal conditions. (a) Asymmetrical chemical environment resulting in difference in surface tensions [30, 41]; *k*1 and *k*2 are spring constants on each side of the nanosheet. (b) Imbalance in layer widths resulting in shifting of the layer and bending of nanosheets.[40]

In the absence of factors which stabilize the bended form of nanosheets, the reverse process of transformation of bended nanosheets back to the planar form should occur. While it is difficult to find stabilization factors for a curved single-layer nanosheet (unless an asymmetrical environment is maintained); the curved form of multilayered nanosheets could be stabilized by periodic potentials in the crystal lattice. This effect can be illustrated using the example of two nanosheets curved into a semicircle (Fig. 5.8(c)). Taking the internal diameter of nanotubes as 3.5 nm, the distance between layers in the wall as 0.72 nm, and the distance between Ti atoms along the *c*-axis as 0.919/3 nm, the number of Ti atoms in the first layer will be 18 and the number of Ti atoms in the second layer will be 25. In this case, 8 out of 18 atoms in the first layer will be situated in the same radial lines with eight atoms from the second layer. These lines are shown in Figure 5.8(c) for clarity. The lateral distance between these eight pairs of atoms is minimal and all their positions are very close to the positions in the crystal. Any small straightening of the nanosheets will increase the energy of the system since these eight pairs start to increase the distance between atoms. This means that curving of multilayered nanosheets to nanotubes passes through a sequence of metastable states that are stabilized by a periodic potential in the nanosheet lattice.

Overall, the process of transformation of raw TiO_2 to nanotubular titanate can be considered to take place in several stages: i) partial dissolution of raw TiO_2 accompanied by the growth of layered nanosheets of sodium tritinatates, ii) exfoliation of nanosheets, iii) crystallization of dissolved titanates on nanosheets resulting in mechanical tensions, which induce the curving and wrapping nanosheets to nanotubes, iv) growth of nanotubes along the length, and v) exchange of sodium ions with protons.

5.5 Properties of Titanate Nanotubes

5.5.1 Ion-Exchange Property

According to the crystal structure of titanate nanotubes, protons occupy the cavities between the layers of TiO_6 octahedra. These protons in titanate nanotubes have very broad multiple-peak signals in the ^1H MAS NMR spectrum[42] due to solid-state inhomogeneous broadening. The open morphology of the nanotubes results in effective ion-exchange properties.[43] HRTEM studies of cesium-saturated titanate nanotubes have revealed that the alkaline ions in the titanate framework[44] are positioned inside the walls of the nanotubes between the layers. The intercalation of alkaline ions (Li^+, Na^+, K^+, Rb^+, Cs^+)[44] and some transition-metal ions (Co^{2+}, Ni^{2+}, Cu^{2+}, Zn^{2+}, Cd^{2+})[43] between the layers in the multilayered nanotubes does not affect the interlayer distance, indicating that the rigidity of the titanate framework is maintained during ion exchange.

The maximum reported ion-exchange capacity for sodium ions, defined as the ratio between sodium and titanium atoms in the nanotubes (Na/Ti ratio), varies from 0.67[45] to 1.1.[33] The first number was obtained from analysis of titration curves for suspended titanate nanotubes in aqueous solution by 0.05 M NaOH. The other number was evaluated by chemical analysis of the amount of sodium in the sample of fresh titanate nanotubes taken directly from a 10 M NaOH solution and washed with ethanol. If it is assumed that the crystal structure of titanates corresponds to the structure of trititanate[21] then the value 0.67 corresponds to the complete ion exchange of titanate protons with the sodium ions. The fact that all protons in titanate nanotubes are exchangeable to alkali ions in solution means that the ion transport in the interlayer space along the length of the nanotubes is very effective. This is also confirmed by the fast establishment of equilibrium between ions in the nanotubes and ions in solution. The degree of ion exchange of precious metals to the protons of titanate nanotubes is less then that for alkali metals.

The ion exchangeability also provided the opportunity to prepare a complex of guest molecules and titanate nanotubes, which would be ideal materials for heterogeneous catalysis or catalyst support. The nanotubular structure yielded high specific surface areas and should be advantageous for the ion-exchange process. Optical and other new properties could be introduced or manipulated by introducing different kinds of cations.

5.5.2 Surface Chemistry

Titanate nanotubes combine the properties of conventional TiO_2 nanoparticles, such as being wide-bandgap semiconductors and stimulating photocatalysis. Most of proposed crystal structures of titanate nanotubes hypothesize that the layer of a titanate nanotube consists of edge- and corner-sharing TiO_6 octahedra building up to a zigzag structure. Moreover, Rajh *et al*[19] reported that the coordination geometry of Ti atoms in titanate nanotubes differs from that in the bulk rutile and anatase structures, and is surprisingly similar to that of 2-nm-diameter nanoparticles based on XANES spectra. Since the exact crystal structure of titanate nanotubes is still disputed, we will analyze the surface structure and reaction based on those of TiO_2 nanoparticles.

In following sections, we will focus our discussion on the properties of the undercoordinated Ti sites presented on the surface of small TiO_2 nanoparticles. Those undercoordinated Ti sites are very reactive for certain molecules such as catechol. Catechol molecules could attach to Ti sites by forming bidentate (both of the hydroxyl groups attaching to one/two Ti atom(s)), or monodentate structure (one of the hydroxyl groups attaching to one Ti atom). Different binding configurations of catechol on nanoparticle surfaces (e.g. monodentate and bidentate structures) lead to the different absorption energies, and may induce different structural changes of TiO_2 nanoparticles. Similar to TiO_2 nanoparticles, our experimental results (see Chapter 6 for details) show that when titanate nanotubes are exposed to the organic molecules, e.g. catechol, their local structures change. In order to study the mechanisms of different binding configurations between titanate nanotubes and the organic molecules, we chose three different molecules, hydroquinone, 4-Methoxypenol(MEHQ) and catechol. Each of these three molecules is expected to form different binding configuration. The optical and structural properties of titanate nanotubes and the three hybrid structures (titanate nanotube/hydroquinone, titanate nanotube/MEHQ and titanate nanotube/catechol) were characterized by multiple techniques. In order to pave the way for later discussion on the surface reaction mechanisms of the organic molecule/titanate nanotube hybrid structures, it is necessary to go through the discussion on the surface reactions between catechol and TiO_2 nanoparticle with different binding configurations.

The following section is started with a review of the undercoordinated Ti sites on the TiO_2 nanoparticle surface, followed by an introduction to the surface reaction between some molecules, e.g. catechol, and TiO_2 nanoparticles. The reaction between water and TiO_2 nanoparticles is briefly mentioned, since water was used during the synthesis and the stability study in aqueous condition. The reaction between catechol and TiO_2 nanoparticles is discussed in particular details, including the reaction energy calculations of different binding configurations, and the induced optical and structural changes, etc. The recent studies on the structural properties of titanante nanotubes are also summarized.

5.5.2.1 Surface Properties of TiO_2 Anatase Nanoparticle

The structural and electrochemical properties of nanoparticles were found to be different from those of the corresponding bulk semiconductors. There have been studies of molecular interactions on the anatase surface of TiO_2.[46-52] The anatase (101) surface was calculated to be one of the lowest energy surfaces of anatase. It was found that on the (101) surface molecular adsorption with two hydrogen bonds to neighboring bridging oxygens is preferred over dissociative adsorption at both low and monolayer coverage. In contrast, the dissociative adsorption is more favorable than molecular adsorption on the anatase (001) surface. The recent studies of Rajh *et al.*[[17, 53] on TiO_2 nanoparticles of ~20 Å size suggest that defect sites present on the surfaces of very small TiO_2 nanoparticles may be very reactive to certain molecules such as catechol and ascorbic acid. It was observed that there was a large optical red shift of about 1.6 eV when catechol and ascorbic acid are adsorbed on TiO_2 nanoparticles.

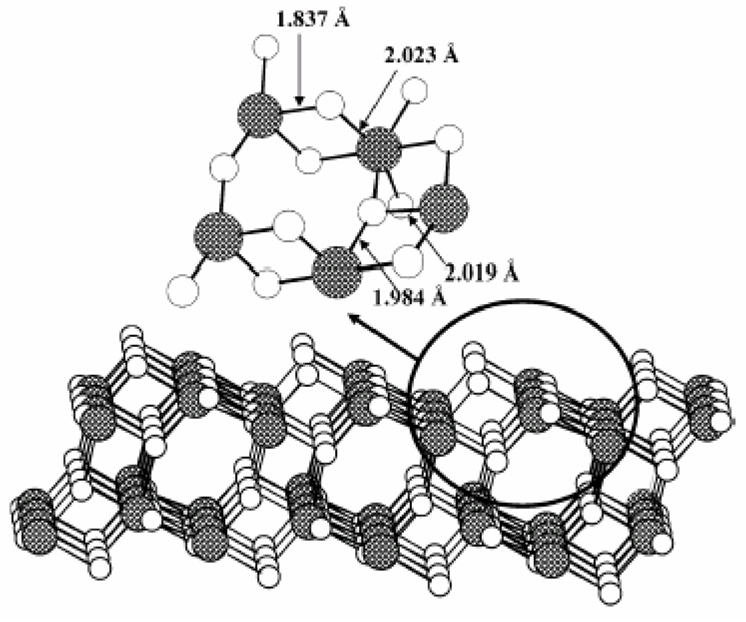

Fig. 5.9. Anatase (101) surface (side and top views)[53]

Rajh *et al.*[53]also examined several aspects of water and catechol binding on the anatase (101) surface and on the undercoordinated defect sites. The cluster models for adsorption sites were obtained from a relaxed anatase (101) surface[47] structure shown in Fig. 5.9 and were kept unchanged throughout the calculations, except where noted. Hydrogen saturators were used on oxygens with dangling bonds so that the clusters were closed shell with neutral charge. Two different types of adsorption sites were examined for water and catechol. The first corresponds to a titanium atom coordinated to five oxygens at the (101) surface. Clusters modeling this site including 1 (**S1**), 2 (**S2**), 4 (**S4**), and 6 (**S6**) titanium atoms are shown in Fig. 5.10. Also shown in Fig. 5.10 is a 17-atom cluster (**S17**) that was used to embed the smaller clusters in a larger cluster for single-point calculations of excitation energies. The second site corresponds to a defect site that contains a titanium atom coordinated to five oxygen atoms, one of these corresponding to a Ti=O double bond. Clusters modeling this site including 1 (**D1**), 2 (**D2**), 3 (**D3**), and 4 (**D4** and **D4′**) titanium atoms are shown in Fig. 5.11. They considered two possible four-titanium-atom clusters with Ti=O bonds, **D4** and **D4′**.

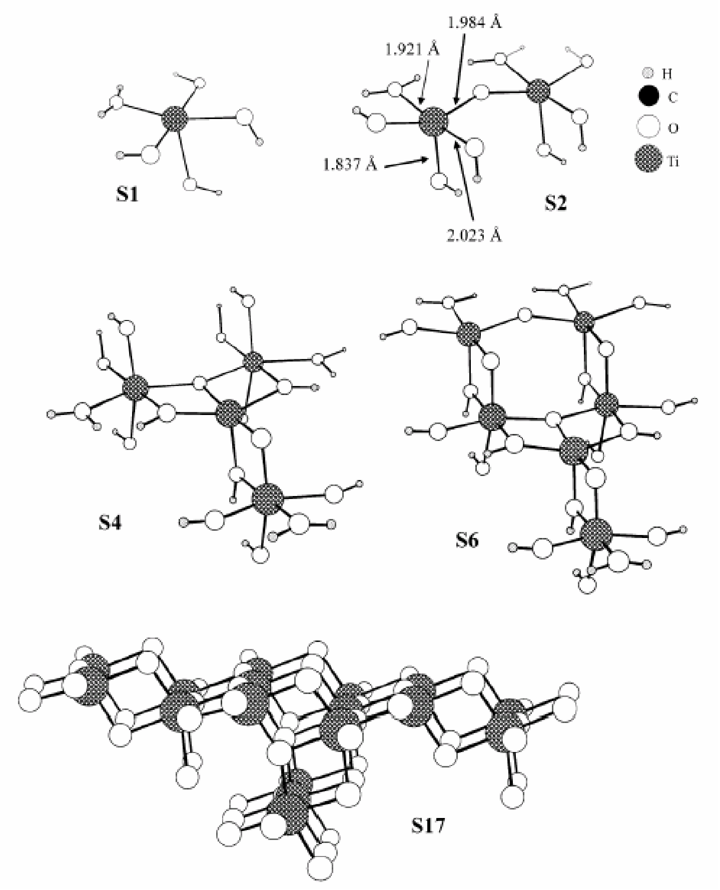

Fig. 5.10 Cluster models used for the anatase (101) surface. The geometrical parameters of the cluster models were obtained from a relaxed anatase (101) surface (see text) and kept unchanged throughout the calculations, except where noted.[53]

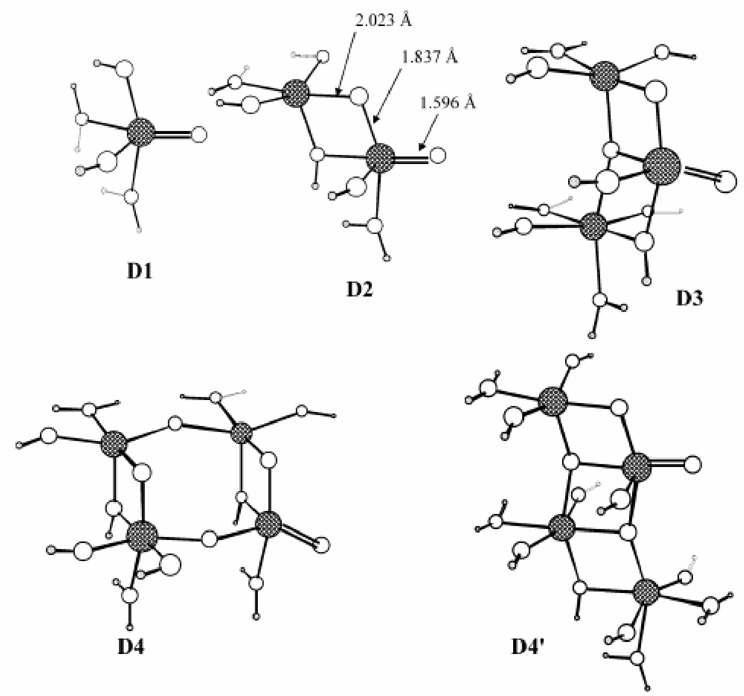

Fig. 5.11 Cluster models used for defect Ti=O double bond site. Atom definitions are same as in Figure 5.10.[53]

5.5.2.1.1 Water Adsorption

Molecular adsorption structures for H_2O on the **S2**, **S4**, and **S6** clusters (**W3**, **W5**, **W7**, **W8**) are shown in Fig. 5.12. This figure also contains the dissociative H_2O structures on the **S2**, **S4**, and **S6** clusters (**W4**, **W6**, **W9**, and **W10**). Dissociative H_2O structures on the **D4** and **D6** clusters (**W13**, **W14**) are shown in Fig. 5.13.

The calculation indicates that molecular adsorption on the (101) surface is more favorable than dissociative adsorption. The molecular adsorption energy at the five-coordinated titanium (101) sites on the **S2** cluster is -21.6 kcal/mol compared to a dissociative energy of only -8.4 kcal/mol.

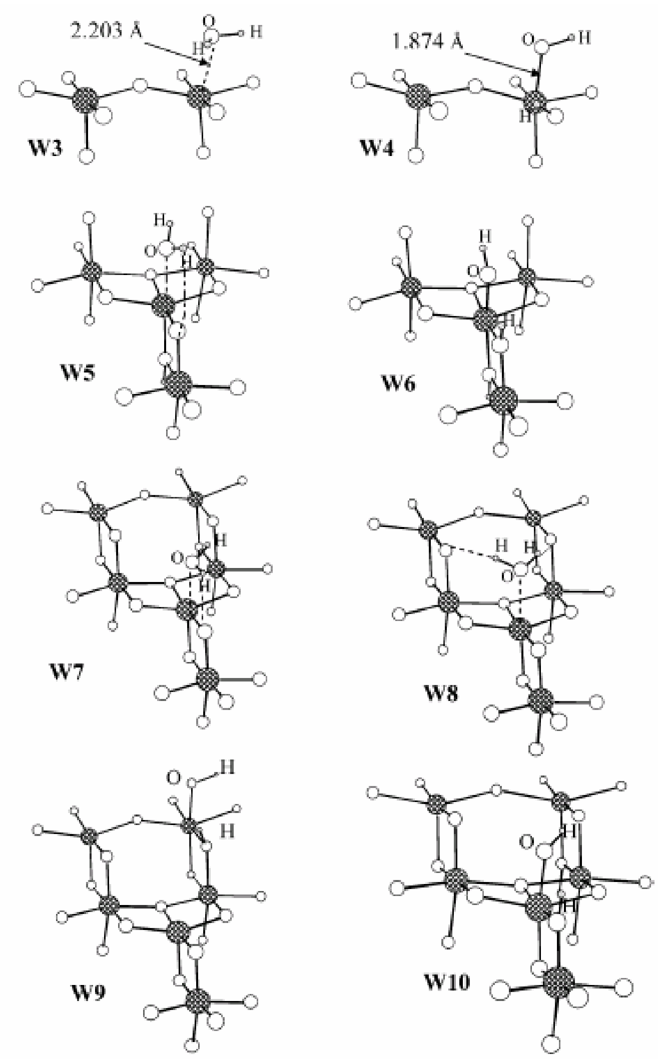

Fig. 5.12 Molecular adsorption and dissociative adsorption of H_2O on cluster models of anatase (101) surface. Terminal hydrogens not shown. Atom definitions are same as in Figure 5.10.[[53]

The dissociative addition of water at the edge site involves the breaking of one OH bond in water that adds a hydrogen to the oxygen in Ti=O and an OH to the titanium of this site, as shown in structures **W13** and **W14** in Fig. 5.13. The dissociative energy for the addition of water at the Ti=O site of the **D2** cluster is -18.2 kcal/mol. Thus, the edge site is significantly more reactive toward the dissociative addition of water than the (101) surface, which has a reaction energy of -8.4 kcal/ mol, but is still slightly less stable than the molecular adsorption of water on the (101) surface.

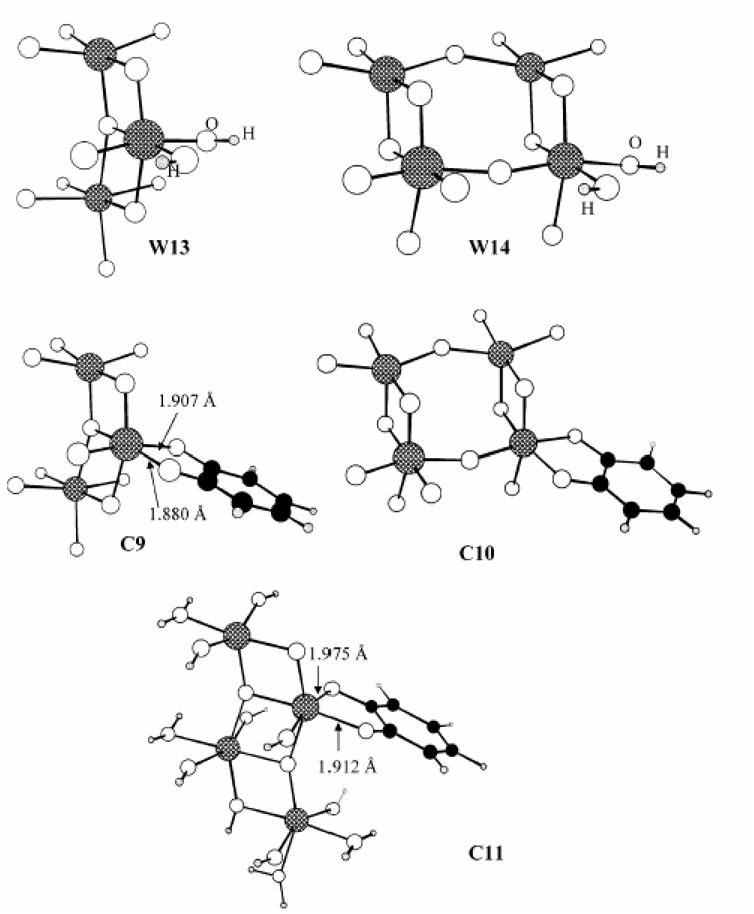

Fig. 5.13 Dissociative addition of water and dissociative bidentate adsorption of catechol at a defect Ti=O double bond site.Terminal hydrogens not shown. Atom definitions are same as in Fig. 5.10.[53]

5.5.2.1.2 Catechol Adsorption

Molecules having OH groups such as catechol may adsorb on the surface of a TiO_2 nanoparticle by molecular adsorption or by dissociative adsorption. In the former process, a van der Waals complex with hydrogen bonds is formed. Molecular adsorption structures for catechol on the **S2** and **S4** clusters (**C3**, **C5**) are shown in Fig. 5.15. In dissociative adsorption on the (101) surface, a hydrogen atom dissociates from one of the catechol OH groups and attaches to a bridging oxygen on the surface, and the remaining catechol oxygen bonds to a five-coordinate surface titanium atom forming a monodentate structure. Fig. 5.15 also contains the dissociative catechol structure on the **S2** and **S4** clusters (**C4**, **C6)** Another possible adsorbate structure for catechol on the (101) surface involves bridging structure. On the (101) surface, the dissociation of two hydrogens from the catechol can lead to the formation of a bidentate bridging structure with two surface titanium atoms (**C12 in** Fig. 5.14). At a defect Ti=O site, there can be H_2O elimination resulting in a bidentate structure with two chemical bonds from catechol to a surface titanium. Dissociative catechol structures on the **D3**, **D4** and **D4′** clusters (**C9**, **C10**, **C11**) with a defect site having a Ti=O are shown in Fig. 5.13. These are all bidentate structures.

The reaction energies of the molecular adsorption of catechol on the (101) surface and dissociative adsorption of monodentate structure are approximately the same (ca. -19 kcal/mol). The dissociative bidentate bridging structure has a dissociative reaction energy of -17.4 kcal/mol, similar to that of the monodentate and molecular structures on the (101) surface. The dissociative energy for the addition of catechol at the Ti=O site in a bidentate structure is -24.8 kcal/mol and -30.1 kcal/mol for the **D2** and **D4′** clusters, respectively. Thus, the edge site is significantly more reactive toward catechol than either the molecular adsorption or dissociative addition on the (101) surface. This is probably due to the formation of the two chemical bonds to one titanium at a defect site.

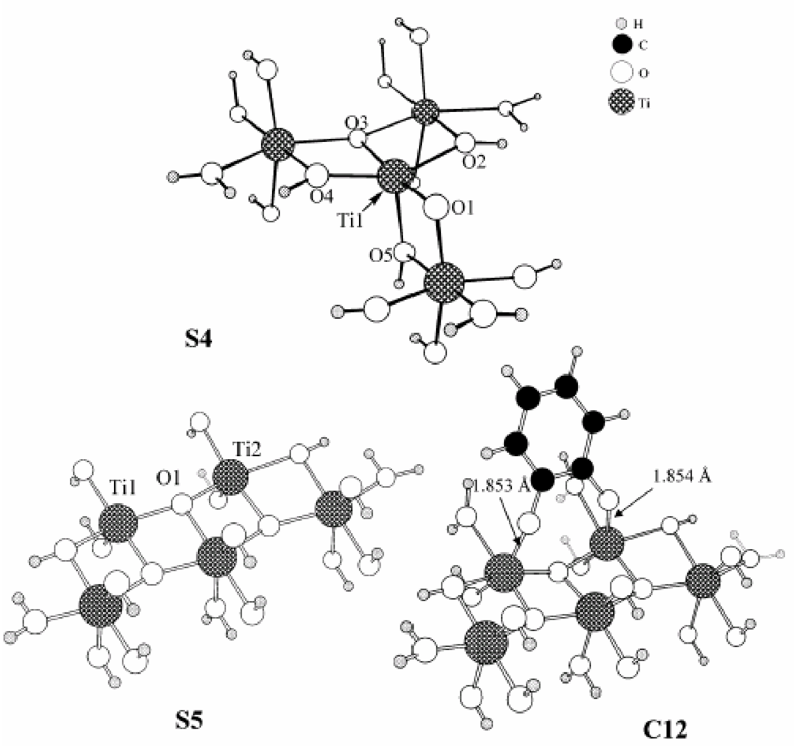

Fig. 5.14 Cluster model used for investigating the effect of (101) surface relaxation at interaction site for a 4 Ti cluster and a 5 Ti atom cluster. Also shown is the bridging structure for catechol when it is dissociatively adsorbed on two titanium atoms The numbered atoms are relaxed.[53]

Water and catechol may compete for a defect site. Water can react with a Ti=O double bond to form $Ti(OH)_2$ (**W13** and **W14**), and catechol can react with Ti=O to form a bidentate structure (**C9-C11**). The results indicate that catechol forms a more stable structure than water with the edge site. It is important to avoid water when we synthesize the hybrid structure of titanate nanotubes and organic molecules, like catechol (see Chapter 6 for details).

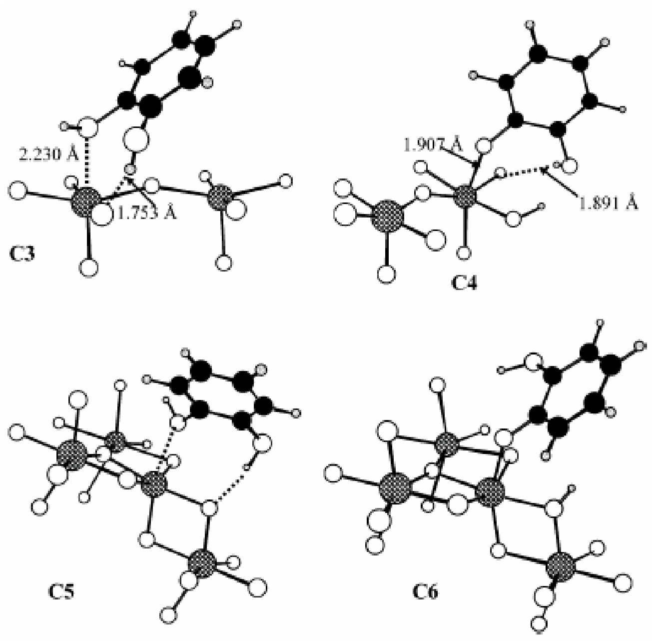

Fig. 5.15 Monodentate dissociative and molecular adsorption of catechol on cluster models of anatase (101) surface.Terminal hydrogens not shown. Atom definitions are same as in Figure 5.10.[53]

5.5.2.1.3 Optical Spectra of TiO_2-Catechol Complexes

Experimental results indicate that a shift to longer wavelength in the optical absorption spectra occurs when molecules such as catechol (Fig. 5.16) [15, 18, 19, 48, 54], ascorbic acid[17] or mPEG-DOPA[16] bind to small TiO_2 nanoparticles.

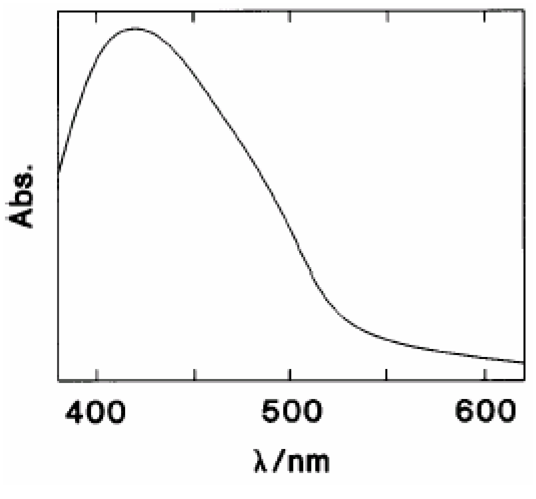

Fig. 5.16. Differential diffuse reflectance spectrum of surface titanium–catechol complexes; the spectrum is plotted in arbitrary absorbance units.[18]

Rajh *et al.* studied the energy levels of the adsorbate-TiO_2 clusters and the results are illustrated schematically in Fig. 5.17 for both the molecular complex and the bidentate adsorbate. The adsorption of catechol at the defect site leads to a larger red shift in the TiO_2 excitation energy than molecular adsorption on the (101) anatase surface does. This is consistent with recent observations of a large red shift for the adsorption of catechol and ascorbic acid on small (20 Å) TiO_2 nanoparticles, and is probably due to the formation of two Ti-O bonds at the defect site. The excitation occurs from a molecular orbital primarily associated with catechol carbon atoms, to a molecular orbital delocalized on some of the titanium atoms and corresponds to charge transfer from the catechol to the TiO_2 cluster. There is a larger red shift of the absorption edge for the bidentate or monodentate binding compared to that for the molecular complex because of the stronger interaction between catechol and titanium oxide energy levels for the former type of interaction. Evidence for the stronger interaction comes from an examination of the molecular orbital, which shows a stronger mixing of catechol and TiO_2 orbitals in the HOMO of the bidentate and monodentate structures compared to that in the molecular complex. Also, the bidentate and monodentate structures have $Ti\text{-}O_{catechol}$ distances of 1.9-2.0 Å, which are shorter than in the molecular complex (2.2-2.3 Å) and are closer to the bulk Ti-O distances. Therefore, the HOMO-LUMO gap is smaller for the shorter bonds than for the van der Waals bonds, causing a larger red shift.

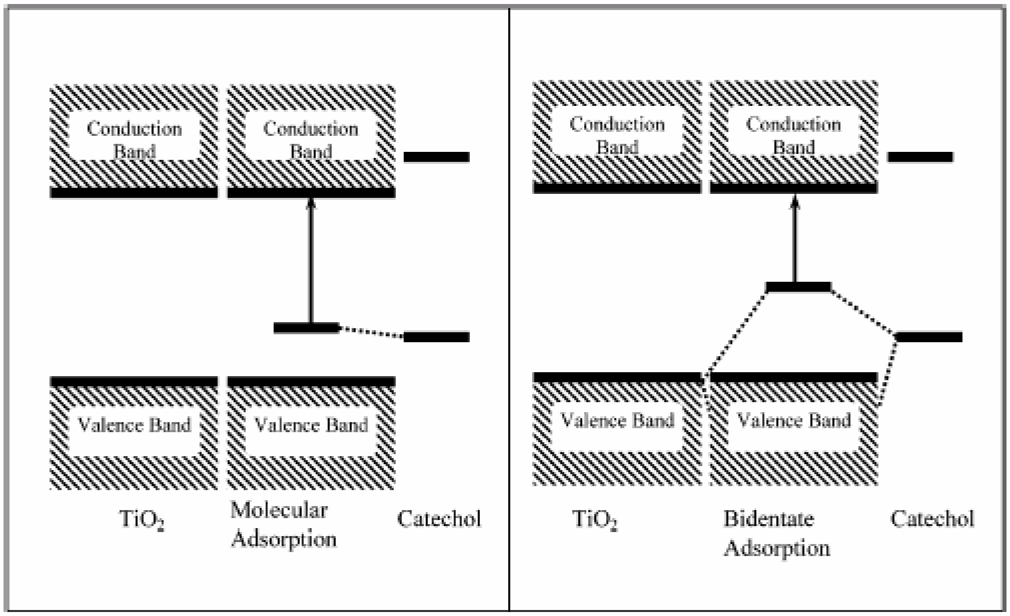

Fig. 5.17. Schematic illustration of electronic structure of catechol adsorbed on TiO_2 nanoparticles molecularly and dissociatively (bidentate).[53]

5.5.2.1.4 Surface Reconstruction of Nanocrystalline TiO_2 by Surface Modification

To probe the origin of the unique functions of titanium dioxide (TiO_2) nanoparticles observed in photocatalytic reactions and surface reactions, structures of Ti atom sites in titanium dioxide (TiO_2) nanoparticles with different sizes were studied by Rajh *et al.*[55] Compared to the bulk TiO_2 structure, the results revealed an increasing disorder of the lattice with decreasing sizes of the nanoparticles based on a coordination number decrease. These results imply that the increasing number of 5-coordinated Ti surface sites as well as possible corner defects in small nanoparticles may be the main cause of the unique surface chemistry exhibited by nanoparticles of TiO_2.

In their later work[17] they reported that the coordination of Ti surface atoms changes from six-coordinate (octahedral) in 500 Å particles to pentacoordinate (square-pyramidal) in small 20 ± 3.2 Å particle colloids. They confirmed the existence of the shorter Ti-O bond lengths in 20 Å particles (1.79 Å) as compared to bulk anatase TiO_2 (1.96 Å) (Fig. 5.18).

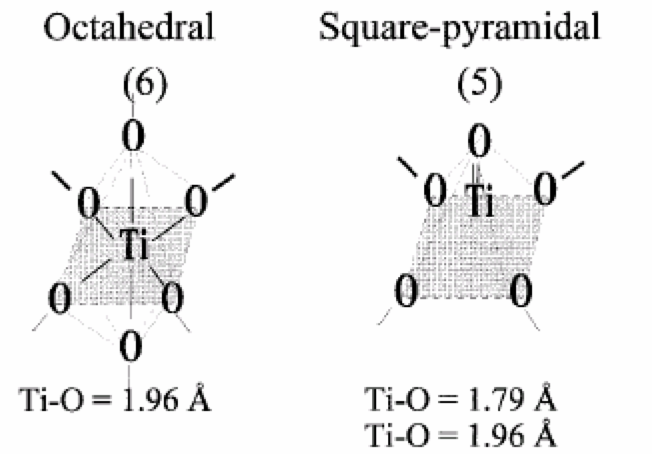

Fig. 5.18 Schematic presentation of the coordination environment in flat surface and small-particle (*D* = 20 Å) colloids.[17]

In contrast to large particles and flat surfaces, they have found using FTIR spectroscopy that under-coordinated "corner defects" in small-particle colloids bind ascorbic acid as bidentate ligands through both of the ortho-substituted hydroxyl groups of the furane ring. This is consistent with bidentate binding that results in the formation of a five-membered ring around the surface Ti atoms (Fig. 5.19) having a favorable conformation of bond angles and distances for octahedrally-coordinated surface Ti atoms. Extended X-ray absorption fine structure (XANES) reveals that surface modification with ascorbic acid restores the features of octahedrally coordinated Ti in the anatase crystal environment. This indicates that bidentate binding of ascorbic acid helps to reestablish the octahedral coordination of the nanocrystalline surface, relaxing the surface Ti atoms to their original anatase environment. They also mentioned that monodentate binding on large surfaces does not induce a change in the optical properties.

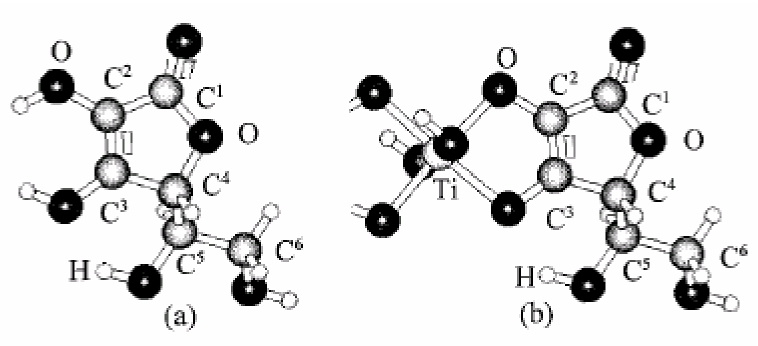

Fig. 5.19 Molecular Structure of Ascorbic Acid before (a) and after (b) Binding to the Surface of Nanocrystalline TiO_2.[17]

Molecules with similar structure were studied by Rajh, *et al*[15], such as catechol, alizarin, dopamine (Fig. 5.20), etc. These molecules can form complex ligands on the surface of a TiO_2 nanoparticle, inducing a red shift of the semiconductor absorption compared to the unmodified nanocrystallites. Other groups also reported the red shift induced by the attachment of charge-transfer ligands, like mPEG-DOPA,[16] vitamin C,[17] catechol,[18] salicylic acid,[48] etc. It was found that these five-coordinated defect sites are the source of novel enhanced and selective reactivity of the nanoparticle toward bidentate ligands binding as observed using IR spectroscopy. Those ligands have the optimal geometry for chelating surface Ti atoms, resulting in a reconstruction of the six-coordinated octahedral geometry of surface Ti atoms, evidenced by both XANES and EXAFS.

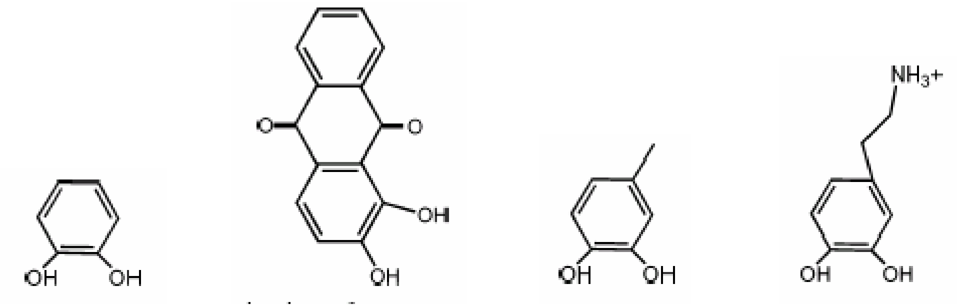

catechol alizarin methyl catechol dopamine

Fig. 5.20 Molecular Structure of catechol, alizarin, methyl catechol and dopamine. [15]

5.5.2.2 Surface Properties of Titanate Nanotubes

Since the first report on the synthesis of titanate nanotubes,[56] many efforts have been made to characterize the particles. Most studies have focused on the crystal structure and the possible mechanism of nanotube formation. In order to determine possible applications of nanotubes, systematic studies of other characteristics are necessary. Systematic studies of physicochemical properties have only recently been reported.[19, 40, 43]

5.5.2.2.1 Structure Characterized by Raman Spectroscopy

Raman spectroscopy is used to characterize the structural property of titanate nanotubes. A typical Raman spectrum[28] of titanate nanotubes is shown in Fig. 5.21, which agrees well with those reported earlier[43, 57-59]. The spectrum is characteristically different from the Raman signature of both anatase and rutile, which have peaks at 142, 194, 394, 512, 635 and 236, 444, 607 cm^{-1}, respectively.

According to Hodos *et al.*[59] the sodium form of ion-exchangeable trititanate nanotubes exhibits features at 278, 448, 660 and 905 cm^{-1}. The 448 cm^{-1} peak was assigned to a pure framework Ti–O–Ti vibration, the 278 and 660 cm^{-1} peaks to Ti–O–Na vibrations involving the Na^+ ion occupying an ion-exchange position in the trititanate wall[26] and the 905 cm^{-1} peak to four-coordinate Ti–O involving non-bridging oxygen atoms coordinated by the Na^+ ion.[43]

Kasuga *et al.*[26] suggested that the peaks at 278 cm^{-1} and 660-760 cm^{-1} were due to Na-O-Ti, as reported for Na_2O-TiO_2 glass.[60] The peak at 905 cm^{-1} is due to four-coordinate Ti-O.

Kim *et al.*[61] investigated the formation of the sodium titanate hydrogel layer on the surface of Ti metal treated in NaOH. It was proposed that the peak about 448 cm^{-1} be assigned to a Ti–O bending vibration involving three-fold oxygen; the peaks at about 690 cm^{-1} to a Ti–O bending and stretching vibration involving two-fold oxygen; the peak at about 905 cm^{-1} to a Ti–O stretching vibration involving non-bridging oxygen, some of which are coordinated with Na$^+$ ions [62, 63].

A different assignment was suggested by Qian *et al.*[58] They proposed that the peaks at 278 and 905 cm^{-1} are from the symmetric stretching mode of a short Ti-O bond of sodium titanate in the layer structure.[64]

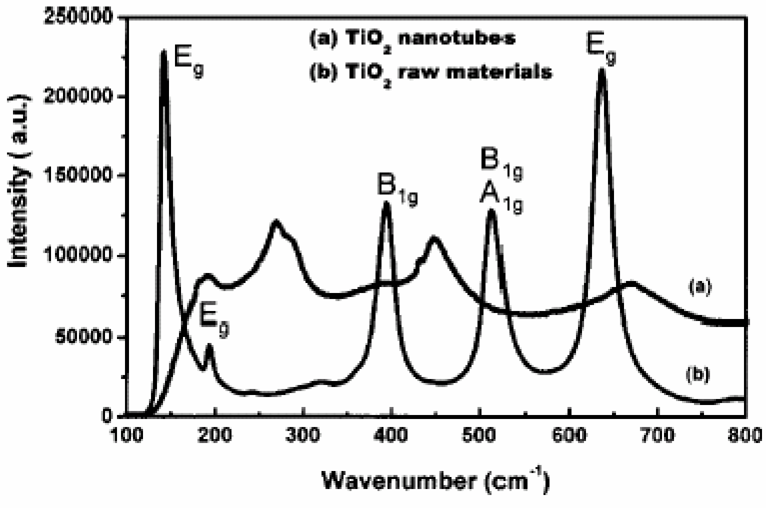

Fig. 5.21 Raman spectra of the (a) as-synthesized titanate nanotubes and (b) TiO_2 anatase.[28]

Unfortunately, the assignment of Raman peaks is still under dispute and the exact assignment is not available.

5.5.2.2.2 Structure Reconstruction of Titanate Nanotubes Through Surface Chemistry

Recently, based on XANES spectra, Rajh *et al*[19] reported that the coordination geometry of the Ti atoms in titanate nanotubes differs from that in bulk rutile and anatase structures, and is surprisingly similar to that of 2-nm diameter nanoparticles. These results suggest that

40 % of Ti atoms in nanotubes are undercoordinated. As in the TiO_2 nanoparticles, the five coordinated defect sites in nanotubes react selectively with bidentate ligands[15]. The incompletely-coordinated Ti defect sites exhibit a high affinity for oxygen-containing ligands and present the opportunity for chemical modification. Oxygen-rich charge transfer ligands, e.g. dopamine, form strongly-coupled conjugated structures by restoring the coordination of the Ti defect sites. As a consequence, the attachment of the ligands to Ti sites results in the red shift of the optical absorption compared to that of unmodified nanotubes, as shown in Fig 5.22.

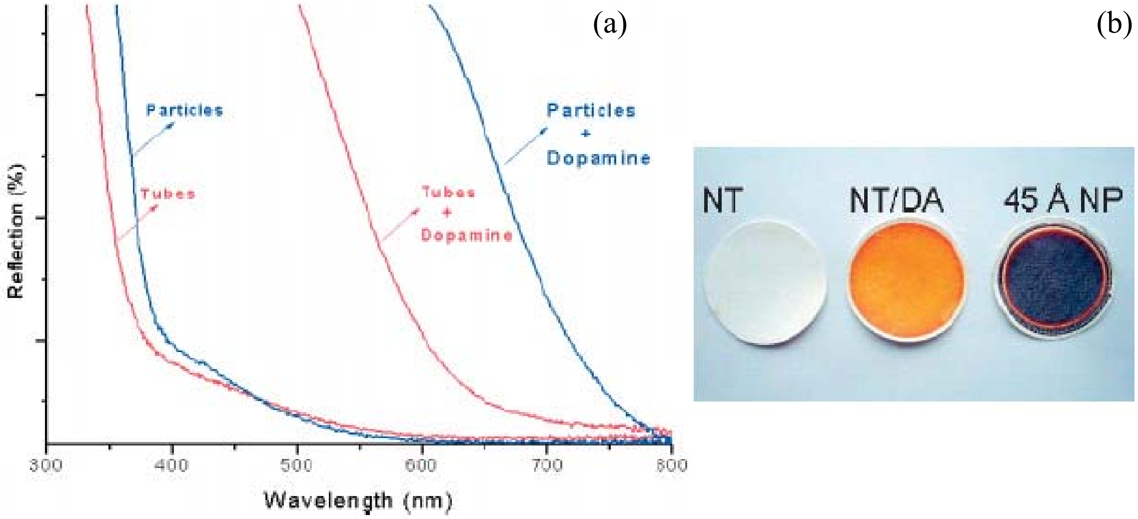

Fig. 5.22. (a) Reflection spectra of bare and surface modified 45 Å TiO_2 nanoparticles and titanate nanotubes. (b) Photographic image of powdered samples of nanotubes before (NT) and after (NT/DA) surface modification with dopamine, compared to dopamine-modified 45 Å TiO_2 nanoparticles (45 Å NP).[19]

In contrast to the nanoparticles, in which all the surface Ti atoms were modified by dopamine, the addition of charge transfer ligands restored only a small fraction (~5 %) of the undercoordinated sites. This result suggests that the majority of undercoordinated sites were located on the interior walls of the nanotubes; most were probably on the interface between the layers and were not accessible to dopamine molecules.

In our study, we are able to restore the undercoordinated Ti sites completely, including those on the interface between the layers. This development contributes significantly to the synthesis of the uniform novel molecule-nanotube hybrid system: control of titanate nanotube properties by changing the surface environment.

5.6 Applications of Titanate Nanotubes

The unique properties of titanate nanotubes, together with their unusual morphology, render these materials very promising for many applications. Since my study mainly focuses on the structural and the surface properties, I will just briefly mention two important applications.

5.6.1 Catalysis and Photocatalysis

Titanate nanotubes are of great interest for catalytic processes since their high cation-exchange capacity provides the possibility of achieving a high loading of active catalyst with an even distribution and a high dispersion. The open mesoporous morphology of nanotubes and the high specific surface area facilitate transport of reagents to the active sites during the catalytic reaction. The semiconducting properties of titanate nanotubes result in a strong electronic interaction between the support and a catalyst, improving catalytic performance in redox reactions. There are a few reports of catalytic activity of titanate nanotubes as acid-based catalysts[65] and in the hydrolysis of 2-chlorethyl ethylsulfide.[20] Most of the catalytic studies are focused on the use of this mesoporous semiconductor as a high-surface-area catalyst support. There are several examples of titanate nanotubes as mesoporous catalyst supports for different nanoparticles: CdS-decorated TiO_2 nanotubes[59, 66] and Zn^{2+} doped nanotubes[67] in the photocatalytic oxidation of dyes, RuO_2–TiO_2 nanotubes as an electrocatalyst for reduction of CO_2[68], and ruthenium(III)-hydrated oxide deposited on TiO_2 nanotubes for selective oxidation of alcohols.[42]

The ability of titanate nanotubes to adsorb metal cations from aqueous solution provides a strategy for the deposition of active catalysts on the surface of nanotubes. During adsorption, the catalyst precursor should be in cationic form in aqueous solution. This will allow the achievement of a high value of ion-exchange ratio and the washing out of the impregnating solution in order to avoid further formation of catalyst outside the surface of the titanate nanotubes. The combination of ion exchange followed by reactive fixation of catalyst allows a relatively high catalyst loading which maintains specific catalytic activity[42] The good electrical contact between nanoparticles and titanate nanotubes can provide an efficient interfacial charge-transfer region, which makes this binary system also suitable for photocatalysis.

5.6.2 Solar Cells

Nanotubular titanate films were also examined as an electrode of dye-sensitized solar cells[69-71] and had the following characteristics: open-current voltage of 0.704 V, short current of 1.26 mA, energy conversion efficiency of 2.9% (7.1% in the literature[70]). These characteristics are very similar to those of conventional titania nanoparticles (P-25) used for solar-cell technology and the authors considered this result as negative. At that time, however, the following parameters had been chosen, which minimize the benefit of titanate nanotubes. Firstly, the negatively charged standard *cis*-di(thiocyanate)bis(2,2-bipyridyl- 4,4-di-carboxylate) ruthenium(II) complex was used as the dye sensitizer deposited on the surface of titanate nanotubes from ethanol solution. In this condition, the adsorption of dye molecules is not optimal. The best results are expected using adsorption of positively charged molecules of dye from aqueous solution. Secondly, the annealing of the acid form of a titanate nanotube film at 450°C could result in loss of nanotubular morphology and formation of nanorods, with have less surface area and ion-exchange capacity. Thirdly, as the authors indicated, the agglomeration of nanotubes into secondary particles needs to be avoided during the preparation of nanotubes. It should now be possible to strategically improve the performance of solar cells based on TiO_2 nanostructures by tailoring synthesis conditions to produce optimum materials.

So far, the understanding of the structure, formation mechanism and chemical properties is still limited. Although the mechanism of transformation and details of the synthesis have been thoroughly studied, there are several unanswered questions. Will an improved knowledge of the mechanism allow us to modify and control the properties (optical, structural) of nanotubes and tailor them for specific needs? Will the material, titanate nanotube, be modified with uniform properties, including the Ti sites on the interfaces between the layers? Will these modified properties be stable in specific conditions for the applications? For example, the TiO_2 films, as the electrode, in a solar cell must be stable in the electrolyte, usually an aqueous solution.

Our experimental results shown in Chapter 6 provide important information on the properties of titanate nanotubes and titanate nanotube/organic molecule hybrids. Based on those results, we achieved a better understanding of the structure of the titanate nanotubes, and the mechanisms of the reactions between titanate nanotubes and specific organic molecules. Those results may contribute greatly to the applications, such as photocatalysis, and titanate nanotubes as a fuel-cell electrodes.

5.7 References

1. A. Fujishima, and K. Honda, *Nature*, **238,** 37 (1972).

2. J. Nowotny, T. Bak, M. K. Nowotony, and L. R. Sheppard, *J. Phys.Chem. B,* **110**, 18492 (2006).

3. T. Bak, J. Nowotny, M. Rekas, and C. C. Sorrell, *International journal of hydrogen energy*, **27,** 991 (2002).

4. S. U. Khan, M. Al-Shahry, and W. B. Ingler Jr, *Science*, **297,** 2243 (2002).

5. A. Mills, R. H. Davies, and D. Woresley, *Chem. Soc. Rev.*, **22**, 417 (1993).

6. A. Hagfeldt, and M. Gratzel., *Chem. Rev*., **95,** 49 (1995).

7. A. L. Linsebigler, G. Lu, and J. T. Yates, Jr, *Chem. Rev.*, **95,** 735 (1995).

8. A. Hagfeldt, and M. Gratzel, *Accounts of Chemical Research*, **33,** 269 (2000).

9. M. Graztel, *Nature*, **421,** 586 (2003).

10. M. Grazel, *J. of Photochemistry and Photobiology A:Chemistry.*, **164,** 3 (2004).

11. L. Schmidt-Mende, U. Bach., R. Humphry-Baker, T. Horiuchi, H. Miura, S. Ito, S. Uchida, and M. Gratzel, *Adv. Mater.*, **17,** 813 (2005).

12. P. Wang, C. Klein., R. Humphry-Baker,S. M. Zakeeruddin, and M. Gratzel, *J. Am. Chem. Soc.*, **127,** 808 (2005).

13. P. Wang, S. M. Zakeeruddin, R. Humphry-Baker, J. E. Moser, and M. Gratzel, *Adv. Mater*, **15,** 2101 (2003).

14. P. Wang, S. M. Zakeeruddin,, J. E. Moser, R. Humphry-Baker, P. Comte, V. Aranyos, A. Hagfeldt, M.. K. Nazeeruddin, and M. Gratzel, *Adv. Mater*, **16,** 1806 (2004).

15. T. Rajh, L. X. Chen., K. Lukas, T. Liu, M. C. Thurnauer, and D. M. Tiede, *J. of Phys. Chem. B*, **106,** 10543 (2002).

16. J. L. Dalsin, L. Lin., S. Tosatti, Janos Voros, M. Textor,and P. B. Messersmith, *Langmuir*, **21**, 640 (2005).

17. T. Rajh, J. M.Nedeljkovic., L. X. Chen, O. Poluektov, and M. C. Thurnauer, *J. Phys. Chem. B*, **103,** 3515 (1999).

18. R. Rodrguez, M. A. Blesa., and A. E. Regazzoni, *J. Colloid and Interface Science*, **177,** 122 (1996).

19. Z. V. Saponjic, N. M. Dimitrijevic., D. M. Tiede, A. J. Goshe, X. Zuo, L. X. Chen, A. S. Barnard, P. Zapol, L. Curtiss, and T. Rajh, *Adv. Mater*., **17**, 965 (2005).

20. A. Kleinhammes, G. W. Wagner., H. Kulkarni, Y. Jia, Q. Zhang, L.-C. Qin, Y. Wu, *Chem. Phys. Lett.*, **411,** 81 (2005).

21. G. H. Du, Q. Chen., R. C. Che, Z. Y. Yuan, and L.-M. Peng, *Appl. Phys. Lett.*, **79**, 3702 (2001).

22. M. Adachi, Y. Murata, and M. Harada, *Chem. Lett*., **8**, 942 (2000).

23. T. Kasuga, M. Hiramatsu., M. Hirano, A. Hoson, and K.Oyamada, *J. Mater.Res*, **12**, 607 (1997).

24. T. Kasuga, M. Hiramatsu, A. Hoson, and K.Oyamada, *Proceedings of the 2nd International Meeting of the Pacific Rim Ceramic Society*, Cairns, (1996).

25. T. Kasuga, M. Hiramatsu, A. Hoson, T. Sekino, and K. Niihara, *Langmuir*, **14**, 3160 (1998).

26. T. Kasuga, M. Hiramatsu, A. Hoson, T. Sekino, and K. Niihara, *Adv.Mater*. **11**, 1307 (1999).

27. Q. Chen, G. H. Du., S. Zhang, and L.-M. Peng, *Acta Crystallographica Section B*, 58, 587 (2002).

28. B. D. Yao, Y. F. Chan, X. Y. Zhang, W. F. Zhang, Z. Y. Yang, and N. Wang, *Appl. Phys. Lett.*, **82**, 281 (2003).

29. Y. Suzuki, and S. Yoshikawa, *J. Mater. Res*., **19**, 982 (2004).

30. S. Zhang, L.-M. Peng, Q. Chen, G. H. Du, G. Dawson, and W. Z. Zhou, *Phys. Rev. Lett.*, **91**, 256103-1 (2003).

31. S. Zhang, J. Zhou, and Z. Zhang, *Chin. Sci. Bull*, **45** 1533 (2000).

32. Q. Chen, W. Zhou., C. Du, and L-M Peng, *Adv. Mater.*, **14**, 1208 (2002).

33. J. Yang, Z. Jin., X. Wang, W. Li, J. Zhang, S. Zhang, X.Guo, and Z. Zhang, *Dalton Transitions*, 3898 (2003).

34. R. Ma, Y. Bando, T. Sasaki, *Chem. Phys. Lett.*, **380** 577 (2003).

35. R. Ma, Y. Bando, T. Sasaki, *J. Phys. Chem.B*, **108,** 2115 (2004).

36. D. V. Bavykin, J. M. Friedrich and F. C. Walsh, *Adv. Mater.*, **18**, 2807 (2006).

37. A. Fahmi and C. Minot, *Phys. Rev. B*, **47**, 11717 (1993).

38. J. K. Burdett, T. Hughbanks, G. J. Miller, J. W. Richardson, Jr., and J. V. Smith, *J. Am. Chem. Soc*, **109,** 3629 (1987).

39.W. Wang, O. K. Varghese., M. Paulose, and C. A. Grimes, *J. Mater. Res.*, **19**, 417 (2004).

40. D. V. Bavykin, V. N. Parmon, A. A. Lapkin, and F. C. Walsh, *J. Mater.Chem.*, **14**, 3370 (2004).

41. S. Zhang, Q. Chen, and L.-M. Peng,, *Phys. Rev. B,* **71**, 014104 (2005).

42. D. V. Bavykin, A. A. Lapkin, P. K. Plucinski, J. M. Friedrich, and F.C. Walsh, *J. Phys. Chem. B*, **109,** 19422 (2005).

43. X. Sun, and Y. Li., *Chem. Eur. J*, **9**, 2229 (2003).

44. R. Ma,T. Sasakia and Y. Bando, *Chemical Communications*, **7**, 948 (*2*005).

45. D. V. Bavykin, A. A. Lapkin, P. K. Plucinski, J. M. Friedrich, and F.C. Walsh, *J. Catal.*, **235**, 10 (2005).

46. Y. Wang, K. Hang, N. A Aderson and T. Lian, *J. Phys.Chem. B*, **107**, 9434 (2003).

47.A. Vittadini, A. Selloni, F. P. Rotzinger, and M. Gratzel, *Phys. Rev.Lett.*, **81**, 2964 (1998).

48. J. Moser, S. Punchihewa, P. P. Infelta, and M. Gratzel, *Langmuir,* **7**, 3012 (1991).

49. C. R. Rice, M. D. Ward, M. K. Nazeeruddin, and M. Gratzel, *New Journal of Chemistry,* **24**, 651 (2000).

51. L. G.C, Rego and V. S. Batista, *J. Am. Chem. Soc*., **125**, 7989 (2003).

52. Y. Liu, J. I. Dadap, D. Zimdars, and K. B. Eisenthal, *J. Phys. Chem. B*, **103**, 2480 (1999).

53. P. C. Redfern, P. Zapol, L. A. Curtiss, T. Rajh, and M. C. Thurnauer. *J. Phys.Chem. B*, **107,** 11419 (2003).

54. T. Lana-Villarreal, A. Rodes, J. M, Perez, and R. Gomez, *J. Am. Chem. Soc,* **127**, 12601 (2005).

55.L. X. Chen, T. Rajh, Z. Wang, and M. C. Thurnauer, *J. Phys.Chem. B*, **101**, 10688 (1997).

56. T. Kasuga, M. Hiramatsu, A. Hoson, T. Sekino, K. Niihara, *Langmuir*, **14**, 3160 (1998).

57. R. Ma, K. Fukuda, T. Sasaki, M. Osada, and Y. Bando, *J. Phys. Chem. B*, **109**, 6210 (2005).

58. L. Qian, Z.-L. Du., S.-Yi Yang, and Z.-S. Jin, *J. Molecular Structure*, **749**, 103 (2005).

59. M. Hodos, E. Horvath, H. Haspel, K. Kukovecz ,Z. Konya, and I. Kiricsi *Chem. Phys. Lett,* **399**, 512 (2004).

60. F. Miyaji, T. Yoko., H. Kozuka, and S. Sakka, *J. Mater. Sci.,* **26**, 248 (1989).

61. H. M. Kim, F. Miyaji, and T. Kokubo, *J. Mater. Sci.: Mater. Med.*, **8**, 341 (1997).

62. B. C. Bunker, C. H. F. Peden, D. R. Tallant, S. L.Martinez and G. L. Turner, *Mater. Res. Soc. Symp. Proc.*, **121**, 105 (1988).

63. S. Sakka, F. Miyaji.and K. Fukumi., *J. Non-Cryst.Solids*, **112**, 64 (1989).

64. S. H. Byeon, S. O. Lee., and H. Kim, *J. Solid State Chem.*, **130**, 110 (1997).

65. C. H. Lin, S. H.Chien., J. H. Chao, C. Y. Sheu, Y. C. Cheng, Y. J.Huang, and C. H. Tsai,, *Catal. Lett.*, **80**, 153 (2002).

66. J. Cao, J. -Z. Sun., H. -Y. Li, J. Hong, and M. Wang, *J. Mater. Chem.*, **14**, 1203 (2004).

67. J. -C. Xu, M. Lu, X. -Y. Guo, and H. -L. Lia,, *J. Mol. Catal. A*, **226**, 123 (2006).

68. Y. -G. Wang, and X. -G. Zhang., *Electrochim. Acta*, **49**, 1957 (2004).

69. S. Uchida, R. Chiba., M. Tomiha, N. Masaki, and M. Shirai, *Electrochemistry*, **70**, 418 (2002).

70. Y. Ohsaki, N. Masaki, T. Kitamura, Y. Wada, T. Okamoto, T. Sekino, K. Niiharab, and S. Yanagida, *Phys. Chem. Chem. Phys.*, **7**, 4157 (2005).

71. G. K. Mor, K. Shankar, M. Paulose, O. K. Varghese, and C. A, Grimes, **6**, 215 (2006).

CHAPTER 6

HYBRID STRUCTURE OF TITANATE NANOTUBE AND ORGANIC MOLECULES

As mentioned in **Chapter 5** the different binding configurations of catechol on nanoparticle surfaces (e.g. monodentate and bidentate structures) lead to the different adsorption energies, and may induce different structural changes of TiO_2 nanoparticles. Similar to TiO_2 nanoparticles, our result shows that when titanate nanotubes were exposed to organic molecules, e.g. catechol, their color changes along with changes of local structures. In order to study the mechanisms of different binding configurations and the induced structure changes experimentally, I chose three different molecules: hydroquinone, 4-methoxypenol(MEHQ) and catechol. Each of these three molecules is expected to form a different binding configuration. The optical and structure properties of titanate nanotubes and the three hybrid structures (titanate nanotube/hydroquinone, titanate nanotube/MEHQ and titanate nanotube/catechol) were characterized by multiple techniques, such as UV-Vis, Raman spectroscopy, X-ray diffraction, thermal gravity analysis (TGA) and NMR spectroscopy.

In **Chapter 6** the experimental results are discussed in detail, starting with the synthesis processes of the titanate nanotubes and titanate nanotube/organic molecule hybrid, followed by the properties characterization of the hybrid structures using UV-Vis, Raman spectroscopy, X-ray diffraction and NMR spectroscopy, etc. Through comparing the results of the three hybrid structures, it is found that by forming bidentate structures, organic molecules (hydroquinone and catechol) and titanate nanotubes can form hybrid structures which are relatively stable in an aqueous environment. Also, it was demonstrated that the local structure of titanate nanotubes can be changed into an anatase-like structure by the incorporation of organic molecules.

6.1 Experimental Details

6.1.1 Synthesis of Titanate nanotubes

All chemicals were obtained from Aldrich and used without further purification.

Titanate nanotubes were produced by hydrothermal synthesis. 4 g of TiO_2 anatase nanocrystal powder with an average nanocrystal diameter of 32 nm was immersed in 560 g of 10-molar NaOH and was heated in a Teflon®-lined autoclave at 130°C for 72 hours. The precipitate produced was equally divided. One sample, referred to here as acid-washed titanate nanotubes (Ti-a), was post treated by successively washing with distilled H_2O, 0.1-molar HCl, H_2O, H_2O, 0.1-molar HCl, H_2O, H_2O. The pH of the precipitate dropped below 3 after the first HCl washing, and increased to a pH of 5 (the distilled water used has pH 5) over subsequent washes. The precipitate was then dried at 55°C for 3-5 hours to yield a white powder of nanotubes. The second sample, referred here as water-washed titanate nanotubes (Ti-w) was washed repeatedly with distilled H_2O up to 35 times until the solution became neutral (pH =5). The precipitate was then dried at 55°C for 3-5 hours to yield a white powder of nanotubes.

6.1.2 Synthesis of Titanate Nanotube/Organic Molecule Hybrid Structure

As mentioned in Section 5.5.2.1.2, water could compete with molecules like catechol to react with Ti defect sites. Here, instead of H_2O, methacrylic acid (MAA) was used as the solvent to dissolve solid HQ. The advantages are (1) HQ is stable in MAA; (2) the solubility of HQ in MAA is much higher (>3 times higher) than that of HQ in H_2O in the temperature range 25-70°C;(3) the anchoring functional group of HQ (hydroxyl group) is more effective than that of MAA (carboxylic group)[1], in other words, HQ is more reactive than MAA to react with Ti defect sites. For the loading of hydroquinone (HQ) (catechol (CAT) or 4-methoxyphenol (MEHQ)), a solution was prepared by dissolving 3.5 mmol HQ (CAT, or MEHQ) powder in 20 ml MAA at 70°C. The commercial MAA contains either an initial HQ or MEHQ content of 100-250 ppm as an inhibitor for polymerization. The structure and relevant dimensions of HQ, CAT and MEHQ are shown in Fig. 6.1. Both acid-washed and water-washed titanate nanotubes were exposed through the same sequence to organic molecules: 0.2 g of washed nanotubes (Ti-a, Ti-w) were added to the HQ (MEHQ, CAT) solution and kept at 70°C for 48 hours (this treatment temperature and time were used unless mentioned otherwise). The precipitate was then separated from the solution by filtration. It was either dried at room temperature (RT) then used directly for various characterizations, or annealed at 140°C for 2 hours under N_2 flow and then used for various characterizations. Samples are designated by the washing procedure, the attached organic molecule, and

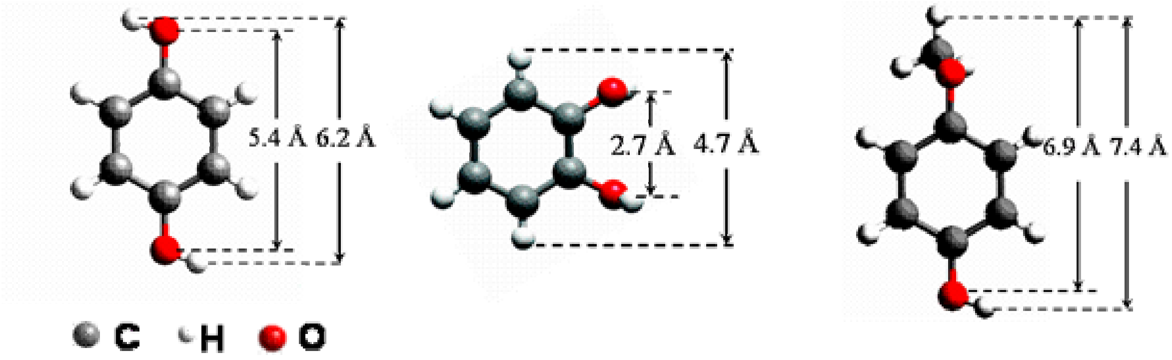

Figure 6.1 Molecular structures and relevant dimensions of (a) HQ, (b) CAT and (c) MEHQ.

the processing temperature: e.g. HQ-Ti-w-140°C – water-washed titanate nanotubes exposed to HQ at 70°C for 48 hrs and annealed at 140°C; HQ-Ti-a-70°C – acid-washed titanate nanotubes expose to HQ at 70°C for 48 hrs and dried at RT. To study the concentration effect of HQ treatment, the titanate nanotubes were treated with a smaller amount of HQ, shorter reaction time and lower reaction temperature: 0.025 HQ powder was dissolved in 20 ml MAA at RT, and 0.2 g of Ti-a (w) nanotubes was added to the HQ solution and kept at RT for 2 hours. The precipitate was filtered and dried at RT afterwards. This sample is denoted as HQ-Ti-a (w)-RT.

6.1.3 Measurements

UV-visible reflection spectra were recorded using a Shimadzu UV-3600 spectrophotometer with an integrating sphere (ISR-3100, Shimadzu). Raman experiments were performed using a Dilor XY triple-monochromator Raman spectrometer with a liquid-nitrogen-cooled CCD detector. The excitation wavelength was 514.5 nm using a Spectra-Physics Ar^+ ion laser. XRD patterns were collected on a diffractometer with a monochromatized Cu-$K\alpha$ radiation ($\lambda = 0.15405$ nm). Nuclear magnetic resonance (NMR) measurements were carried out with a 400 MHz using a Chemagnetics spectrometer and 4-mm magic angle spinning (MAS) probe. All experiments were done on non-enriched samples due to the unavailability of enriched ^{13}C HQ or CAT.

6.2 Results and Discussion

6.2.1 Titanate Nanotube/Hydroquinone Hybrid Structure

6.2.1.1 TEM and SEM Images

The TEM image shown in Fig. 6.2 (a) reveals that Ti-a nanotubes have the tubular structure with an inner diameter of 5 nm and an outer diameter of 10 nm. Fig. 6.2 (b) and (c) are TEM images of HQ-Ti-a-70°C and 140°C. Clearly, the tubular structure is maintained after HQ treatment.

Figure 6.3 (a) and (b) are scanning electron microscopy (SEM) images of Ti-a and Ti-w nanotubes, respectively. It shows that Ti-a nanotubes exist as bundles composed of 3~4 nanotubes, while Ti-w nanotubes are separated single tubes. The Ti-a and Ti-w nanotubes were treated with exactly the same steps except for the post washing processes. The different morphologies between Ti-w and Ti-a nanotubes could be induced by the washing treatments. During the multiple water washing process, up to 35 times, H_2O changes the concentration and distribution of OH^- groups[2] of precursor nanotubes by dissociative adsorption, as well as the Na^+ content[3] in the nanotube framework. All OH^- groups on the surfaces (internal and external) of the nanotubes, as well as in the interlayer region, are accessible for small molecules, like HQ, which determine nanotubes' chemistry.[4] Different configurations of OH^- groups and Na^+ content in Ti-a and Ti-w nanotubes lead to changes of local framework structure and coordination states of Ti atoms. More details will be discussed later in this chapter.

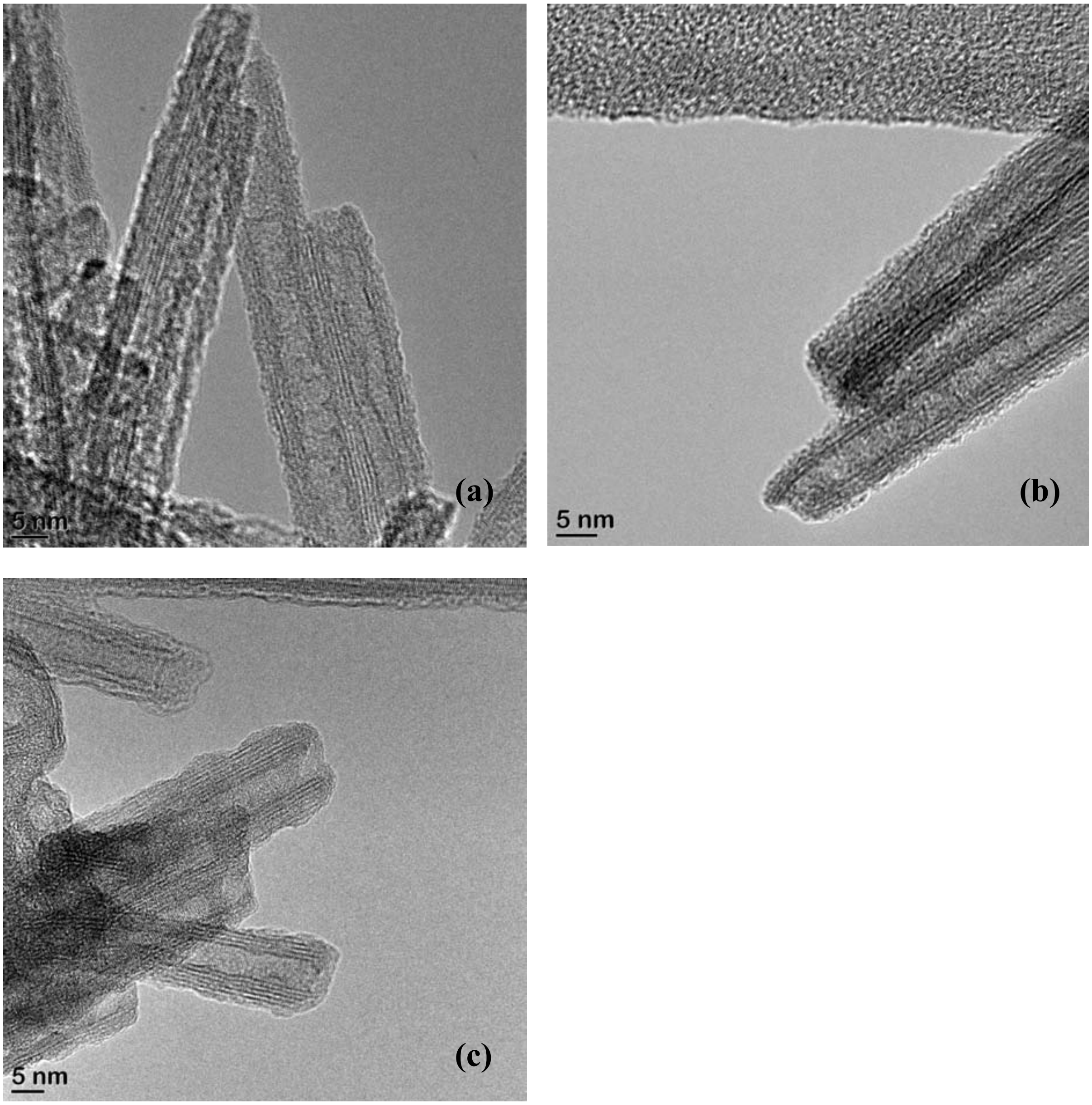

Figure 6.2 TEM images of (a) as-synthesized Ti-a nanotubes; (b) HQ-Ti-a-70°C, (c) HQ-Ti-a-140°C.

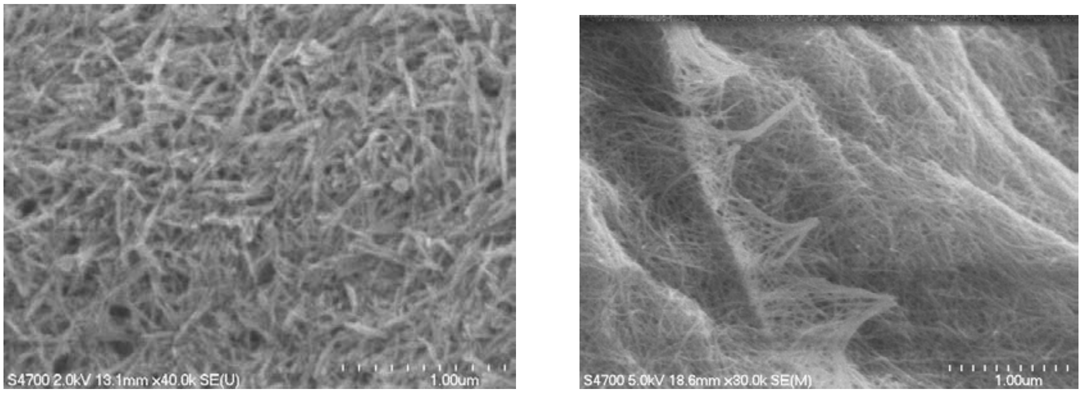

(a) **(b)**

Figure 6.3 SEM images of as-synthesized titanate nanotubes. SEM image of acid washed titanate nanotubes (Ti-a). (b) SEM image of water washed titanate nanotubes (Ti-w).

6.2.1.2 UV-Vis Spectra

Figure 6.4 shows the UV-vis reflection spectra of solid HQ, as-synthesized Ti-a, Ti-w titanate nanotubes, HQ-Ti-a-70°C and HQ-Ti-w-70°C. The thresholds of absorption for titanate nanotubes, both Ti-a and Ti-w, are at 380 nm and that of the solid HQ is at 320 nm. As a result of HQ treatment, the spectra show broad absorption peaks for HQ-Ti-a and Ti-w nanotubes extending significantly beyond 700 nm (Fig. 6.4 (d) and (e)), leading to the reddish color of the HQ-treated nanotube powder, as shown in Fig 6.5 (c) and (c'). The red shift in the titanate nanotube absorption spectrum induced by attaching HQ is consistent with that of TiO_2 nanoparticles with the attachment of catechol, as mentioned in Section 5.5.2.1.3. The red shift is probably due to the formation of Ti-O bonds between HQ and nanotubes at the defect site. The excitation occurs from a molecular orbital primarily associated with HQ carbon atoms, to a molecular orbital delocalized on some of the titanium atoms and corresponds to charge transfer from the HQ to the titanate nanotubes. The stronger the interaction between HQ's and titanate nanotubes' energy levels, the larger the red shift of the absorption edge of HQ treated nanotubes. Compared to that of HQ-Ti-w-70°C, the absorption peak of HQ-Ti-a-70°C is red shifted 70 nm further to larger wavelength at the half height (Fig. 6.4 (d)). As mentioned above, this shift may be induced by the different configurations of surface functional groups, e.g. OH^- groups, in Ti-a and Ti-w nanotubes, leading to the different interactions between HQ and nanotubes in HQ-Ti-a-70°C and HQ-Ti-w-70°C samples.

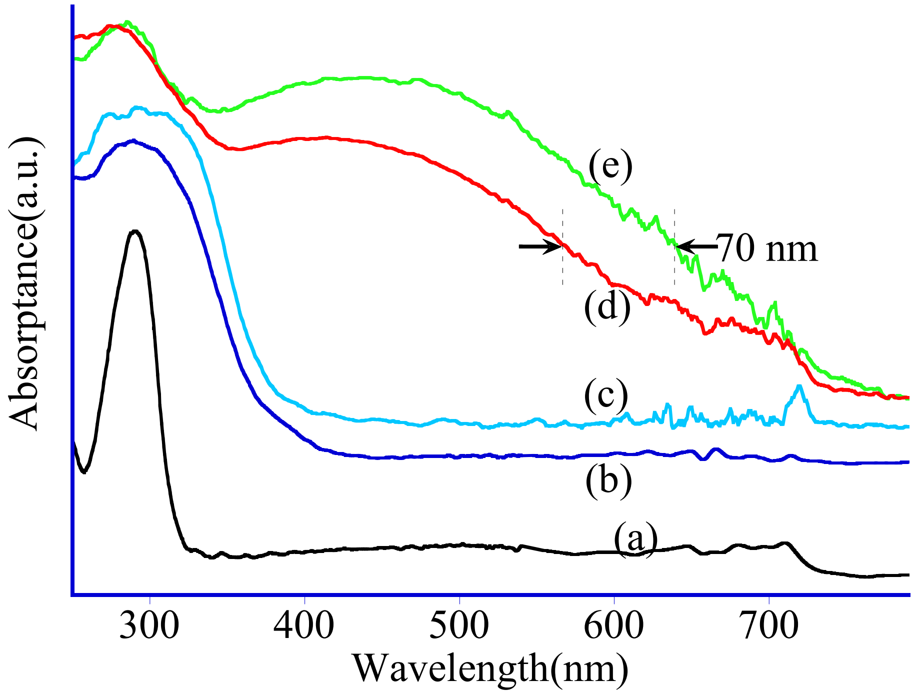

Figure 6.4 UV-vis absorption of (a) HQ solid, (b) as-synthesized Ti-w nanotubes, (c) as-synthesized Ti-a nanotubes (d) HQ-Ti-w-70°C, (e) HQ-Ti-a-70°C.

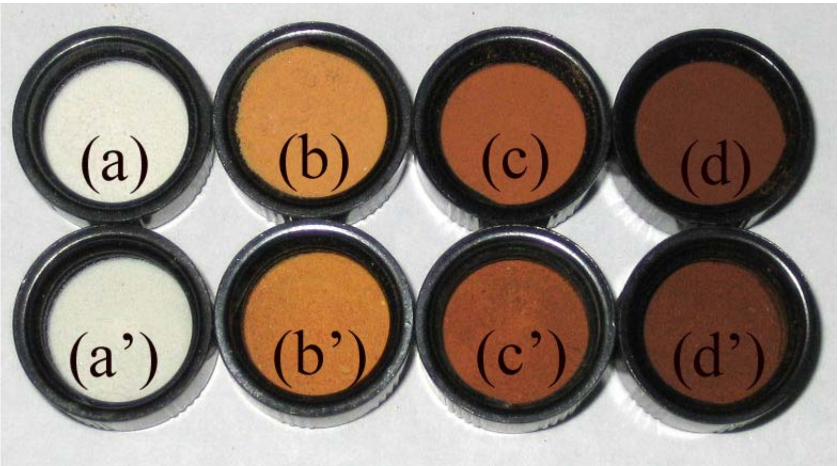

Figure 6.5 Different colors of various samples. (a) as-synthesized Ti-a nanotubes, (a') as-synthesized Ti-w nanotubes, (b) MEHQ-Ti-a-70°C, (b') MEHQ-Ti-w-70°C, (c) HQ-Ti-a70°C, (c') HQ-Ti-w-70°C, (d) CAT-Ti-a-70°C, (d') CAT-Ti-w-70°C.

6.2.1.3 Raman Spectra

Figure 6.6 shows the Raman spectra of anatase, Ti-a and Ti-w nanotubes. As reported previously,[5] the dominant Raman peaks of anatase (144 cm^{-1}, 196 cm^{-1}, 394 cm^{-1}, 509 cm^{-1} and 634 cm^{-1}) and nanotubes (279 cm^{-1}, 449 cm^{-1} and 660~710 cm^{-1}) are very different. The dominant E_g mode in anatase TiO_2 at 144 cm^{-1}, which was attributed to O-Ti-O bending[6, 7], is completely missing in the spectrum of as-synthesized nanotubes. So far, there is no consensus on the assignments of nanotube Raman peaks due to the lack of a structural model. Kokubo, *et al*. suggested that the third Raman peak, at 660 cm^{-1} for Ti-w and 710 cm^{-1} for Ti-a is due to an O-Ti-O bending and stretching vibration.[8] However, Kasuga *et al.* had a different opinion, claiming this peak was due to a Na-O-Ti vibration mode.[9]

Structural differences between the Ti-a and Ti-w nanotubes induced by different washing treatments are revealed by the differences observed in the Raman spectras around 660 cm^{-1}. Ti-a shows one peak at 660 cm^{-1} while Ti-w shows a broader peak composed of several lines. In Ti-w spectrum, additional features are present at around 710 and 830 cm^{-1}, indicating changes of the local framework structure and coordination states of the nanotubes upon washing. These different surface properties between Ti-a and Ti-w lead to the significantly different Raman spectra of these nanotubes upon HQ treatment.

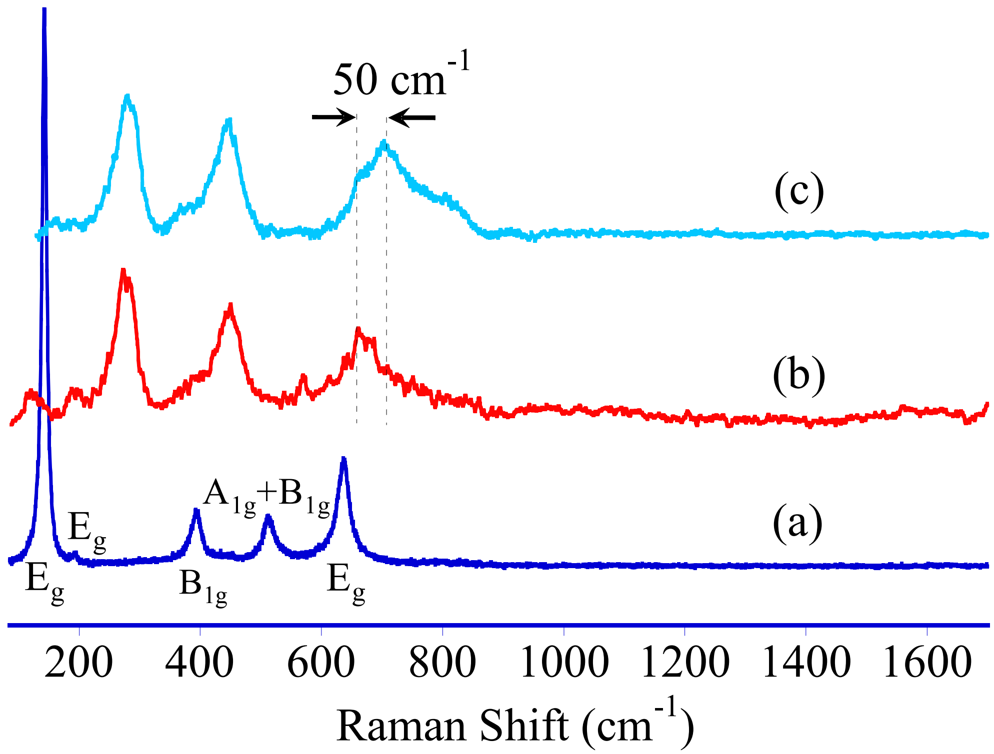

Figure 6.6 Raman spectra of (a) anatase TiO_2 nanocrystals, (b) as-synthesized Ti-a nanotubes, (c) as synthesized Ti-w nanotubes.

Figure 6.7 shows the Raman spectra of solid HQ, as-synthesized Ti-w nanotubes and HQ-Ti-w-70°C. Those peaks of solid HQ at higher wavenumbers (1110~1700 cm^{-1}) were also detected in HQ-Ti-w-70°C. The broadening of those peaks in HQ-Ti-w-70°C indicates the formation of bondings between the HQ molecule and the nanotube surface, which causes the red shifts in UV-vis spectra shown in Fig 6.4. The Raman peaks of HQ at lower wavenumbers (120~1110 cm^{-1}) were not observed in HQ-Ti-w-70°C, and it may be because the peaks are greatly broadened and overlapping with Ti-w peaks. Unfortunately, the assignments of the solid HQ Raman peaks are currently unavailable. Further theoretical investigation regarding the Raman peak assignment is of great importance to understand the mechanism of the bonding between HQ and nanotubes and the induced structural changes.

The positions of the three dominant peaks of Ti-w nanotubes are not affected by HQ treatment. However, in the HQ-Ti-w-70°C spectrum, both the intensities of the peaks at 270 cm^{-1} and 450 cm^{-1} with respect to the peak at 710 cm^{-1} are reduced compared to as-synthesized Ti-w nanotubes, which is a reflection of the subtle local structure changes of nanotubes induced by HQ ligands binding.

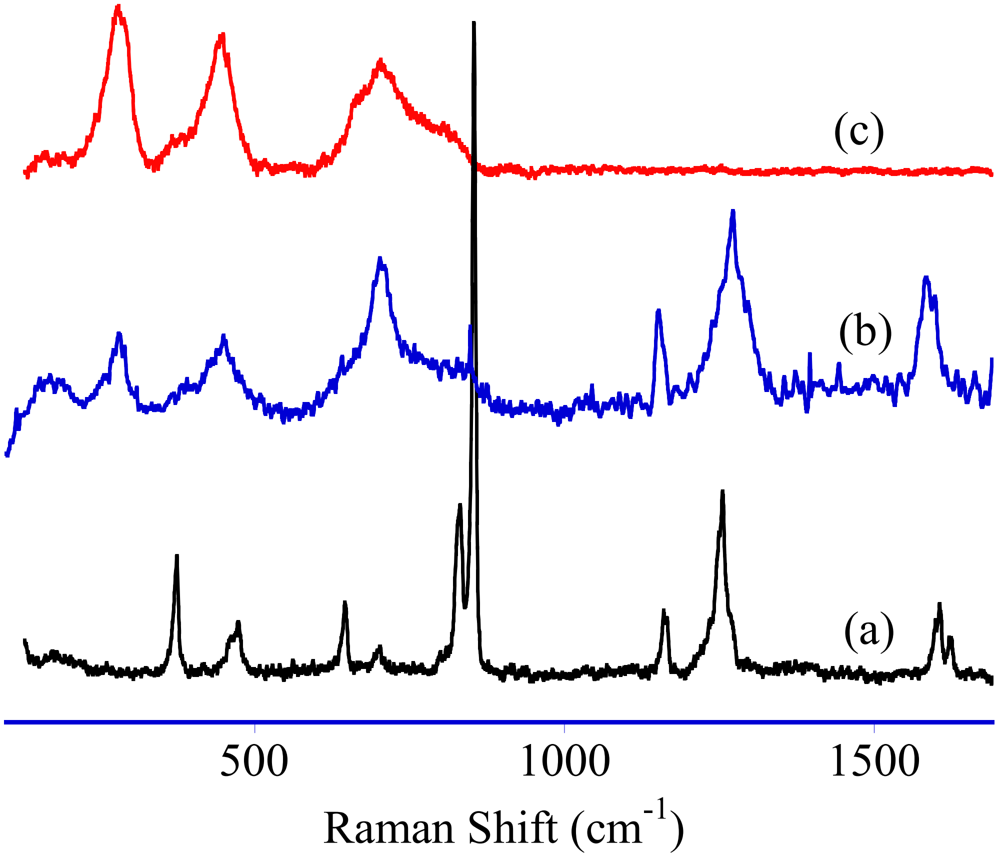

Figure 6.7 Raman spectra of (a) solid HQ, (b) HQ-treated Ti-w nanotubes, (c) as-synthesized Ti-w nanotubes.

Distinctively different from HQ-Ti-w-70°C, the anatase TiO_2 Raman spectrum was restored in HQ-Ti-a-70°C except for a small shift of the 144 cm^{-1} E_g mode (Fig. 6.8). When the HQ treatment of Ti-a nanotubes is done at RT and low HQ concentration (HQ-Ti-a-RT), the Raman spectrum shows a superposition of the spectra of anatase TiO_2 and as-synthesized

Ti-a nanotubes. A sufficient amount of HQ is needed to incorporate enough HQ and make the conversion to the anatase-like Raman spectrum complete. At higher wavenumbers (1110~1700 cm^{-1}) faint and broadened Raman peaks representing solid HQ were observed in the spectrum of HQ-Ti-a-70°C (Fig. 6.8 d). The broadening of the peaks indicates the formation of bonding between HQ and Ti-a nanotubes. In HQ-Ti-a-RT, only one HQ peak at 1597cm^{-1} appears and the intensity is weak, indicating a limited amount of HQ bonding to the Ti-a nanotube surface due to the low concentration of HQ in MAA solvent. In HQ-Ti-a-140°C spectrum, the Raman peaks of HQ are greatly broadened and cannot be observed, which is probably caused by the strong bonding between HQ and the Ti-a nanotube surface formed during annealing at 140°C.

During the sample preparation, MAA or 140°C annealing might also induce changes to the local structure of nanotube framework. In order to clarify the role of MAA and annealing at 140°C to the Ti-a nanotube structure, Ti-a nanotubes were exposed to pure MAA solution (inhibited by 110 ppm MEHQ). The mixture was kept at 70°C for 48 hrs, and the precipitate was separated by filtration. It was either dried at RT (MAA-Ti-a-70°C) then used directly for Raman measurement, or annealed for 2 hours under N_2 flow (MAA-Ti-a-140°C) and then used for Raman measurement.

Fig. 6.8 shows the Raman spectra of Ti-a nanotubes, MAA-Ti-a-70°C and MAA-Ti-a-140°C. The positions of the three dominant peaks of MAA-Ti-a-70°C and MAA-Ti-a-140°C are the same as those of Ti-a nanotubes. The shapes and intensities of the peaks change slightly, reflecting subtle local structure changes of nanotubes induced by attachment of MAA, or annealing at 140°C. Clearly, the structure reconstruction to the anatase-like structure is induced by HQ molecules rather than MAA or annealing at 140°C.

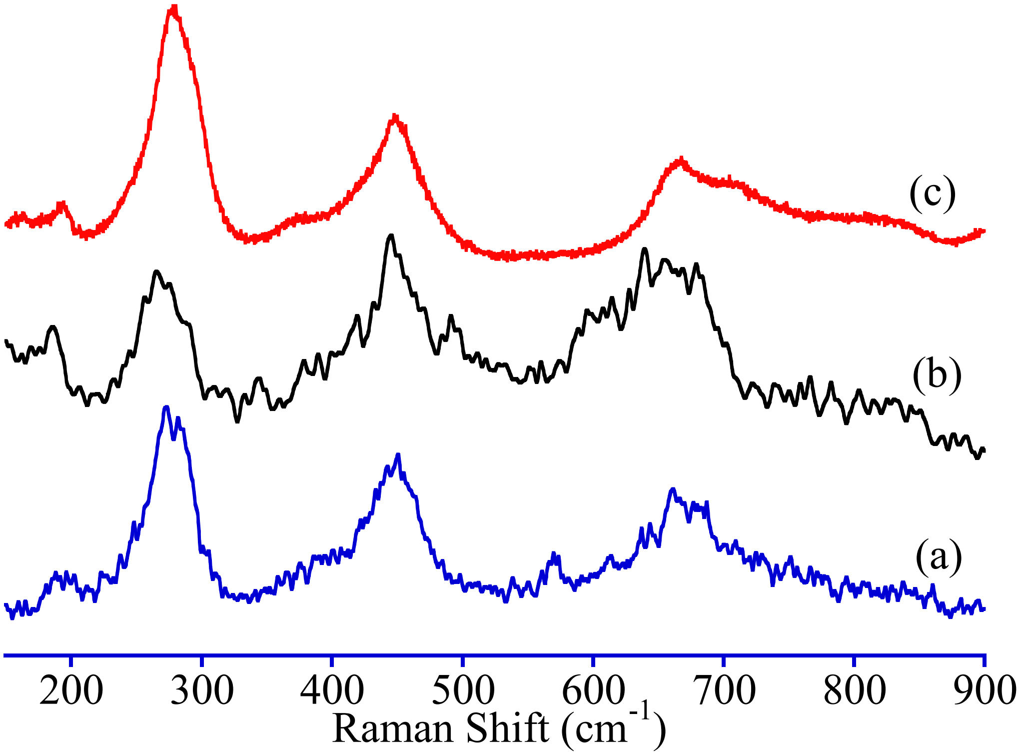

Figure 6.8 Raman spectra of (a) as-synthesized Ti-a nanotubes, (b) MAA-Ti-a-70°C, (c) MAA-Ti-a-140°C.

The change of the Raman spectrum upon HQ treatment indicates that defects and undercoordinated Ti atoms in nanotubes were restored to anatase-like local structures. Since the Raman spectrum of HQ-treated nanotubes can be attributed completely to anatase-like local structures, it suggests that most of the undercoordinated Ti atoms are removed by HQ treatment, including the majority of the sites that can be accessed only through diffusion in-between the layers. HQ can react with the undercoordinated Ti sites on the surface via one or both of their hydroxyl groups (Fig.7.1 (a)). Moreover, HQ could react in the outer, inner surfaces and interlayer region of nanotubes with one undercoordinated Ti atom through one of its hydroxyl groups (monodentate structure). HQ could also react in the interlayer region with two undercoordinated Ti atoms on opposite sides, linking two adjacent nanotube layers (bidentate structure), as illustrated in Figure (6.10). Monodentate and bidentate bonding of HQ could both be present in HQ treated Ti-a nanotubes, as will be discussed later.

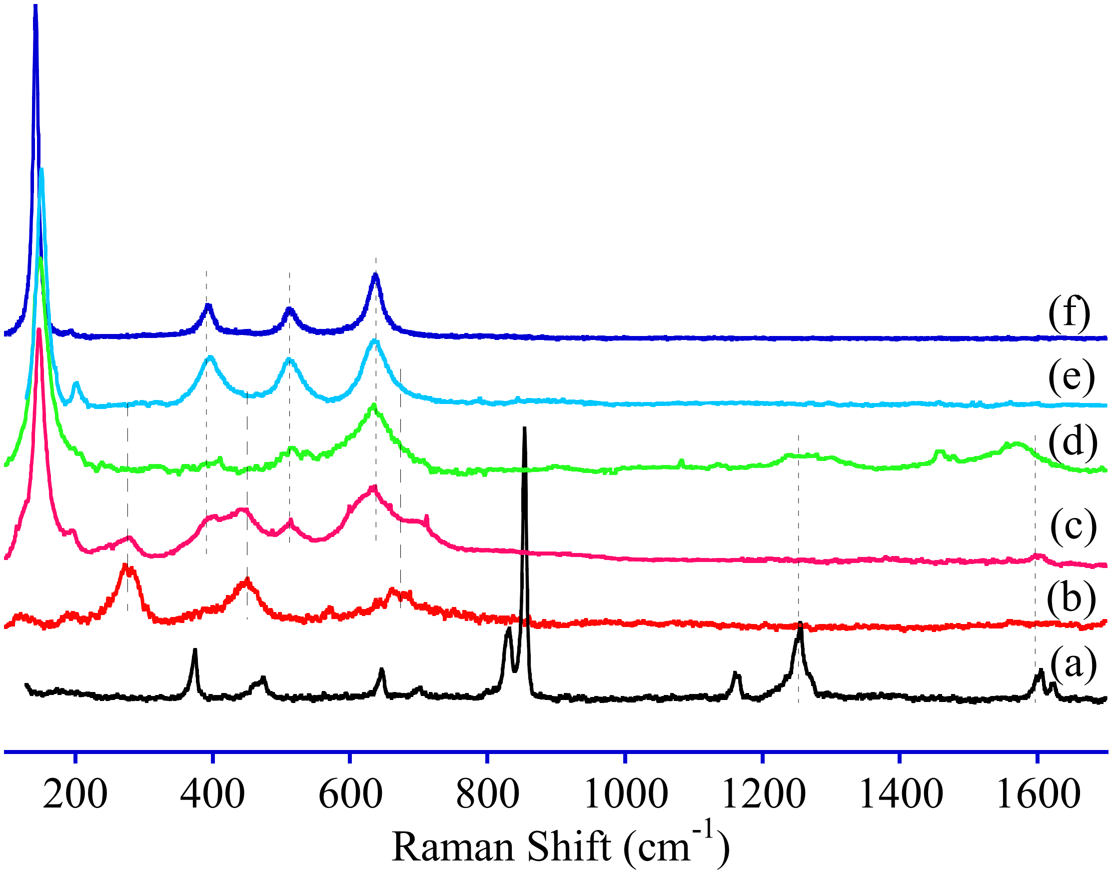

Figure 6.9 Raman spectra of (a) solid HQ, (b) as-synthesized Ti-a nanotubes, (c) HQ-Ti-a-RT, (d) HQ-Ti-a-70°C, (e) HQ-Ti-a-140°C, (f) anatase TiO_2 nanocrystals.

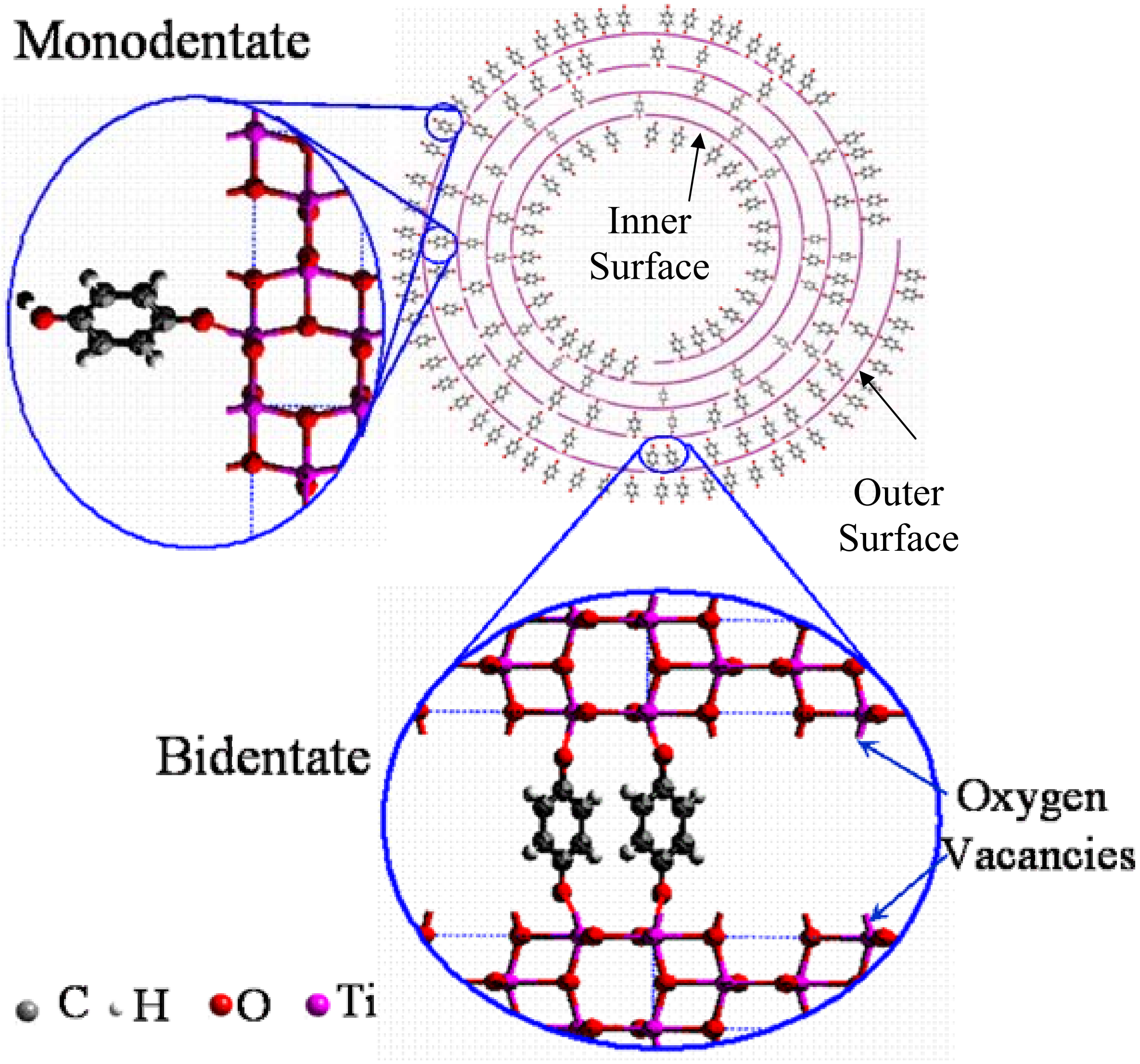

Figure 6.10 Schematic depiction of monodentate and bidentate bonding to Ti-a nanotube surfaces.

An issue of significant importance for applications is the structural stability of the Ti-a nanotube/HQ hybrid system in the aqueous environment. Except for the HQ-Ti-a-140°C sample, soaking the HQ-treated samples in water for a few days causes the reddish color to fade and the Raman spectrum to return to that of as-synthesized Ti-a nanotubes, as shown in Fig. 6.11. However, only a slight color fading was observed in the HQ-treated sample annealed at 140°C after soaking in water for 7 days. Its Raman spectrum, as shown in Fig.

6.11 (d), remains largely anatase-like with only a small contribution attributed to as-synthesized Ti-a nanotubes. The latter could originate from the outer, inner surfaces and possibly the interlayer region of the nanotubes where HQ did not bind stably with the Ti-a nanotube surface in the aqueous environment. As will be mentioned later, the unstable bonding is because those HQ did not react with both hydroxyl groups binding to two adjacent surfaces of the nanotube, forming a bidentate structure; instead, they formed monodentate bonding via one hydroxyl group. Issues about the mechanism of annealing, how annealing could enhance the strength of the bidentate bonding and stabilize the hybrid structure, are still unclear yet, and further investigation is needed to clarify those points.

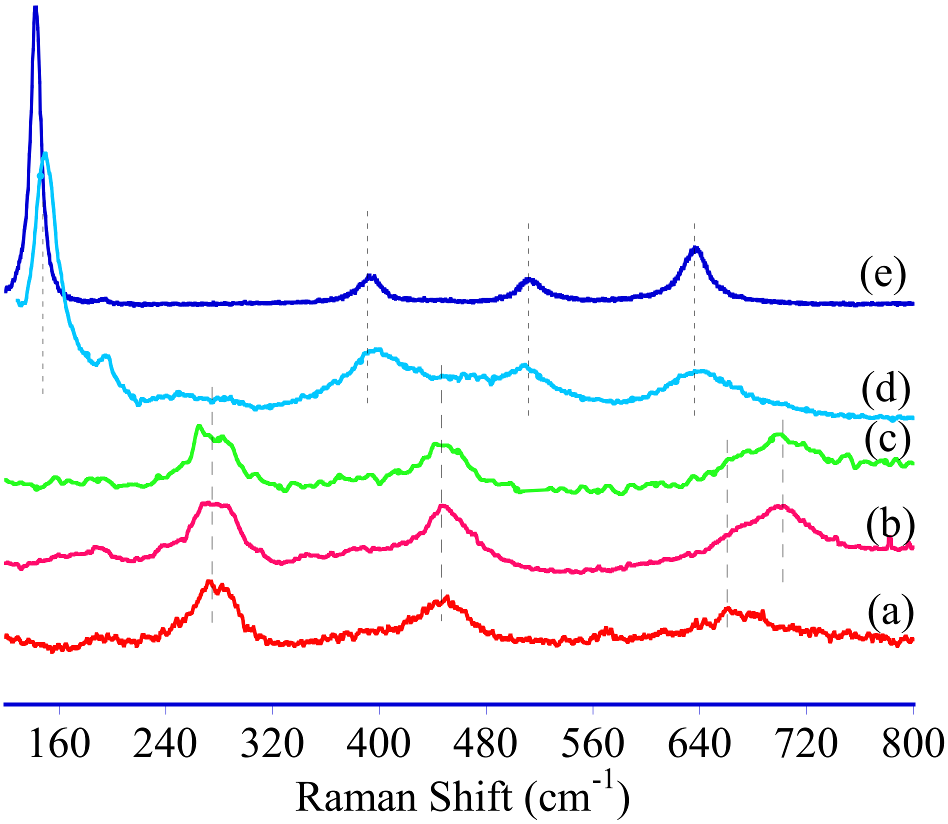

Figure 6.11 Raman spectra of (a) as-synthesized Ti-a nanotubes, (b) HQ-Ti-a-RT soaked in H_2O for 2 hours, (c) HQ-Ti-a-70°C soaked in H_2O for 7 days, (d) HQ-Ti-a-140°C soaked in H_2O for 7 days. (e) anatase TiO_2 nanocrystals.

Moreover, in the spectra of HQ-Ti-a- RT and HQ-Ti-a-70°C soaked in H_2O (Fig 6.11 (b) and (c)), a significant shift of the third Raman peak (originally at 660 cm^{-1}) is observed before and after washing. The peak is shifted to ~710 cm^{-1}, which is very close to the position of the third peak of the Ti-w nanotubes. It indicates that the local framework and coordination of the Ti atom in HQ treated Ti-a nanotubes are transformed from anatase-like to the structure characteristic of Ti-w nanotubes, instead of returning to the structure of Ti-a nanotubes. According to Redfern *et al*,[2] water could remove undercoordinated Ti defect sites by dissociative adsorption (also see Section 5.5.2.1.1), which would induce changes of the local structure of the Ti atom in nanotubes. Thus, in the aqueous condition, water molecules could compete with HQ to react with a Ti defect site. In the HQ-Ti-a-RT and HQ-Ti-a-70°C, the bonding between H_2O and the undercoordinated Ti atom seems more stable than that between HQ and Ti sites. Gradually, HQ molecules are replaced by H_2O and the local structure in the vicinity of the Ti atoms is also transformed to that of as-synthesized Ti-w nanotubes. However, in the HQ-Ti-a-140°C sample, the bonding between HQ and the Ti sites becomes stronger than that between H_2O and Ti, possibly due to structural relaxation upon annealing. Therefore, the hybrid structure of the Ti-a nanotube/HQ is stable in water and the structure remains anatase-like (Fig. 6.11 (d)).

6.2.1.4 NMR Spectra

Figure 6.12 shows ^{13}C NMR spectra of solid HQ, liquid MAA, and HQ-Ti-a-70°C using decoupling and cross polarization (CP) (see Appendix for details). In the spectrum of solid HQ (Fig. 6.12 b), the peak at 150.8 ppm represents the ^{13}C nuclei that anchor the hydroxyl group, and the peak at 116.5 ppm represents the remaining equivalent carbons in the aromatic ring (Fig 6.14(a)). The peak assignments of the MAA spectrum are

$H_2C(2)=C(3)(C(1)H_3)C(4)OOH$ as shown in Fig. 6.12 a. In the HQ-treated nanotube spectrum there are two peaks originating from ^{13}C nuclei associated with the hydroxyl group: one is at 150.1 ppm, corresponding to the ^{13}C connected to free hydroxyl group (Fig 6.14 (a)); the second peak is shifted to 160.0 ppm, corresponding to the ^{13}C connected to Ti atom via oxygen (Fig 6.14 (a_2)). The observed shift difference between attached and unattached HQ is in agreement with first principles calculations. This demonstrates that HQ anions are indeed chemically bound to the nanotube surfaces forming a nanotube/HQ hybrid system. The intensities of the two peaks are approximately the same, indicating two possible mechanisms: 50 % of HQ are physically absorbed (Fig. 6.14 (a_1)) on the surfaces of Ti-a nanotubes and the other 50 % of HQ are chemically bound to the nanotube surface by the bidentate structure (Fig. 6.14 (a_3)); or the majority of HQ is chemically bound to the Ti-a nanotube surface by forming the monodentate structure (Fig. 6.14 (a_2)). Since repeated NMR measurements of various samples all show equal intensities for the two hydroxyl peaks in HQ-Ti-a-70°C, and such a coincidence of 50% bound and 50% unbound is unlikely, we favor the interpretation that the majority of HQ anions are chemically bound to the nanotube surfaces by monodentate bonding. Moreover, as will be discussed in detail in **6.2.2,** bidentate bonding of some HQ is needed to maintain the stable anatase-like local structure of Ti-a nanotubes in the aqueous environment after 140°C annealing. Thus, compared to the majority of HQ, which forms monodentate bonding to the nanotube surface, the amount of HQ forming bidentate bonding in 140°C annealed samples might be small, but it is still sufficient to reconstruct the local structure to the anatase-like structure and keep the reconstruction stable in water.

As discussed previously, the Raman experiment shows that no structural change is induced by pure MAA (Fig. 6.11), neither is there a color change. This indicates that MAA does not play a direct role in the HQ-induced structural changes. However, it is also clear from the ^{13}C NMR spectra that some MAA molecules are also incorporated in the nanotube structure. It was calculated that in the HQ-Ti-a-70°C sample, the molecular ratio of HQ to MAA is 1:2.3 by comparing the integration area of HQ and MAA peaks.

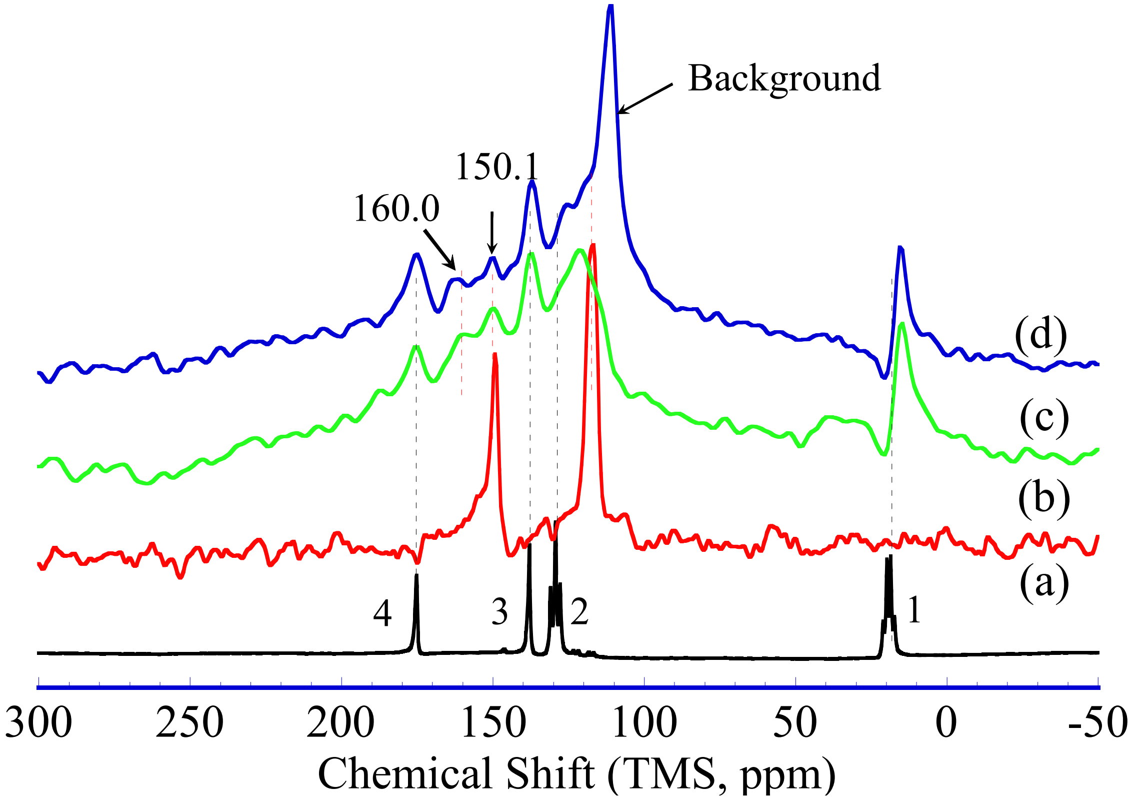

Figure 6.12 ^{13}C NMR spectra of (a) liquid MAA, (b) solid HQ, (c) HQ-Ti-a-70°C observed using CP, (d) HQ-Ti-a-70°C using direct detection with proton decoupling.

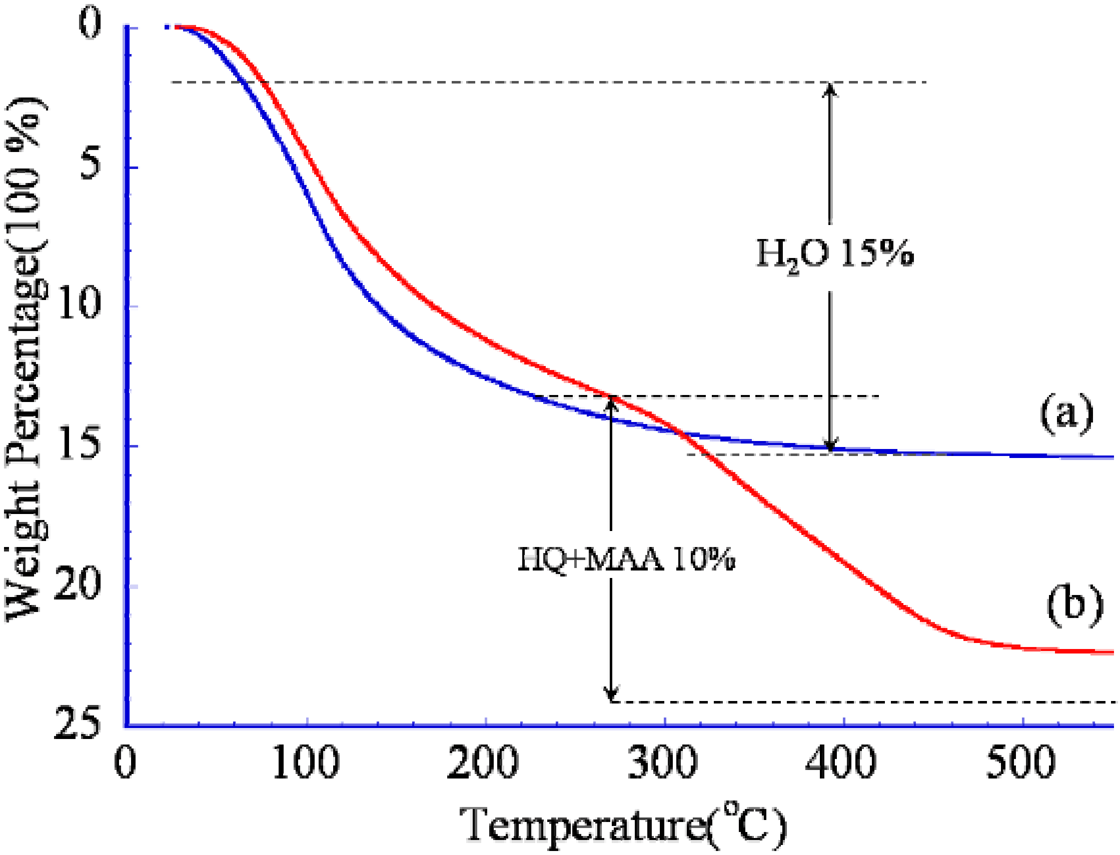

Figure 6.13 TGA curves of (a) as-synthesized Ti-a nanotubes and (b) HQ-Ti-a-70°C.

The amount of incorporated HQ and MAA can be determined quantitatively by TGA measurement. Figure 6.13 shows the TGA curves of as-synthesized Ti-a nanotubes and HQ-Ti-a-70°C. The weight loss of 15% in as-synthesized Ti-a nanotubes from RT to 450°C is attributed to H_2O, in good agreement with a previous study.[10] The water content in HQ-Ti-a-70°C is about 12%. The weight loss of 10% from 270°C to 500°C is caused by losing MAA and HQ. Using the results that the molecular ratio of HQ to MAA is 1:2.3, the content of HQ in HQ-Ti-a-70°C is estimated to be about 5.6%. If the trititanate nanotube ($H_2Ti_3O_7$) model is used to calculate the number of Ti atoms in the Ti-a nanotubes, it suggests that the molecular ratio of HQ to Ti is 6.7:100. As evidenced by the Raman spectra, the majority of the undercoordinated Ti sites are completely reconstructed to the anatase-like structure by the monodentate bonding. There, the molecular ratio of HQ to Ti could be used as an estimation of the content of the undercoordinated Ti site. In other word, 6.7% of Ti sites are undercoordinated in Ti-a nanotubes, lower than suggested in a previous study.[11]

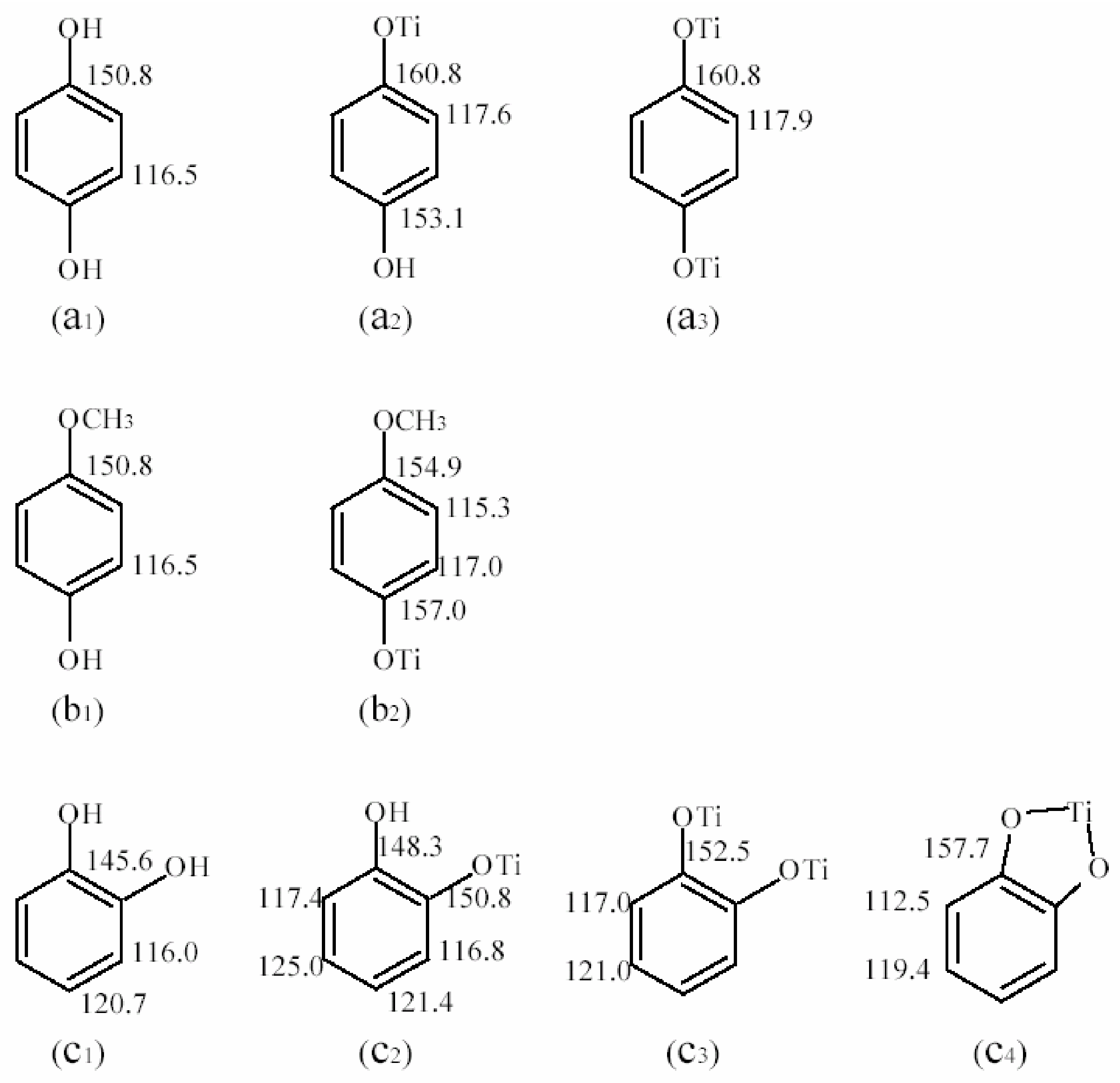

Figure 6.14 Chemical shifts of the ^{13}C nucleus in possible configurations in (a_1) HQ, (a_2), (a_3) HQ anions chemically bonded to Ti, (b_1) MEHQ, (b_2) MEHQ anions chemically bonded to Ti, (c_1) CAT, (c_2), (c_3), (c_4) CAT anions chemically bonded to Ti. The chemical shifts were predicted using the software "CS prediction".

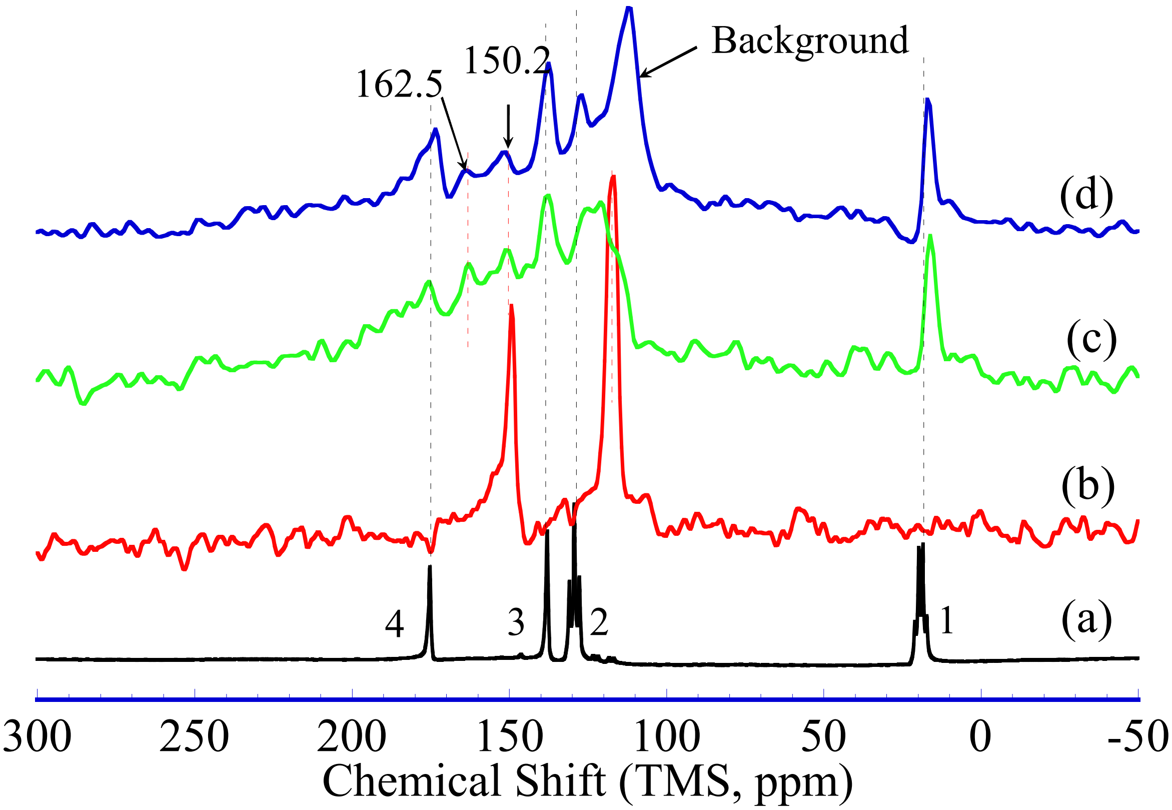

Figure 6.15 ^{13}C NMR spectra of (a) liquid MAA, (b) solid HQ, (c) HQ-Ti-w- 70°C observed via CP, (d) HQ-Ti-w-70°C using direct detection with proton decoupling.

Figure 6.15 shows ^{13}C NMR spectra of liquid MAA, solid HQ and HQ-Ti-w-70°C using decoupling and CP. Similar to that of HQ-Ti-a-70°C, in the spectrum of HQ-Ti-w-70°C sample there are also two peaks originating from ^{13}C associated with the hydroxyl group: one is at 150.2 ppm, corresponding to the ^{13}C connected directly to the hydroxyl group (Fig 6.14 (a_1)); the other peak is shifted to 160.0 ppm, corresponding to the ^{13}C connected to the Ti atom via oxygen (Fig 6.14 (a_2) or (a_3)), the shift difference again agrees with theoretical predictions which suggest that HQ anions are chemically bound to the nanotube surfaces forming a nanotube/HQ hybrid system. The intensities of the two peaks are approximately the same, which suggests that the majority of HQ is chemically bound to the Ti-a nanotube surface by forming the monodentate structure (Fig. 6.14 (a_2)).

6.2.1.5 XRD Pattern

Despite the qualitative changes of the Raman spectra upon HQ treatment, changes in the XRD patterns of Ti-a nanotubes are subtle as shown in Fig. 6.16. So far, there is no consensus with regard to the indexing of the XRD pattern of the nanotubes.

Given the fact that HQ-treated nanotubes show anatase-like Raman spectra, it is tempting to consider the anatase structure as the basis of the nanotube structure. The peak at 2θ=10.2° of the as-synthesized nanotubes, attributed to interlayer interference, corresponds to an interlayer distance of 8.7 Å. The interlayer distance is not affected by HQ treatment.

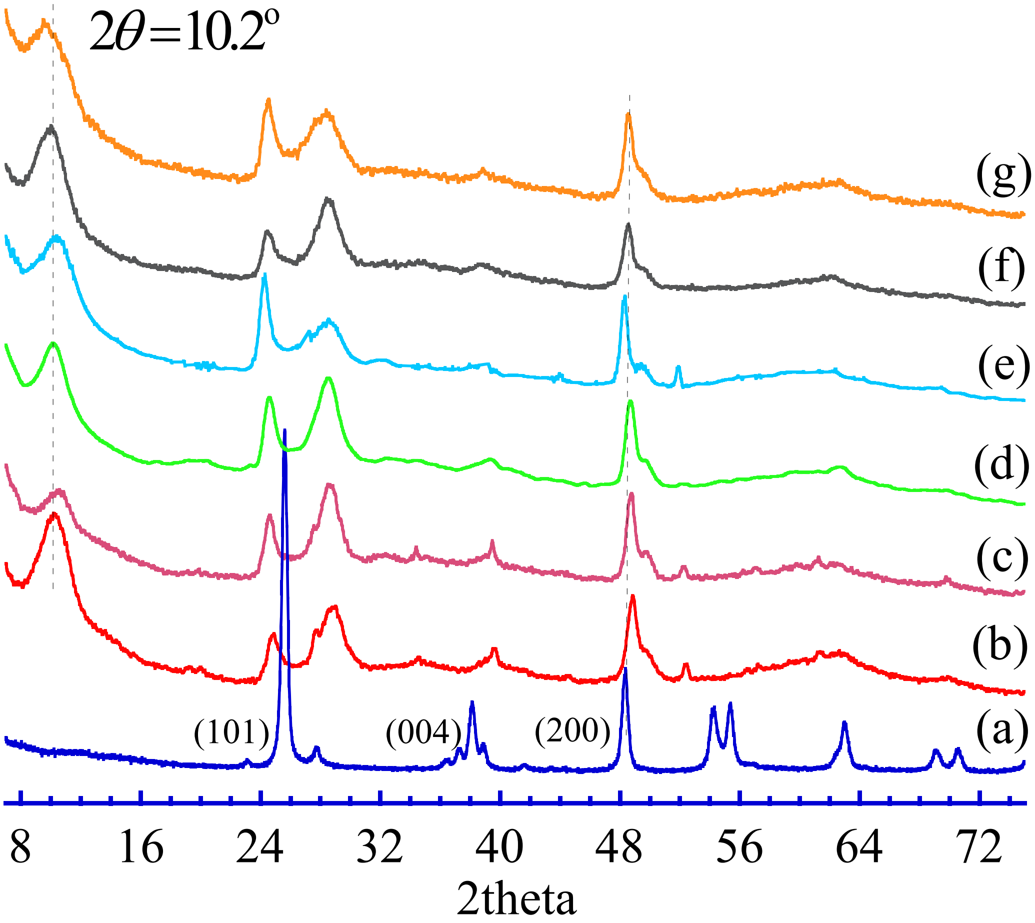

Figure 6.16 XRD patterns of (a) anatase nanocrystals, (b) as-synthesized Ti-a nanotubes, (c) HQ-Ti-a-RT, (d) HQ-Ti-a-70°C, (e) HQ-Ti-a-140°C, (f) as-synthesized Ti-w nanotubes, (g) HQ-Ti-w-140°C.

The XRD pattern of as-synthesized Ti-a nanotubes has two prominent and relatively sharp peaks, as is shown more clearly in Fig. 6.16 (b), one at $2\theta=48.86°$ with a shoulder at $2\theta=49.7°$ and the other at $2\theta=24.81°$. The peak at $2\theta=48.86°$ was previously assigned to anatase (200), which is at $2\theta=48.34°$ in the nanocrystal sample. Previous structural analysis suggests[5] that the sheet that rolls up to form the nanotube is perpendicular to the [010] direction and the axis of the tube is along the [100] direction as illustrated in Fig. 6.17. Since there is no curvature along the [100] direction, the (200) peak is expected to be sharp. The peak at $2\theta=48.62°$ in HQ-treated nanotubes is very close to the (200) peak of anatase TiO_2. This corresponds to a lattice parameter a of 3.74 Å for the anatase unit cell. The peak at $2\theta=40.0°$ in the HQ-Ti-a-140°C resembles the (004) peak of anatase TiO_2. Assigning the $2\theta=40.0°$ peak to (004) would give a lattice parameter c of 9.0 Å for the anatase unit cell. However, the interpretation of the XRD pattern is far more complicated than this. It was suggested previously that the peak at $2\theta=24.81°$ is associated with the (101) peak,[11] which is at $2\theta=25.60°$ in the anatase TiO_2 nanocrystal sample. Figure 6.16 (e) shows that this peak is shifted further to $2\theta=24.45°$ in the HQ-Ti-a-140°C. The assignment of the $2\theta=24.45°$ peak to anatase (101) would lead to an unreasonably large lattice parameter c of over 15 Å. Another intense peak is the broad one at $2\theta=28.7°$ which is present in all nanotube samples. Its interpretation most likely requires diffraction involving interlayer structures. Successful schemes were found to index the major peaks ($2\theta=10.2°$, 24.45°, 28.7°, and 48.62°) based on layered structures of either trititanate $H_2Ti_3O_7$[12] or lepidocrocite titanate $H_xTi_{2-x/4}\square_{x/4}O_4$.[13] However, there are some problems with these indexing schemes also. One is the predicted weakness[12] of the peak at $2\theta=24.45°$ which is quite intense in all nanotube samples. Another problem is why this peak is much sharper than the broad peak at

2θ=28.7°, since under the indexing scheme of titanate structures both peaks should be broadened by the finiteness of the number of layers. It is also unclear how titanate structures can be reconciled with the anatase-like Raman spectra of HQ-treated nanotubes. Further structural modeling is needed to reconcile all this structural information.

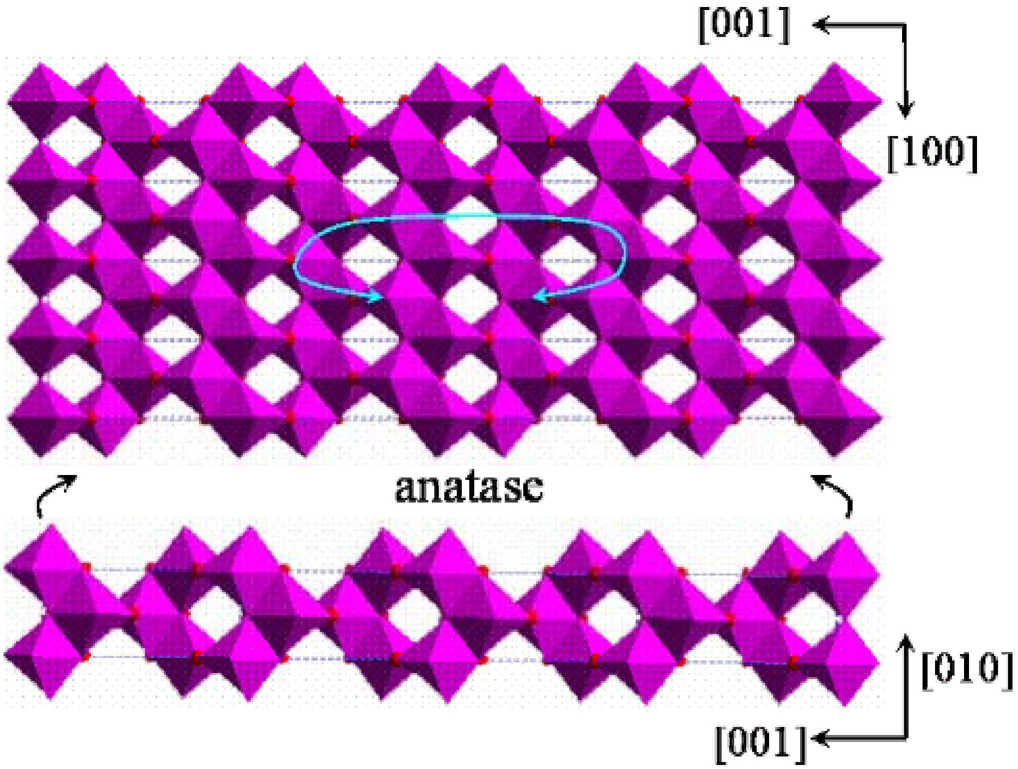

Figure 6.17 Illustration of a possible scheme of tube formation based on the anatase TiO_2 structure.

However, it is clear that significant structural change occurs in the HQ-treated nanotubes upon annealing at 140°C. The ratio of peak heights of the 2θ=24.45° peak versus that of the 2θ=28.7° peak increases substantially upon HQ treatment and 140°C annealing. The peak at 2θ=28.7° is broadened by 140°C annealing. Such changes did not take place in the HQ-treated nanotubes without 140°C annealing. The change of the overall structure contributes significantly to the binding stability of HQ in nanotubes.

The XRD pattern of as-synthesized Ti-w nanotubes and HQ-Ti-w-140°C is shown in Fig 6.16 (f), (g). Similar to the case of the Ti-a nanotubes, changes of the XRD patterns of Ti-w nanotubes are subtle. The ratio of peak heights of the $2\theta=24.45°$ peak versus that of the $2\theta=28.7°$ peak increases substantially upon HQ treatment and 140°C annealing. The peak at $2\theta=28.7°$ is also broadened by 140°C annealing.

6.2.2 Titanate Nanotube/4-Methoxyphenol Hybrid Structure

6.2.2.1 Raman Spectra

Figure 6.18 shows Raman spectra of solid MEHQ, as-synthesized Ti-w nanotubes and MEHQ-Ti-w-70°C. The peaks of solid MEHQ at higher wavenumbers (700~1700 cm^{-1}) were also detected in MEHQ-Ti-w-70°C. The broadening of those peaks in MEHQ-Ti-w-70°C indicates the formation of bonding between MEHQ molecules and nanotube surfaces, leading to the yellowish color of MEHQ treated nanotubes as shown in Fig. 6.5 (b’). The mechanism of the color change could be similar to that induced by HQ bonding (Section 6.2.1.2). The red shift is due to the formation of Ti-O bonds between MEHQ and nanotubes at the defect site. The excitation occurs from a molecular orbital primarily associated with MEHQ carbon atoms, to a molecular orbital delocalized on some of the titanium atoms and corresponds to charge transfer from MEHQ molecules to the nanotubes. The smaller red shift compared to HQ treatment indicates that the bonding of MEHQ with nanotubes is weaker than HQ. Raman peaks of MEHQ at lower wavenumbers (120~700cm^{-1}) were not observed in MEHQ-Ti-w-70°C, which might be because the peaks are greatly broadened and overlapping with Ti-w peaks. Also, the number of MEHQ could also be small, which is confirmed by NMR as will be discussed later. The positions of the three dominant peaks of Ti-w nanotubes are not affected by MEHQ treatment, which indicates the relatively weak bonding between MEHQ molecules and Ti-w nanotubes. However, the intensity ratios of the peaks at 270 cm^{-1} and 450 cm^{-1} with respect to the peak at 710 cm^{-1} are decreased compared to as synthesized Ti-w nanotubes. There is thus subtle local structure change in the nanotubes induced by MEHQ ligands monodentate bonding.

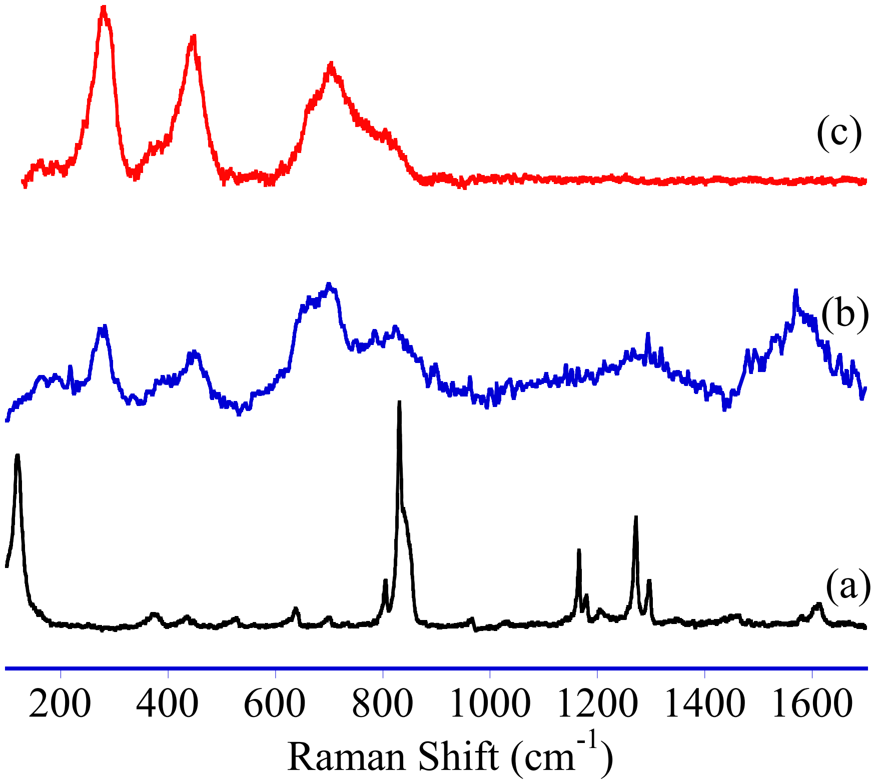

Figure 6.18 Raman spectra of (a) solid MEHQ, (b) MEHQ-Ti-w-70°C, (c) as-synthesized Ti-w nanotubes.

Similar as HQ-treated Ti-a nanotubes, the Raman spectra of MEHQ-Ti-a-70°C are also nearly identical to anatase TiO_2 (Fig. 6.19) unlike MEHQ-Ti-w-70°C described above. As shown in Fig. 6.1 (c), MEHQ has only one hydroxyl group, indicating it can only binds to Ti site by forming the monodentate structure. The anatase-like Raman spectrum of MEHQ-Ti-a-70°C shows that monodentate bonding is effective in inducing the dramatic change to anatase-like Raman spectrum. At higher wavenumbers (770~1700 cm^{-1}) faint and broadened Raman peaks representing solid MEHQ were observed in the spectrum of MEHQ-Ti-a-70°C (Fig. 6.19 (d)). The broadening of the peaks indicates the formation of bonding between MEHQ and Ti-a nanotubes. The Raman peaks of MEHQ at lower wavenumbers (120~770 cm^{-1}) were not observed in MEHQ-Ti-a-70°C, and it may be because the peaks are greatly broadened.

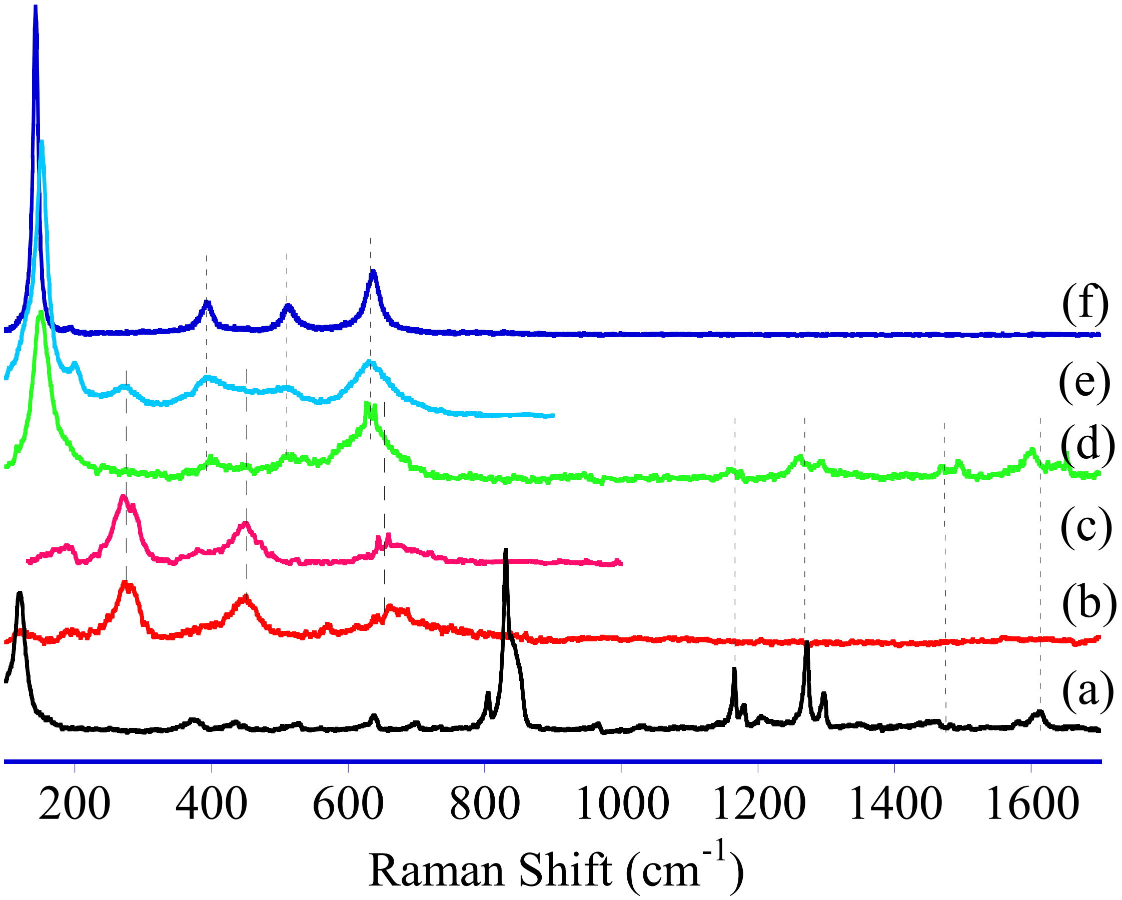

Figure 6.19 Raman spectra of (a) solid MEHQ, (b) as-synthesized Ti-a nanotubes, (c) MEHQ-Ti-a-140°C soaked in H_2O for 4 days, (d) MEHQ-Ti-a-70°C, (e) MEHQ-Ti-a-140°C, (f) anatase TiO_2 nanocrystals.

Since the Raman spectrum of MEHQ-treated nanotubes can be attributed completely to anatase-like local structures, it suggests that most of undercoordinated Ti atoms are removed by MEHQ treatment, including the majority of sites which can be accessed only through diffusion in-between the layers. Different from HQ, MEHQ has only one hydroxyl group. Therefore, MEHQ could react with one of the undercoordinated Ti atoms in the outer, inner surfaces and interlayer region of the nanotubes by forming a monodentate structure, which effectively induces the dramatic local structure reconstruction to the anatase-like structure.

As to the stability in an aqueous environment, the Raman spectrum of MEHQ-Ti-a-140°C soaked in water for 4 days returns to that of as-synthesized nanotubes, as shown in Fig 6.19 (c). The third Raman peak tends to shift to larger wavenumbers as well, but not as much as in HQ-Ti-a-140°C. It might be because the soaking period of MEHQ-Ti-a-140°C (4 days) was shorter than that of HQ-Ti-a-140°C (7 days). It indicates that the monodentate ligand MEHQ did not bind stably with the Ti-a nanotube surface. Even with annealing, MEHQ induced changes to the anatase-like local structures are also not sufficient to stabilize the nanotube/MEHQ hybrid structure in an aqueous environment.

Combining the results of HQ- and MEHQ-treated Ti-a nanotubes, it is clear that the monodentate bonding is capable of inducing a local structure reconstruction of Ti-a nanotubes to the anatase-like structure; while bidentate binding, along with annealing, is necessary to stabilize the Ti-a nanotube/HQ hybrid structure and maintain the anatase-like local structure. Eventually, this leads to the idea that the majority of HQ molecules are bonded to the Ti-a nanotube surface by the monodentate bonding (as indicated in Fig 6.10), and the minority of them form the bidentate bonding. Both the monodentate and the bidentate contribute to inducing the anatase-like local structure, but only the bidentate bonding can stabilize the hybrid structure in the aqueous conditions. The quantitative determination of the ratio of the monodentate- to the bidentate- bonded HQ molecules is difficult. Solid-state ^{13}C NMR was performed in an attempt to solve this issue, but because of the insufficient resolution in chemical shift, signals from these two origins (mono- and bidentate bondings) were not resolved. Further investigation is needed to clarify this point.

6.2.2.2 NMR Spectra

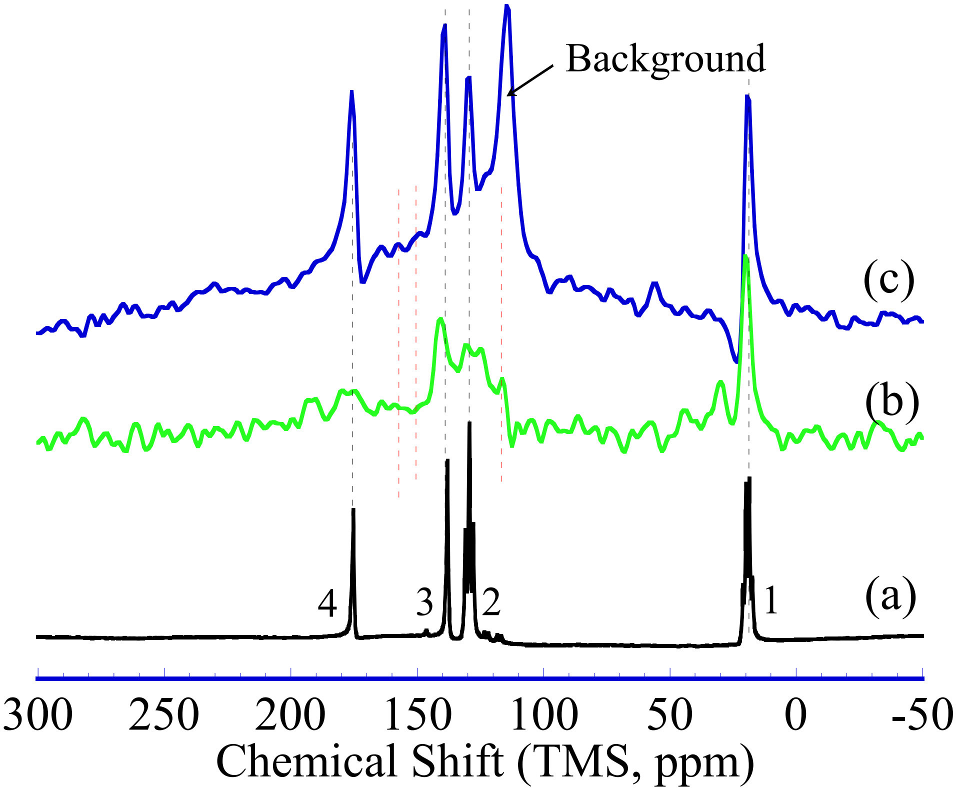

Figure 6.20 ^{13}C NMR spectra of (a) liquid MAA, (b) MEHQ-Ti-w-70°C using CP, (c) MEHQ-Ti-w-70°C using decoupling.

Figure 6.20 shows the ^{13}C NMR spectra of liquid MAA, and MEHQ-treated Ti-a nanotubes obtained using decoupling and CP. The peak assignments of the MAA spectrum are the same as shown in Fig. 6.12. The spectra only show the ^{13}C signals from liquid MAA.

The ^{13}C NMR signals originating from MEHQ molecules are unobservable (recent high-field data show the presence of small amount MEHQ). It indicates that the amount of bonded MEHQ molecule is much less than that of HQ in HQ-treated Ti-a nanotubes per unit gram, but it is still sufficient to induce surface reconstruction from the as-synthesized nanotube structure to the anatase-like local structure.

6.2.2.3 XRD Spectra

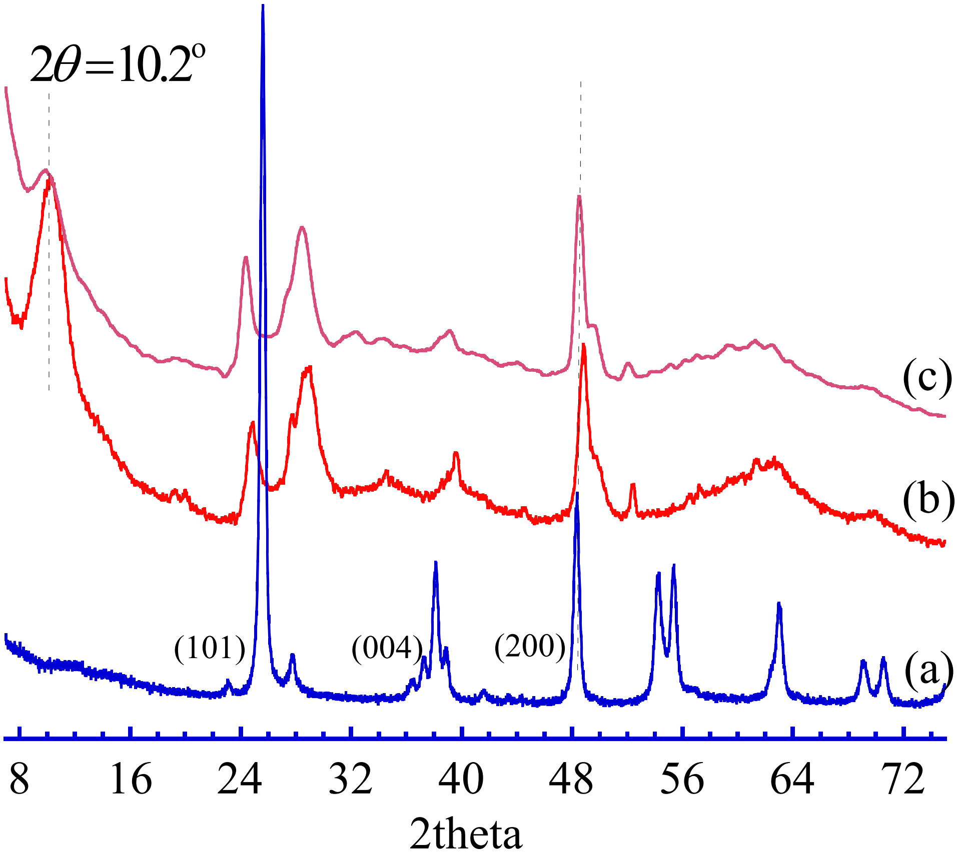

Figure 6.21 XRD patterns of (a) anatase nanocrystals, (b) as-synthesized Ti-a nanotubes, (c) MEHQ-Ti-a-140°C.

As expected, despite the qualitative change of the Raman spectrum upon MEHQ treatment, changes in the XRD patterns of Ti-a nanotubes are subtle as shown in Fig. 6.21. The interlayer distance is not affected by MEHQ treatment. Upon MEHQ treatment and annealing at 140°C, the ratio of peak heights of the $2\theta=24.45^\circ$ peak versus that of the

$2\theta=28.7°$ peak remains unchanged, unlike HQ treated nanotubes annealed at 140°C. Also, no noticeable broadening of the peak at $2\theta=28.7°$ in MEHQ-Ti-a-140°C pattern is observed. The weaker bonding of MEHQ with nanotubes compared to HQ and the small amount of incorporated MEHQ could be the reasons for the minor changes in XRD.

6.2.3 Titanate Nanotube/Catechol Hybrid Structure

Catechol has been suggested to be able to bind to TiO_2 surfaces through the bidentate bonding configuration (see Section 5.5.2 for details). We use this molecule to explore the effect of bidentate bonding to the titanate nanotube structure.

6.2.3.1 Raman Spectra

Figure 6.22 shows Raman spectra of solid CAT, as-synthesized Ti-w nanotubes and CAT-Ti-w-70°C. The assignments of solid CAT peaks are shown in Table 6.1.[14] Those peaks of solid CAT at higher wavenumbers (1110~1700 cm^{-1}) were also detected in CAT-Ti-w-70°C. The peak at 1160 cm^{-1}, which is assigned to the B_2 mode of O-H bonds, is completely missing, strongly indicating that CAT molecules attaches to the nanotube surfaces via hydroxyl groups. The broadening of those peaks in CAT treated Ti-w nanotubes also indicates the formation of bonds between CAT molecules and the nanotube surface, leading to the dark reddish color of CAT-treated nanotubes as shown in Fig. 6.5 (d'). The mechanism of the color change could be similar to that induced by HQ bonding (Section 6.2.1.2). The red shift is due to the formation of Ti-O bonds between CAT and nanotubes at the defect sites. The molecular orbital primarily associated with CAT carbon atoms is somewhat delocalized on some of the titanium atoms and corresponds to charge transfer from CAT molecules to the titanate nanotubes. The Raman peaks of CAT at lower wavenumbers (120~1110 cm^{-1}) were not observed in CAT-Ti-w-70°C, and it may be because the peaks are greatly broadened. The positions of the three dominant peaks of Ti-w nanotubes are not affected by CAT treatment. However, in CAT-Ti-w-70°C spectrum, both the intensities of the peaks at 270 cm^{-1} and 450 cm^{-1} with respect to the peak at 710 cm^{-1} are decreased compared to as-synthesized Ti-w nanotubes, which is a reflection of subtle local structure changes of nanotubes induced by CAT ligands bonding.

Table 6.1. Experimental Vibrational Frequencies for Catechol Shifts.[14]

ν / cm^{-1}	1597	1514	1271	1160	1040	773
assignment	$\gamma CC + \gamma CO, B_2$	$\gamma CC + \delta CH, B_2$	$\gamma CC, A_1, 7a$	$\gamma CH, A_1$ $\gamma OH, B_1$	$\gamma CH, A_1$	ring,A_1

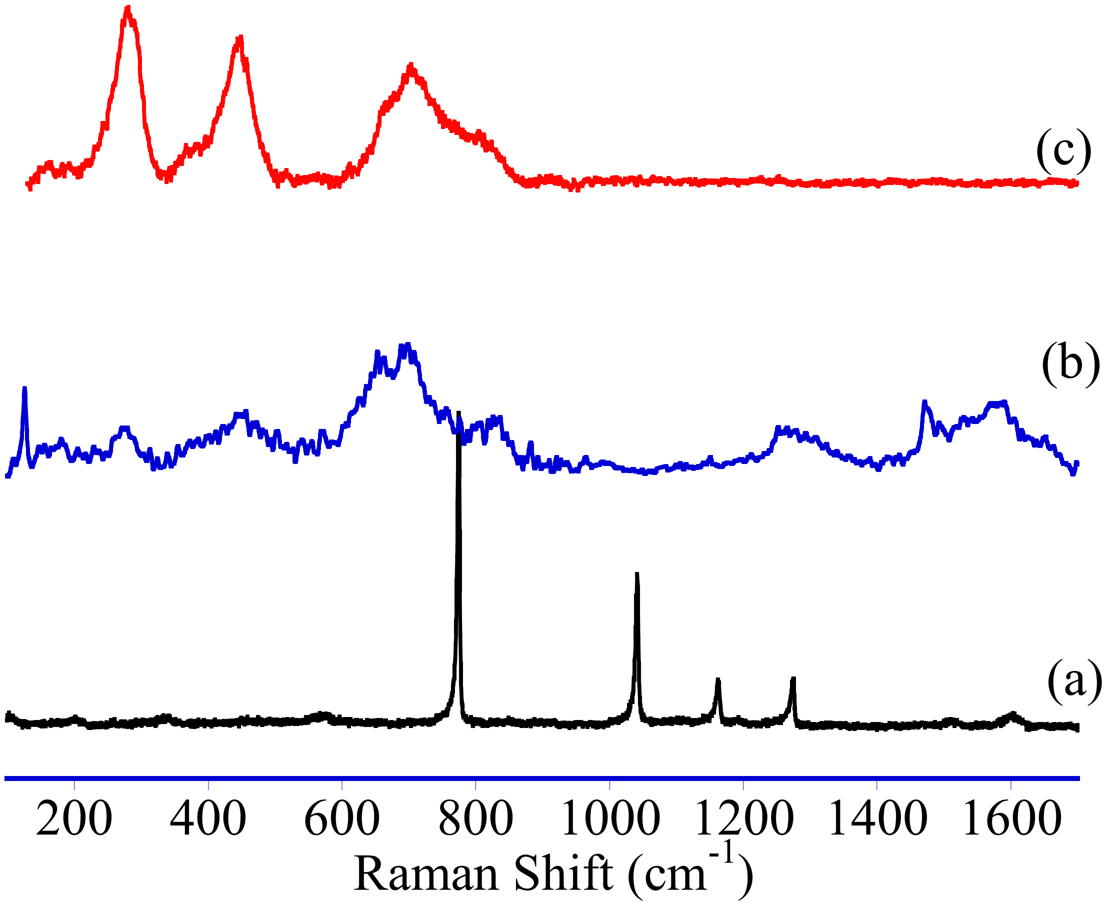

Figure 6.22 Raman spectra of (a) solid CAT, (b) CAT-Ti-w-70°C, (c) as-synthesized Ti-w nanotubes.

As expected, the Raman spectra of CAT-Ti-a-70°C are also nearly identical to that of anatase TiO_2 (Fig. 6.23) in contrast to CAT-Ti-w-70°C. The CAT treatment also induces a dark reddish color (Fig 6.5 (d)). Those solid CAT Raman peaks at higher wavenumbers (1110~1700 cm^{-1}) were observed in the spectrum of CAT-Ti-a-70°C, and the broadening of the peaks indicates the formation of bondings between CAT and Ti-a nanotubes. The peak at 1160 cm^{-1} which is assigned to B_2 mode of O-H bonds is completely missing, strongly indicating that CAT molecule attaches to the nanotube surface via hydroxyl groups. The Raman peaks of CAT at lower wavenumbers (120~1110 cm^{-1}) were not observed in CAT-Ti-a-70°C, and it may be because the peaks are greatly broadened.

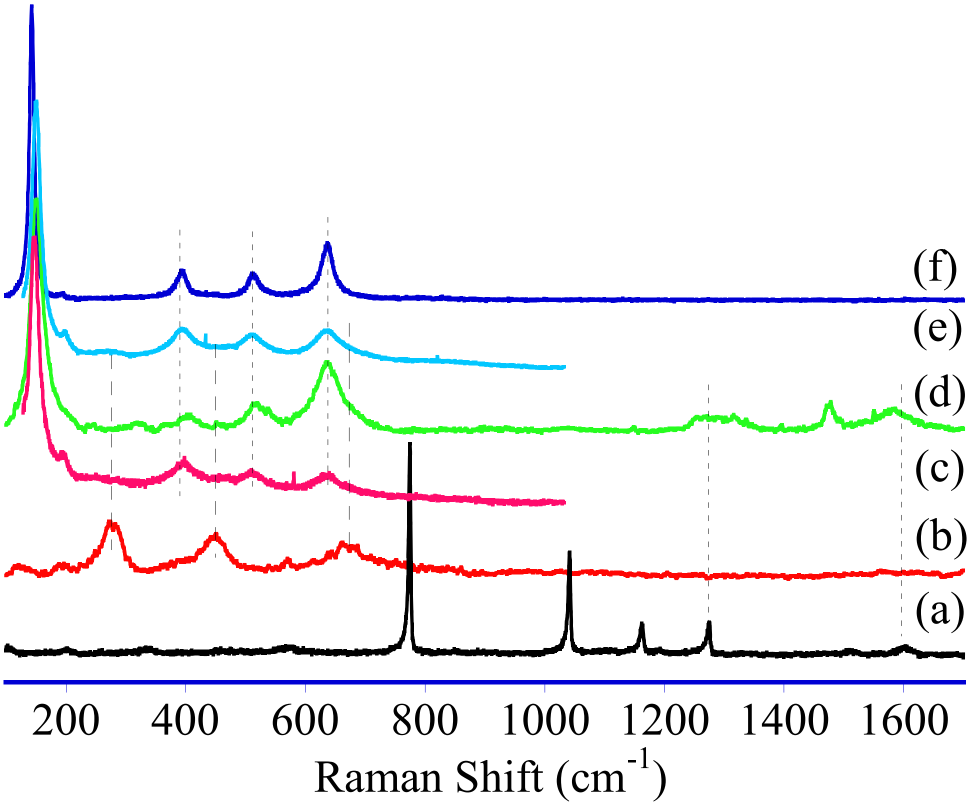

Figure 6.23 Raman spectra of (a) solid CAT, (b) as-synthesized Ti-a nanotubes, (c) CAT-Ti-a-70°C soaked in H_2O for 4 days, (d) CAT-Ti-a-70°C, (e) CAT-Ti-a-140°C, (f) anatase TiO_2 nanocrystals.

The change of the Raman spectrum upon CAT treatment indicates that defects and undercoordinated Ti atoms in nanotubes were restored to anatase-like local structures, including those in interlayer region. There are three possible kinds of bonding configurations for a CAT molecule with Ti sites: monodentate (Fig. 6.14 (c_2)) and two possible bidentate structures (Fig. 6.14 (c_3) and (c_4)). Owing to its unique molecular structure, as shown in Fig 6.1, both hydroxyl groups of CAT could react with Ti defect sites, not only in the interlayer region, but also in the inner and outer surfaces.

As to the stability in an aqueous environment, the Raman spectrum of CAT-Ti-a-140°C soaked in water for 4 days remains anatase-like. It indicates that a sufficient number of CAT molecules bind to Ti-a nanotubes by forming a bidentate structure. The bidentate bonding, along with annealing at 140°C, is able to stabilize the Ti-a nanotube/CAT hybrid structure and maintain the anatase-like local structure in aqueous environment. Structural relaxation at the binding site induced by 140°C annealing is most likely responsible for the stability.

6.2.3.2 NMR Spectra

Figure 6.24 shows ^{13}C NMR spectra of liquid MAA, and CAT-Ti-w-70°C using decoupling and CP. The peak assignments of the MAA spectrum are the same as those shown in Fig. 6.11. In the CAT-Ti-w-70°C spectrum, the peak at 157.2 ppm originates mainly from the ^{13}C nuclei connected directly to hydroxyl groups with the configuration indicated in Fig. 6.14 (c_4). The ^{13}C nucleus with the configuration shown in Fig. 6.14 (c3) could also contribute to the 157.2 ppm peak. The peak at 121.0 ppm corresponds to the rest of the ^{13}C nuclei in the aromatic ring. There is no peak observed at 145.6 and 148.3 ppm, which indicates that there is no or very little CAT in the CAT-Ti-w-70°C with the figurations shown in Fig. 6.14 (c_2) and (c_3). Thus, for CAT, the most favorable bonding is to form a bidentate structure via both hydroxyl groups to one Ti atom (Fig. 6.14 (c_4)). Possibly, part of the 157.2 ppm peak could be associated with another form of bidentate structure--the two hydroxyl groups bind to two different adjacent Ti atoms (Fig. 6.14 (c_4)). Compared to HQ- and MEHQ-treated Ti-a nanotubes, the intensity of the CAT treated nanotube ^{13}C signal is stronger relative to the background peak, which shows that more CAT molecules could react with nanotubes per unit gram than HQ or MEHQ.

Figure 6.25 shows ^{13}C NMR spectra of liquid MAA, and CAT-Ti-a-70°C using decoupling and CP. Similar to CAT treated Ti-w nanotubes, in CAT treated Ti-a nanotubes, CAT also favors the configuration shown in Fig. 6.14 (c_4), forming a bidentate structure via both hydroxyl groups.

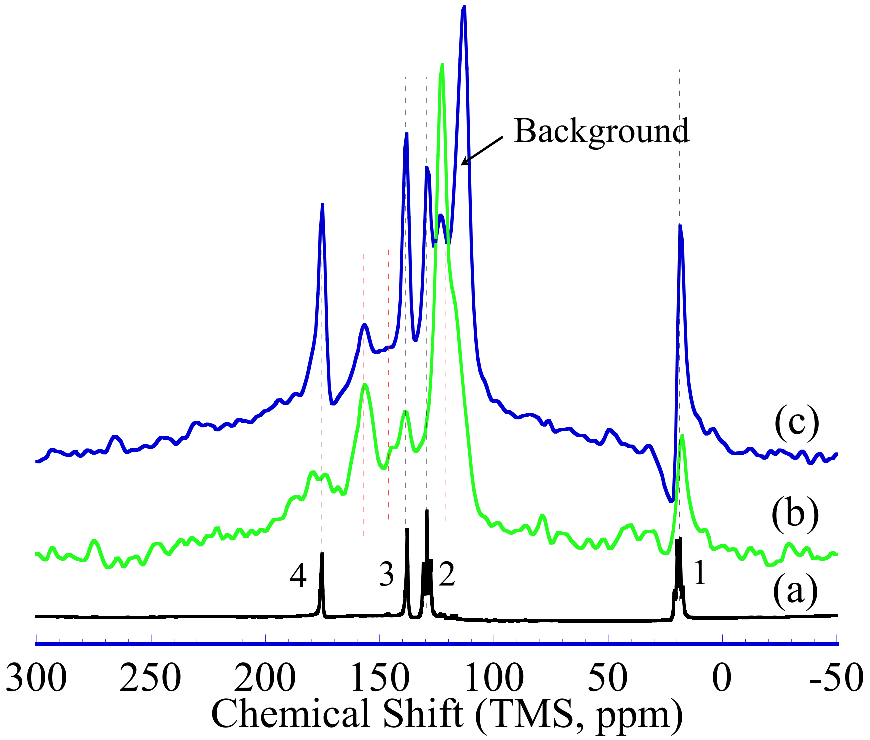

Figure 6.24 ^{13}C NMR spectra of (a) liquid MAA, (b) CAT-Ti-w-70°C using CP, (c) CAT-Ti-w-70°C using decoupling.

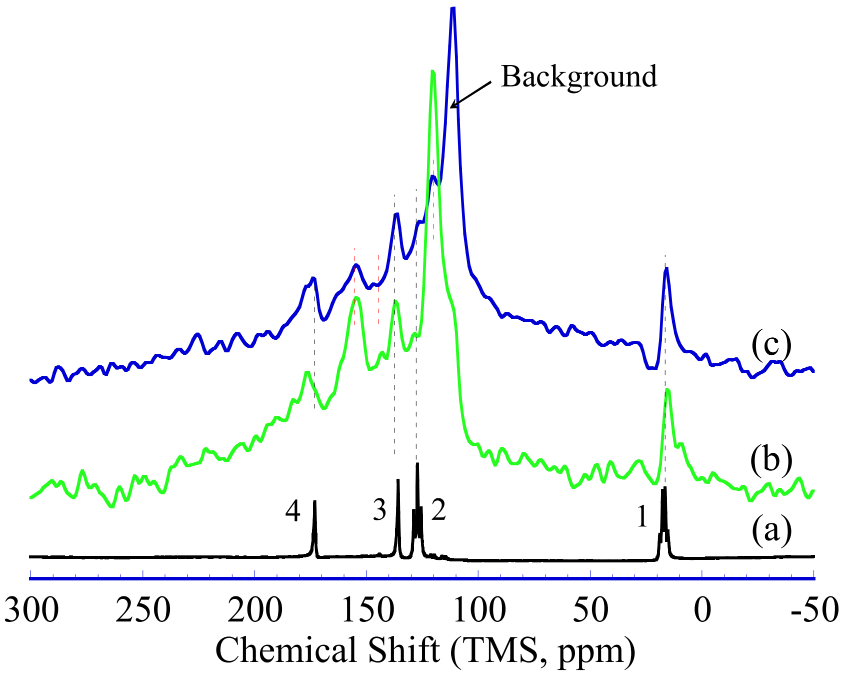

Figure 6.25 ^{13}C NMR spectra of (a) liquid MAA, (b) CAT-Ti-a-70°C using CP, (c) CAT-Ti-a-70°C using decoupling..

6.2.3.3 XRD Spectra

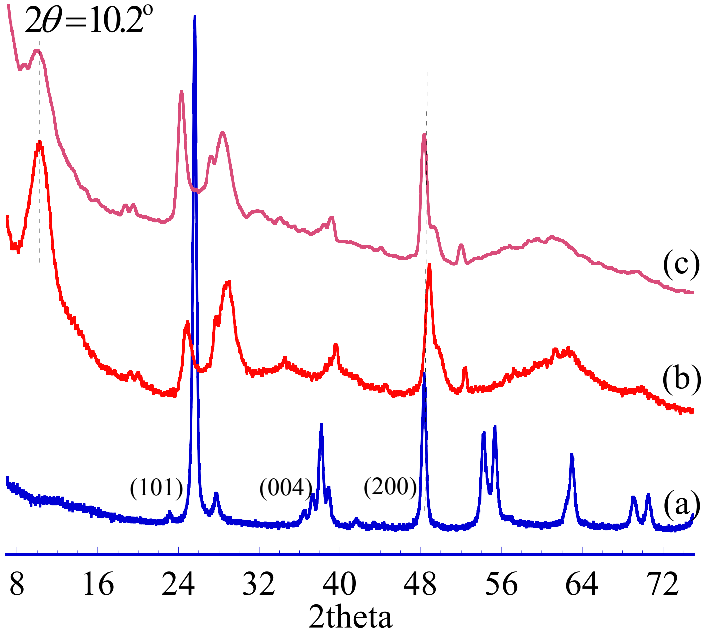

Figure 6.26 XRD patterns of (a) anatase nanocrystals, (b) as-synthesized Ti-a nanotubes, (c) CAT-Ti-a-140°C.

Similar to the case of HQ- and MEHQ-treated Ti-a nanotubes, despite the qualitative change of the Raman spectrum upon CAT treatment, changes in the XRD patterns of Ti-a nanotubes are subtle. The interlayer distance is not affected by CAT treatment. Upon CAT treatment and annealing at 140°C, the ratio of peak heights of the 2θ=24.45° peak versus that of the 2θ=28.7° peak increases substantially. It is consistent with the argument that the changes of the peaks at 2θ=24.45° and 28.7° upon annealing are indications of the change of the overall structure, which contributes significantly to the binding stability of CAT in nanotubes.

In this study, the hybrid structures of titanate nanotube and organic molecules, such as, hydroquinone (HQ), catechol (CAT) and 4-methoxyphenol (MEHQ), were successfully synthesized. The optical and structural properties are characterized by UV-vis, Raman scattering, X-ray diffraction and ^{13}C NMR, etc. It is found that by forming bidentate structure, organic molecules (hydroquinone and catechol) and titanate nanotubes can form hybrid structures which are relatively stable in an aqueous environment. Also, it was demonstrated that the local structure of acid-washed nanotubes can be changed reversibly into an anatase-like structure by the incorporation of organic molecules. Water-washed nanotubes do not show such structural changes to an anatase-like structure upon HQ, MEHQ, and CAT adsorption. There are significant differences in local structures and defects between water-washed and acid-washed samples. This provides important clues for understanding the structure of nanotubes and the interaction between ligands and nanotube surfaces. The hybrid system of titanate nanotubes/organic molecules has optical absorption significantly beyond 700 nm. This system could have very important applications in photocatalysis and photovoltaic devices. The results were published in *Journal of Nanoscience and Nanotechnology,* **7** 458 (2007).

6.3 References

1. C. R. Rice, M.D.Ward., M. K. Nazeeruddin and M. Gratzel, *New J. Chem*., **24**, 651 (2000).
2. P. C. Redfern, P. Zapol, L. A. Curtiss, T. Rajh, and M. C.Thurnauer, *J. Phys. Chem. B*, **107,** 11419 (2003).
3. A. Kleinhammes, G. W. Wagner., H. Kulkarni, Y. Jia, Q. Zhang, L. -C. Qin, and Y. Wu, *Chem. Phys. Lett.*, **411,** 81 (2005).
4. D. V. Bavykin, J. M. Friedrich, Frank C. Walsh, *Adv. Mater*, **18**, 2807 (2006).
5. B. D. Yao, Y. F. Chan., X. Y. Zhang, W. F. Zhang, Z. Y. Yang, and N. Wang, *Appl. Phys. Lett*, **82,** 281 (2003).
6. T. Ohsaka, F. Izumi, and Y. Fujiki, *J. Raman Spectrosc.*, **7,** 321 (1978).
7. G. Cangiani, *AB-initio study of the properties of TiO2 rutile and anatase polytypes. Ph.D dissertation.* University of Trieste, Italy, 63 (2003).
8. H. M. Kim, F. Miyaji, T. Kokubo, *J. Mater. Sci. Mater Med*, **8,** 341 (1997).
9. T. Kasuga, M. Hiramatsu, A. Hoson, T. Sekino, and K. Niihara, *Adv. Mater*, **11,** 1307 (1999).
10. R. Ma, Y. Bando, and T. Sasaki, *Chem. Phys. Lett.*, **380**, 577 (2003).
11. Z. V. Saponjic, N. M. Dimitrijevic, D. M. Tiede, A. J. Goshe, X. Zuo, L. X. Chen, A. S. Barnard, P. Zapol, L. Curtiss, T. Rajh, *Adv. Mater*., **17,** 965 (2005).
12. Q. Chen, G. H. Du., S. Zhang, L. -M. Peng, *Acta Crystallographica Section B*, **58,** 587(2002).
13. R. Ma, Y. Bando, and T. Sasaki, *Chem. Phys. Lett.*, **380**, 577 (2003).
14. L. Ohrstrom,and I. Michaud-Soret, *J. Phys.Chem. A,* **103,** 256 (1999).

CHAPTER 7

CONCLUSIONS

In this dissertation I report the structure and property characterization of two kinds of materials on the micro- and nano-scale level, the self-healing polymer Surlyn® and a titanate nanotube/organic molecule hybrid. Multiple techniques have been utilized to study the structural, dynamic, thermal, and optical properties of the materials.

In the first study, the thermal, structural, and dynamic properties of the self-healing polymer Surlyn® (poly(ethylene-*co*-methacrylic acid) polymer neutralized with Na^+) were investigated. By introducing a suitable cation, Na^+ e.g., Surlyn® possesses unique mechanical, rheological and thermal properties, as well as the intriguing property of self-healing with potential applications in protecting space vehicles from destructive micrometeorite impacts. Understanding the role of the cations in the material, the chemical structure and the physical properties of the polymer is crucial for potential applications. The previous studies on structural properties are mainly based on small angle X-ray scattering (SAXS) data. In my study, the experimental results of thermal properties obtained by differential scanning calorimetry (DSC) and microscopic structures obtained by nuclear magnetic resonance (NMR) are discussed. It is found that although thermal properties change significantly, the structure and dynamics of ionic aggregates (consists of Na^+-O^- pairs) remain unchanged under aging and mechanical deformation. The distance between Na^+ ions was also estimated.

In the second study titanate nanotubes were successfully synthesized. Titanate nanotubes combine the properties and applications of conventional TiO_2 nanoparticles (e.g. photocatalysis, wide band gap) with the properties of layered titanates (e.g. ion exchange). However, its wide band gap, 3.7 eV, limits the solar conversion efficiency in photovoltaic applications. It was reported that 40 % of Ti atoms in such nanotubes are undercoordinated, which could present problems for electron transport. Surface modification, e.g. attachment of charge-transfer ligands, is one of the most effective approaches to modify the optical absorption spectrum and restore the sixfold coordination of Ti sites. Understanding the microstructure of titanate nanotubes and their properties is of great importance in order to predict, control and direct the surface modification process. However, up to now, the structure and the formation mechanism of titanate nanotubes have not been clarified. Previous studies show that the undercoordinated Ti sites present on the surface of small TiO_2 nanoparticles are very reactive and can absorb certain molecules such as catechol, leading to a large optical red shift of about 1.6 eV. The different bonding configurations of catechol on nanoparticle surfaces (e.g. monodentate and bidentate structures) lead to different binding energies, and may induce different structural changes in TiO_2 nanoparticles. Similar to TiO_2 nanoparticles, our results show that when titanate nanotubes are exposed to organic molecules, e.g. catechol, their color changes along with changes of local structures. In order to study the mechanisms of the different bonding configurations and the induced structure changes experimentally, three different molecules, hydroquinone, 4-methoxypenol(MEHQ) and catechol were chosen. Each of these three molecules is expected to form a different bonding configuration. The optical and structural properties of titanate nanotubes and the three hybrid structures (titanate nanotube/hydroquinone, titanate nanotube/MEHQ and titanate nanotube/catechol) were characterized by multiple techniques, such as UV-vis, Raman spectroscopy, X-ray diffraction and NMR spectroscopy, etc. Through comparing the results of the three hybrid structures, it is found that by forming bidentate structure, organic molecules (hydroquinone and catechol) and titanate nanotubes can form hybrid structures which are relatively stable in an aqueous environment. Also, it was demonstrated that there are significant differences in local structures between water-washed and acid-washed titanate nanotubes. For acid-washed nanotubes, the local structure can be changed reversibly into an anatase-like structure by the incorporation of HQ, MEHQ, or CAT. This provides important clues for understanding the structure of titanate nanotubes and the interaction between ligands and nanotube surfaces. The hybrid system of titanate nanotubes/organic molecules has optical absorption significantly beyond 700 nm. This system could have very important applications in photocatalysis and photovoltaic devices.

Although the structure, the formation mechanism and the properties of titanate nanotubes have been studied systematically, still much remains to be learned. Earlier studies suggested that the structure of the nanotubes was titania nanotubes, either anatase phase or anatase-rutile phase. Recently, some researchers claimed that the tubular material is titanate nanotubes, e.g. $H_2Ti_3O_7$, rather than titania nanotubes. Based on the Raman spectra, our results show the structure of titanate nanotubes is closely related to anatase titania. A structural model of the titanate nanotubes is of great importance for the property modification and characterization, as well as other applications.

As shown in our studies, oxygen-rich molecules such as HQ and catechol are very good candidates to modify the optical properties and the structure of titanate nanotubes. However, for the further applications in photocatalysis, more effort is needed to improve the stability in the aqueous environment. Understanding the mechanism of the binding between the organic molecules and titanate nanotubes is of great importance. Apparently, Raman spectroscopy is a powerful tool to monitor the changes of local structure of titanate nanotubes. Thus, it is urgent to assign the Raman peaks of the titanate nanotubes.

There are still several unanswered questions. Do other factors, such as the mobility of the molecules, also play important roles in the property and structural changes? Are there any other molecules more effective at inducing the property and structural changes, and making the hybrid structure stable in the aqueous environment? How one can quantify the amount of the attached molecules and the undercoordinated Ti sites? And the most basic and important question: what is the exact structure of the titanate nanotubes? Other applications, such as photocatalysis, and titanate nanotubes as a fuel-cell electrode, also require urgent development.

APPENDIX

SOLID STATE NMR WITH ENHANCE RESOLUTION AND SENSITIVITY

In powdered solids, the presence of anisotropic interactions leads to broad lines in the NMR spectra, as the different molecular orientations give rise to different resonance frequencies. If the anisotropy of the coupling exceeds the chemical shift the lines will overlap and the chemical shift resolution is lost. In addition to this, dipolar couplings between abundant nuclei (e.g. protons) broaden the lines dramatically and lead to spectra that basically consist of one large ‘hump’. In liquids, the fast isotropic tumbling of the molecules averages the anisotropic interactions to zero and no such substantial line broadening is observed. Thus, it would be desirable to mimic this motion to get spectral resolution in solid samples.

One method for achieving high-resolution NMR is to artificially narrow NMR lines in solids, by physically spinning the sample in a specific way to eliminate the broadening. This is known as magic angle spinning (MAS). In the presence of abundant spins, it may be possible to obtain a high resolution (i.e. without dipolar broadening) spectrum of low-abundance spins, such as naturally abundant ^{13}C, by simply decoupling the abundant spins in analogy to solution NMR. Under certain conditions, cross polarization (CP) to transfer polarization from ^{1}H nuclei can help the sensitivity greatly.

In the following few sections, some methods to achieve high resolution or signal sensitivity, such as MAS, heteronuclear decoupling and cross polarization, will be discussed. Unless explicitly mentioned, the content discussed in this chapter is derived from the book authored by Slichter.[1]

1 Magic Angle Spinning

In liquids, isotropy and rapid tumbling average out interactions such as the direct dipolar coupling and the chemical shift anisotropy by a phenomenon called motional narrowing. In solids, these interactions are usually not completely averaged out owing either to the absence of molecular tumbling and diffusion, or to their insufficiency for complete motional narrowing.

As mentioned, the dipolar interaction between two magnetic moments $\vec{\mu}_i = \gamma_i \hbar \vec{I}_i$ and $\vec{\mu}_j = \gamma_j \hbar \vec{I}_j$ can be written as:

$$\mathcal{H}_{ij} = \frac{\gamma_i \gamma_j \hbar^2}{r_{ij}^3} \{\vec{I}_i \vec{I}_j - 3\frac{(\vec{I}_i \cdot r_{ij})(\vec{I}_j \cdot r_{ij})}{r_{ij}^2}\} \tag{1}$$

The general dipolar contribution to the Hamiltonian for N spins then becomes

$$\mathcal{H}_d = \frac{1}{2}\sum_{i=1}^{N}\sum_{j=1}^{N}\frac{\gamma_i \gamma_j \hbar^2}{r_{ij}^3} \{\vec{I}_i \vec{I}_j - 3\frac{(\vec{I}_i \cdot r_{ij})(\vec{I}_j \cdot r_{ij})}{r_{ij}^2}\} \tag{2}$$

If we define θ as the angle between the external field B_0 and the internuclear vector from $\vec{I}_i$ to $\vec{I}_j$, the total Hamiltonian could be simplified by dropping higher order terms

$$\mathcal{H}_d^0 = \frac{1}{4}\sum_{i,j}\frac{\gamma_i \gamma_j \hbar^2}{r_{ij}^3}\frac{(1-3\cos^2\theta_{ij})}{r_{i,j}^3}(3I_{iz}I_{jz} - \vec{I}_i \cdot \vec{I}_j) \tag{3}$$

The effect of rotation may be expressed very simply in terms of the angles defined in Fig 1. We consider a pair of nuclei i, j fixed in a molecule, the axis of rotation of the molecule making an angle θ' with respect to the static field B_0. Let the internuclear vector from i to j make an angle γ_{ij} with the rotation axis. Then, as the molecule rotates, the angle θ_{ij} varies with time. Since the frequencies of rotation are high compared with the frequencies of interest in the resonance, it is the time average of $1-3\cos^2\theta_{ij}$ that affects H_d^0. This average can be shown to be independent of the details of the motion, and

$$\left\langle 1-3\cos^2\theta_{ij}\right\rangle_{avg} = (1-3\cos^2\theta')\frac{(3\cos^2\gamma_{ij}-1)}{2} \tag{4}$$

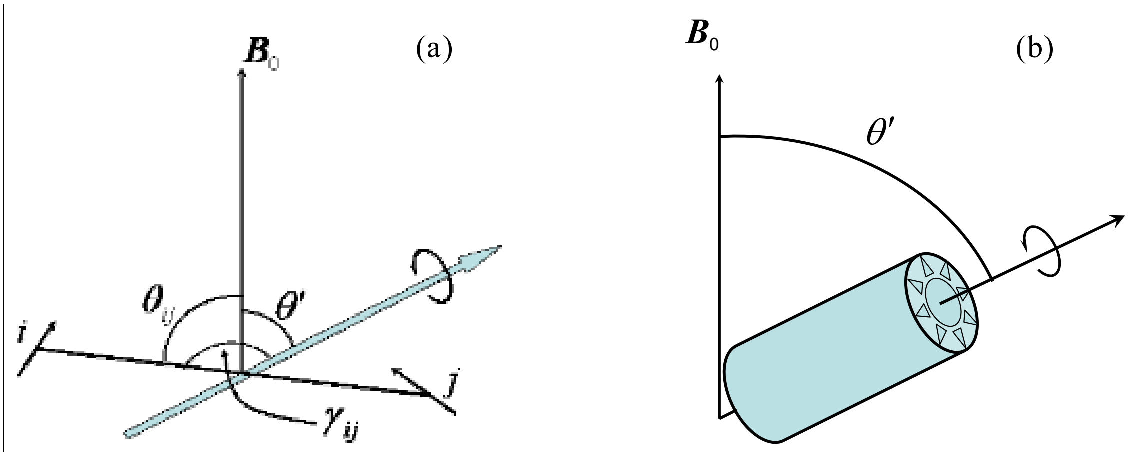

Fig. 1 Angles important in describing the rotation of a molecule.

This expression suggested that one could produce the rotation artificially by turning the entire sample. In this case, the angle θ' would be the same for all pairs of nuclei throughout the sample. Then if one chose θ' to satisfy the condition

$$1-3\cos^2\theta' = 0 \tag{5}$$

the time averaged dipolar coupling would vanish. This value of θ' (54.74°) soon became known as the magic angle, and such a method of line narrowing is called magic angle spinning (abbreviated as MAS). It is historically the first of the methods for narrowing dipolar-broadened lines.

The effect of spinning on dipolar coupling is only one of several important uses of spinning to eliminate unwanted couplings. The line broadening is caused by the orientation dependence of the anisotropic interactions, and is simply a superposition of resonance lines originating from different orientations of the molecules. This is the case for the anisotropic chemical shift, first order quadrupolar couplings and dipolar couplings of isolated spin pairs. The Hamiltonian of the above couplings all contain the factor $1-3\cos^2\theta'$ under MAS, which could be averaged out or reduced by MAS. Thus, magic angle spinning, usually by combining with standard decoupling to ^{1}H nuclei, leads to a high-resolution spectrum.

2 Spin Decoupling

The goal of decoupling is to simplify spectra. A typical NMR spectrum consists of many lines arising from the combined effect of chemical shifts and dipolar couplings. Decoupling is a process which effectively eliminates the dipolar couplings. It is very important for high-resolution spectra of solids, for example to eliminate the effect of proton spins on ^{13}C spectra. We will discuss removing the dipolar coupling between different nuclear species such as ^{1}H and ^{13}C. The basic idea on which all decoupling schemes work can be understood physically as follows. The existence of two lines in the *I*-spin spectrum corresponds to the fact that the *S*-spins to flip back and forth between the up and down (see Section 2.1 for details). If we can cause the *S*-spins to flip back and forth between the up and down orientations sufficiently rapidly, we should achieve an effect much like the motional narrowing of resonance lines. That is, an *I*-spin will precess at a time-averaged frequency rather than at one or the other of two discrete frequencies.

In this Appendix, we will discuss the effect on the *I*-spins of applying a sequence of π pulses to the *S*-spins. We shall see that as the time between *S*-spin π pulses gets shorter and shorter, the *I*-spin spectrum goes from two distinct lines separated by a in angular frequency, to a single line at the average frequency.

Let's first look at the time development of the *I*-spin magnetization following a $\pi/2$ pulse applied to the *I*-spins. In the absence of *S*-spin pulses, the *I*-spin magnetization will consist of two components, one oscillating at $\omega_{0I}+a/2$, the other at $\omega_0-a/2$. So, if we choose $\omega_I=\omega_{0I}$, in the ω_I reference frame the components will precess at angular frequencies $+a/2$ and $-a/2$. If the system were perfectly decoupled, *a* would become effectively zero, so both components are at rest in the ω_{0I} reference frame, and the transverse *I*-spin magnetization will be a constant in time. (We are not including relaxation effects in our Hamiltonian. If we did, the *I*-spin transverse magnetization would decay rather than remaining a constant in time.)

If we apply a single π pulse to the *S*-spins at a time $t=t_\pi$, at time $t=2t_\pi$ the magnetization $\left\langle M_{Iy}(t)\right\rangle$ has returned to its values at time $t=0^+$, immediately after the $\pi/2$ pulse (Fig 2 (a)). Though the magnetization at the time of the π pulse is smaller by factor $\cos(at_\pi/2)$, the π pulse has produced an echo at $t=2t_\pi$, we can repeat the echo by applying a second π pulse to the *S*-spins. If we apply it at a time $t_\pi^{'}$, hence $t_\pi^{'}-2t_\pi$ after the first echo (Fig 2 (b)), or at a time $t^{''}$ given by

$$t^{''}=t_\pi^{'}+(t_\pi^{'}-2t_\pi) \tag{6}$$

and we chose $t_\pi^{'}$ to be given by

$$t_\pi^{'}=3t_\pi \text{ then} \tag{7}$$

$$t^{''}=4t_\pi \tag{8}$$

so that the time delay of the second echo after the first is identical to the time delay of the first echo after the initial signal, then an echo could be produced at $t^{''}=4t_\pi$. We repeat this process again and again. The situation is shown in Fig 2 (c). If we choose a shorter time for t_π, the magnetization versus time will appear like the solid curves in Fig 2 (d), rather than the dashed curves. Clearly, $\left\langle M_{Iy}(t)\right\rangle$ will be a periodic function as long as there is no relaxation, with period $2t_\pi$. We can think of $\left\langle M_{Iy}(t)\right\rangle$ as consisting of a constant with a superimposed periodic ripple, and the more $\left\langle M_{Iy}(t)\right\rangle$ approaches a constant in the reference frame rotating at ω_{0I}, hence behaves as though *a* were zero. Thus, we have "decoupled" the *S*-spins from the *I*-spins.

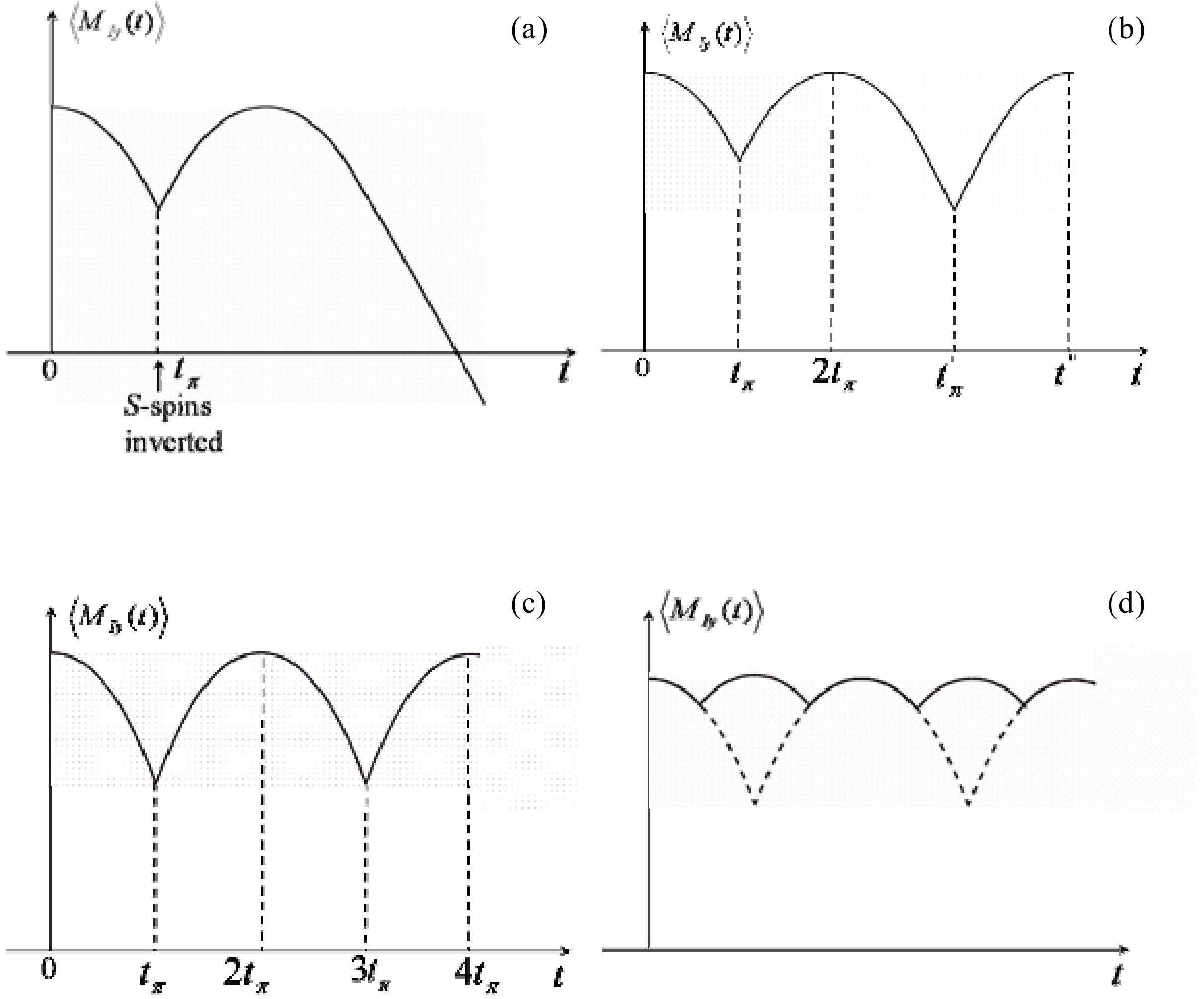

Fig. 2 The effect of rf pulses on $\left\langle M_{Iy}(t)\right\rangle$ at different time. (a) $\left\langle M_{Iy}(t)\right\rangle$ versus time, t. At $t=\pi$, the *S*-spins are inverted by a π pulse; (b) $\left\langle M_{Iy}(t)\right\rangle$ versus t for the case of a π pulse applied to the *S*-spins at $t=t_\pi$, followed by another π pulse at t_π'. (c) The effect on $\left\langle M_{Iy}(t)\right\rangle$ of applying a pair of π pulses to the *S*-spins at time t_π and $t=3t_\pi$. (d) The effect on $\left\langle M_{Iy}(t)\right\rangle$ of halving the time t_π.

3 Cross Polarization

Solid state NMR of dilute nuclei, such as ^{13}C, ^{29}Si, and ^{15}N (isotropic abundance of 1.1%, 4.7%m and 0.03%, respectively) suffers from low sensitivity, particularly when these nuclei also have a low gyromagnetic ratio. Cross polarization (CP) exploits the fact that in many solids the dilute and abundant nuclei are in close proximity and are thus coupled via the magnetic dipolar interaction. As CP is based on heteronuclear dipolar interactions, it is sensitive to internuclear distances and the mobility of molecules or functional groups involved. This means that CP can also be used to establish the connectivity between coupled nuclei and to monitor molecular dynamics in solids, a very useful feature in structural determination.

The language of thermodynamics is well suited to a discussion of the phenomena of CP, so we will start this section with the concept of spin temperature. This part of the discussion is mainly derived from the books authored by Slichter[1] and Fukushima and Roeder[2], and a paper by Pines[3].

3.1 Spin Temperature

Consider a spin-1/2 system in a static magnetic field B_0. For each spin, we will denote the high and the low energy states by the labels *b* and *a* so that a spin in state *b* is antiparallel to the static field and vice versa. The difference in energy between the two states for one spin is $\Delta E = \gamma \hbar B_0$. The spin population associated with the spin states can be sketched in the following way where each 'x' represents a spin (Fig. 3 (a)).

If the spin system is in thermal equilibrium with the surroundings (which we will call the lattice), the ratio of the populations in the two states will be given by the Boltzmann relation where *T* is the temperature of the lattice.

$$N_b / N_a = \exp(-\Delta E / kT) \qquad (9)$$

Suppose that the spin populations are now disturbed so that some additional nuclei in state *a* are promoted to state *b*. While the system may no longer be in thermal equilibrium with the lattice, the populations can still be described by the Boltzmann relation, and the definition of *T* should be changed to keep the relationship correct. Since the ratio N_b / N_a is now greater than it was when the system was in thermal equilibrium with the lattice, the new temperature T_S must be greater than the lattice temperature T_L. T_S will recover towards T_L by giving up thermal energy. T_S is defined as the spin temperature for the particular spin system and note that a two-level system can always be described by it. For the remainder of this section, we will consider only two level systems for simplicity.

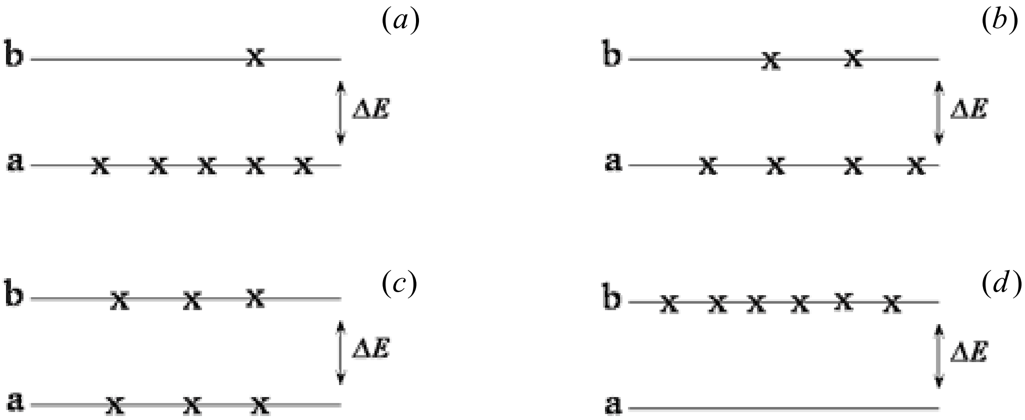

Fig. 3 Spin population distribution for a spin 1/2 system.[2]

The sketch in Fig. 3 (b) shows the qualitative change in the populations for the system at higher T_S. We now consider several situations in order to understand the connection between the spin populations and T_S. First, suppose that all the spins are in the lower energy state. Since N_b / N_a is zero, the Boltzmann relation requires that T_S=0. Even though the third law of thermodynamics states that we can never achieve this temperature, we note that when T_S approaches zero the system is approaching its lowest energy configuration. Next, we heat up the spin system so that some of the spins are now in state *b*, even though $0<N_b/N_a<1$ so that T_S has a finite positive value. If more energy is put into the spins, the system will eventually reach the situation shown in Fig. 3 (c) where $N_b/N_a=1$. In NMR, we say that the spins are saturated and this corresponds to the situation immediately after a $\pi/2$ pulse. From the Boltzmann relation, $T_S=\infty$ is a valid solution. If the spins are heated even further, an excess of spins is in state *b*, $N_b/N_a>1$. In order for that to be true, T_S must be negative. So, now it seems that the spins are hotter than they were at $T_S=\pm\infty$ but the temperature is negative. The existence of negative temperature is contingent on the existence of a maximum energy.

A spin system in equilibrium with a static magnetic field B_0 produces a magnetization according to Curie's law $\vec{M}=C\mu\vec{B}_0/T$. If the system can be characterized by a spin temperature T_S which is not necessarily equal to the lattice temperature T_L, Curie's law still holds so that $\vec{M}=C\mu\vec{B}_0/T_S$. All other thermodynamic relations hold, as well, so that spin temperature can be used to calculate the polarizations of interacting spin systems, especially if they are relatively isolated from the lattice. Such spin calorimetry can be extremely useful, either in calculations or in giving physical insights where applicable, for example, in the discussion on cross polarization.

3.2 General Theory of Cross Polarization

Now we consider observing the insensitive nucleus, usually ^{13}C in a solid, with enhanced sensitivity by taking advantage of the dipolar interaction with an abundant nucleus, e.g. ^{1}H, in the same system. A system of rare spin (*S*) is detected by observing its cumulative effects on an abundant spin system (*I*). The language of spin thermodynamics, is well suited to a discussion of these phenomena (Fig. 4).

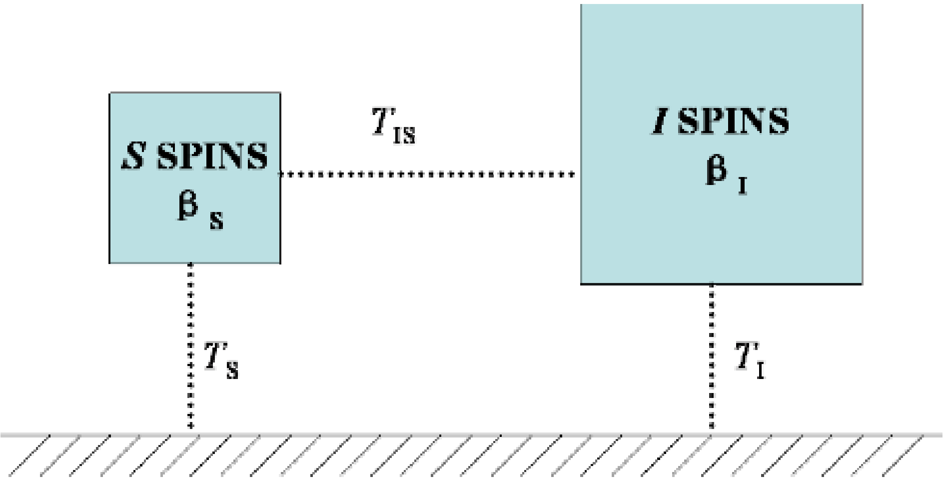

Fig. 4 Simple thermodynamic picture for double resonance.[3]

Consider, for simplicity, that both spin species, *I* and *S*, have spin 1/2. Thermodynamically, such a system can be viewed as consisting of a lattice with a huge heat capacity and two subsystems, *I* and *S*, the former with a much larger heat capacity than the latter. Basically, the experiment works as follows: the *I* spin system is brought into equilibrium with the lattice at an inverse temperature $\beta_L = (kT_L)^{-1}$, where T_L is the lattice temperature mentioned in last section. Normally, according to Curie's law a large magnetization $\gamma\hbar < I > \propto N_I \beta_L$ could now be observed. We also assume that the magnetization of spin *I* is "locked" along the H_{1I} field, which is achieved when H_{1I} is greater than any local dipolar field. During the spin lock a large magnetization of the abundant spins *I* is held by a relatively weak magnetic field H_{1I}. This situation corresponds to a large difference of spin populations between the abundant spin levels, in other words to a very low spin temperature. This means that the *I* spin subsystem has, just before the CP contact, a high inverse spin temperature β_I. At this moment, the magnetization of the *S* spins in the rotating frame is zero, equivalent to an infinite spin temperature or zero inverse spin temperature β_S. The *I* spins are now brought into contact with the *S* spins which are imagined to have no spin order, i.e., an infinite spin temperature.

The contact can be established by matching the Zeeman splittings of the two spins. The simplest method to visualize is the application of two strong rf fields, H_{1I} and H_{1S}, at the *I* and *S* resonance frequencies. In order for the polarization transfer to be possible, the magnetizations of spin *I* and *S* must fulfill the Hartmann-Hahn condition

$$\gamma_I H_{1I} = \gamma_S H_{1S} \tag{10}$$

If the Hartmann-Hahn condition is satisfied, the Zeeman splittings of the *I*-spins quantized along H_{1I} in the *I*-spin rotating frame equal to the Zeeman splittings of the *S*-spins quantized along H_{1S} in the *S*-spin rotating frame. Moreover, the spin systems are coupled via the dipolar interaction. For two spins of unlike species that portion of dipolar interaction which broadens the line is

$$\mathcal{H}_d \propto \frac{\gamma_I \gamma_S}{r_{IS}^3} \hbar^2 I_z S_z (1 - 3\cos^2\theta_{IS}) \tag{11}$$

For a coupled system, when the natural frequencies coincide, resonance transfer of energy results. Thus for two coupled pendulums, one at rest initially, the other set in motion, after a while the first reaches a maximum amplitude, with the second one at rest. Then the energy exchange reverses, the pendulum which was driven now drives, the pendulum which drove now is driven. Then mutual *I* and *S* spin flips via the *I-S* dipolar interaction become energy conserving and cause the system to proceed rapidly to internal equilibrium. The result is a cooling of the *S*-spin system by the establishment of *S*-spin order (in the form of a magnetization along H_{1S}) and a small heating of the *I*-spin reservoir (a small decrease in the *I* magnetization). The effect in the *I*-spins is very small since the *S* spins are rare. Energy flows from the *S*- to the *I*-spin reservoir causing a cumulative heating and destruction of the *I*-spin order.

If the cycle is repeated many times, the net effect is a substantial heating of the *I*-spin reservoir; subsequent observation of the *I* magnetization discloses a correspondingly large change leading to a greatly enhanced sensitivity in the detection of the *S*-spin resonance. This method is called cross polarization.

Following the *I*-*S* contact, the *S*-spin decay is observed. Spin decoupling, and thus high resolution, is achieved by the same *I*-spin irritation used for the spin locking. The cycle is repeated for *n* times, and the *S* signals accumulated until the *I* magnetization is depleted. This yields, of course, a large sensitivity enhancement over conventional *S* free induction decay by the factor of $(\gamma_I / \gamma_S)(1-\varepsilon)^n$ [3], here $\varepsilon = S(S+1)N_S / I(I+1)N_I$ and N_S and N_I are the numbers of *I* and *S* spins; we have therefore made some recognizable progress in our attack on the problem of sensitivity, making the present approach an attractive one for high-resolution NMR in solids.

4 References

1. C. P. Slichter, *Principles of Magnetic Resonance*, (1990). Springer-Verlag New York.
2. E. F. Roeder, and S. B. W. Roeder, *Experimental Pulse NMR*, (1981). Addison-Wesley Publishing Company, Inc.
3. A. Pines, M. G. Gibby, and J. S. Waugh, *J Chem. Phys.*, **59,** 569. (1973).